



Master's thesis

**Investigation of the Magnetically Active
Detached Eclipsing Binary System V80 using
New Photometric Observations from The Kepler
Space Telescope**

Timmi Grosen Jørgensen

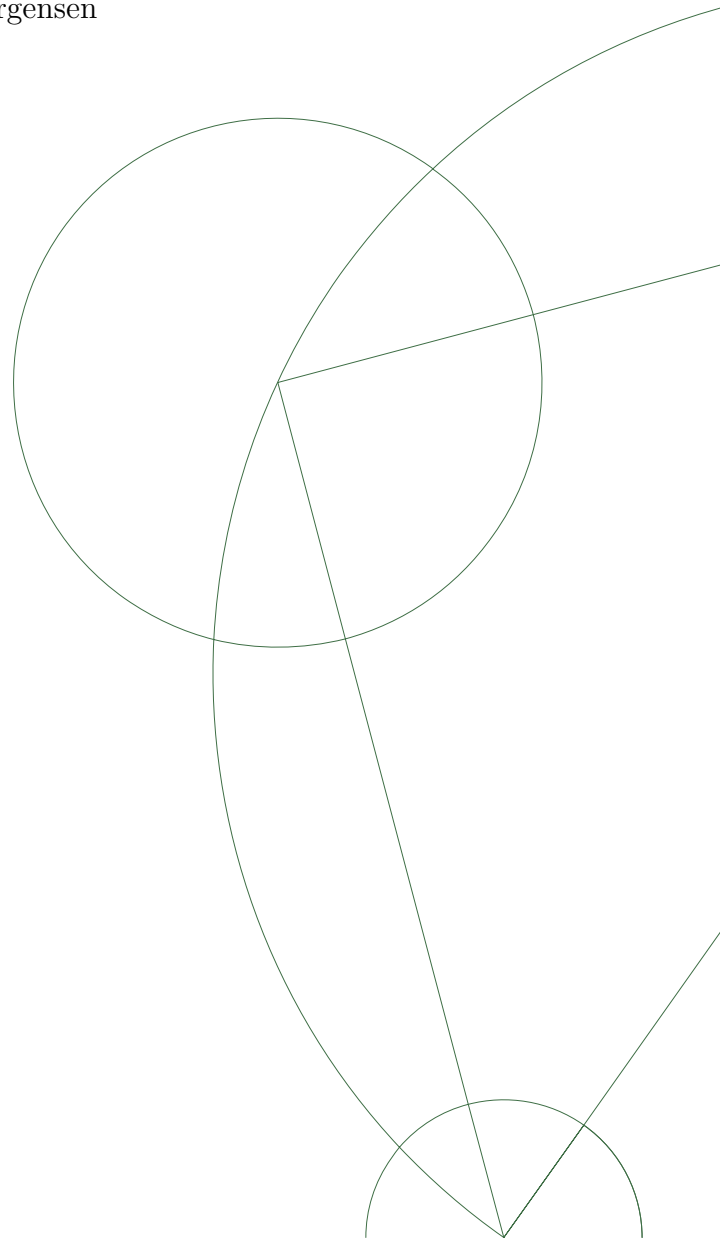
Supervisor:

Anja C. Andersen
Dark Cosmology Centre
University of Copenhagen

Supervisor:

Karsten F. Brogaard
Department of Physics and Astronomy
Aarhus University

Submitted: September 19, 2014



Abstract

This thesis investigates the magnetically active detached eclipsing binary system V80 by using new photometric data from the Kepler Space Telescope along with observations from Brogaard et al. (2011). Magnetically active stars are known to show discrepancies between observation and stellar models which predict stellar radii and temperatures which are $\sim 10\%$ lower and $\sim 5\%$ higher than what is observed, respectively. The standard procedure to regain agreement is to decrease the mixing-length-parameter α_{MLT} in order to mimick the expected reduction in convective efficiency due to starspots. This procedure is however highly likely to result in flawed estimates of the stellar parameters of such systems since it is assumed that the discrepancies can be explained solely by α_{MLT} while keeping parameters such as helium abundance and $[\text{Fe}/\text{H}]$ constant and disregarding their uncertainties. V80 is a member of the open cluster NGC 6791 which has an age constrained to be 8.3 ± 0.3 Gyr from two other longer period detached eclipsing binaries that show no signs of magnetic activity. By knowing the mass-radius (MR) relation that V80 is expected to follow if it was unaffected by magnetic activity, we perform light curve analysis to obtain the best estimate of the radii of the components. We determine the radii of V80 to lie in the range of $1.396 \pm 0.067 R_{\odot} < R_p < 1.354 \pm 0.067 R_{\odot}$ and $0.7595 R_{\odot} < R_s < 0.8358 R_{\odot}$ for the primary and secondary components, respectively. For the primary component this is $6.8 - 10.5\%$ larger than what is expected for star which are not magnetically active.

V80 has high variability in its light curve which is caused by starspots generated by magnetic activity. Further signs of magnetic activity reveals itself by V80 being an X-ray source and by our identification of a superflare in its Kepler light curve. We present evidence indicating that the magnetic activity of V80 is originating from the primary component which also seems to be experiencing anti-solar differential rotation.

Contents

Abstract	i
1 Introduction	1
2 Theory - Eclipsing Binary systems	3
2.1 Two-body orbital motion	3
2.1.1 Relative and barycentric orbits	5
2.1.1.1 Relative orbit	6
2.1.1.2 Barycentric orbits	6
2.1.1.3 Kepler's 3rd law and relationships between barycentric and relative orbits	7
2.1.2 Speed as a function of position	7
2.1.3 Kepler's equation	8
2.1.4 Orientation of the orbit	9
2.1.4.1 Radial velocity	10
2.2 Analytic theory of light curves	11
2.2.1 Eclipses in binary orbits	13
2.2.2 Modeling light curves	15
2.3 Roche model	16
2.4 Blackbody radiation	17
2.5 Light curve perturbations	17
2.5.1 Limb darkening	17
2.5.2 Gravity darkening	18
2.5.3 Reflection and heating	18
2.6 Stellar evolution in Detached Binary systems	19
2.6.1 Stellar abundances and [Fe/H]	19
2.6.2 The CNO cycle	19
2.6.3 Energy transport and mixing length parameter	20
3 Data	23
3.1 The Kepler Space Telescope	23
3.2 Kepler light curve data	26
3.2.1 Kepler data and extraction of data	26
3.2.1.1 Light Curve Binary Extension	26

3.2.1.2	Aperture Extension	27
3.2.2	Target Pixel Data	27
3.3	Brogaard et al. 2011	27
3.3.1	Photometry	27
3.3.2	Spectroscopy	28
3.3.3	Absolute dimensions	29
4	Data analysis	31
4.1	Starspot period	31
4.2	Orbital period of V80	36
4.2.1	Estimation of the orbital period of V80 from PDM	36
4.2.2	Kwee Van Woerden method	36
4.2.2.1	Kepler long and short cadence data	36
4.2.2.2	V and R band data	38
4.2.3	Period and ephemerides	40
4.2.4	O-C diagram	40
4.3	Removal of the magnetic activity	41
4.4	Determining limb darkening coefficients for the components of V80	45
4.5	Preliminary light curve analysis	48
4.5.1	JKTEBOP code	48
4.5.2	Preliminary light curve analysis using V , R and Kp light curves	48
4.5.3	Preliminary light curve analysis using Kepler long cadence light curves	51
4.6	Analysing the magnetic activity of V80	55
4.6.1	Stellar magnetic fields and starspots	55
4.6.2	Preparing the Kepler long cadence light curve	55
4.6.3	Confirmation of starspots	56
4.6.4	Observation of a superflare	60
4.6.5	Line emission	61
4.6.6	X-ray emission and stellar rotation period	62
4.7	Light curve analysis of Kp^*	63
4.7.1	Light ratio in Kp^*	63
4.7.2	Implementing the isochrone of NGC 6791	64
4.7.2.1	Brogaard et al. (2012)	64
4.7.3	Using the isochrone from NGC 6791 as a constant	64
5	Results and discussion	67
5.1	Absolute dimensions	67
5.2	Radius estimation of the primary component	70
5.3	Magnetically active detached binaries	72
5.3.1	Clausen et al. (2008)	73
5.3.2	Clausen et al. (2009)	73
5.3.3	Vos et al. (2012)	73
5.3.4	Article discussion	73

5.4	Anti-solar differential rotation	74
5.4.1	Reports of stars indicating anti-solar differential rotation	74
5.4.2	Strassmeier et al. (2003)	75
5.4.3	Hackman et al. (2001)	76
5.4.4	Comparison to the primary component of V80	79
6	Summary and conclusions	80

1. *Introduction*

Detached eclipsing binary systems are of fundamental importance to stellar physics and the study of stellar evolution models since they are the only stars for which we can precisely and accurately measure quantities such as mass, radius and surface gravity. Stars in a binary system are born from the same gas cloud and they therefore share a common age together with other stellar parameters. Even though the two stars are part of the same mutual gravitationally bound system they still evolve as single stars if they are well separated. This is why detached binary systems are perfect for testing stellar evolution models.

Stars in stellar clusters are all formed from the collapse of the same gas cloud and they therefore generally share the same age and original composition of hydrogen, helium and heavy elements. Because of this, stellar model isochrones can be compared to the brightness and color of the cluster members in order to determine the cluster age and test stellar models.

V80 is a detached eclipsing binary system which is showing variability in its light curve between eclipses which is believed to be caused by starspots generated by magnetic activity. Magnetic activity in the components of binary systems are known to result in discrepancies between observations and models of stellar parameters. Stellar models are known to predict stellar radii and temperatures which are $\sim 10\%$ lower and $\sim 5\%$ higher than what is observed, respectively. The standard procedure is to decrease the mixing-length-parameter α_{MLT} in order to mimick the expected reduction in convective efficiency due to starspots. This procedure is however highly likely to result in flawed estimates of the stellar parameters such as age of such systems, since it is assumed that the discrepancies can be explained solely by α_{MLT} while keeping parameters such as helium abundance Y and $[\text{Fe}/\text{H}]$ constant and disregarding their uncertainties.

V80 is a member of the open cluster NGC 6791 which has an age constrained to be 8.3 ± 0.3 Gyr from two other longer period detached eclipsing binaries that show no signs of magnetic activity. By knowing the mass-radius (MR) relation that V80 would follow if it was unaffected by magnetic activity we can be certain that the possible discrepancies between observation and the MR relation are indeed real and not a consequence of a wrong estimate of the stellar parameters of the system.

In Chapter 2 we address the basics of detached eclipsing binaries and how parameters such as mass and radii can be obtained through radial velocity and photometric light curve measurements. If the reader is familiar with the theory of detached eclipsing binaries Chapter 2 can be skipped. In Chapter 3 we present the light curve data from the Kepler Space Telescope and introduce the data analysis performed in Brogaard et al. (2011) which we will incorporate into our investigation of V80. Chapter 4 explains the data analysis which was done for V80. Chapter 5 shows the obtained results where the results will also be discussed. In Chapter 6 we conclude on our investigation of V80.

2. Theory - Eclipsing Binary systems

2.1 Two-body orbital motion

Newton was the first to show that a spherical body of mass m has a gravitational potential field equivalent to a point mass m located at the centre of the sphere. By considering this, two spherical stars can be treated as two point masses orbiting each other in their mutual gravitational field. Stars are not completely spherical bodies due to their rotation and the tidal forces they exert on each other. However, if the stars are well separated (detached), this approximation is valid. Around 85-90 % of a main-sequence star's total mass is contained within the inner 50 % of its radius which means that the point mass approximation is a good description for detached binaries. As stars evolve they become even more centrally condensed which only justifies the approximation even more.

A force, F , is described as a central force if it is always directed towards a fixed point and if it is parallel to the radial direction \vec{r} . In a two-body system this fixed point will be the location of the centre of mass which both bodies will be orbiting. The central force is a conservative force if the motion of a body in the force field obeys the laws of conservation of energy which means that the kinetic and potential energy is constant. In such a scenario angular momentum will be conserved and angular momentum, $\vec{J} = m\vec{r} \times \dot{\vec{r}}$, will therefore be constant for a body of mass m .

If one wants to investigate the motion of a body of mass m which is acted upon by a central force, one can look at Figure 2.1 where the central force is directed towards the origin O . In a time dt the body moves from P_1 to P_2 , where its radial and angular position changes from r to $r + dr$ and θ to $\theta + d\theta$, respectively. The velocity $\dot{\vec{r}}$ can be separated into two components, namely, the radial component along the direction of \vec{r} and the transverse component in the direction of $\hat{\theta}$. The radial component of the velocity is given by $dr/dt = \dot{r}$, while the transverse component of the velocity is $r d\theta/dt = r\dot{\theta}$. The velocity is therefore given by

$$\dot{\vec{r}} = \dot{r}\hat{r} + r\dot{\theta}\hat{\theta} \quad (2.1)$$

where \hat{r} and $\hat{\theta}$ are the unit vectors in the radial and transverse directions, respectively. In order to evaluate the acceleration the body experiences due to the action of the force \vec{F} , $\dot{\vec{r}}$ needs to be differentiated with respect to time. Since we are in cylindrical

coordinates, the unit vectors themselves must also be operated on. Evaluating the unit vectors, we see that $d\hat{r}/dt = (d\hat{r}/d\theta) (d\theta/dt) = \hat{\theta}\dot{\theta}$ and $d\hat{\theta}/dt = (d\hat{\theta}/d\theta) (d\theta/dt) = -\hat{r}\dot{\theta}$. The acceleration of the body therefore becomes

$$\ddot{\vec{r}} = \ddot{r}\hat{r} + \dot{r}\dot{\theta}\hat{\theta} + \dot{r}\dot{\theta}\hat{\theta} + r\ddot{\theta}\hat{\theta} + r\dot{\theta}\dot{\theta}(-\hat{r}) = (\ddot{r} - r\dot{\theta}^2)\hat{r} + (2\dot{r}\dot{\theta} + r\ddot{\theta})\hat{\theta}. \quad (2.2)$$

In Eq. 2.2 the second term is the transverse component of the acceleration, which is directly linked to Kepler's second law. Kepler's second law states that the radius vector \hat{r} sweeps out equal areas in equal time intervals in the orbit. This can easily be shown by considering the magnitude of the angular momentum vector \vec{J} , which is given by $J = m\vec{r} \times \dot{\vec{r}} = mr^2\dot{\theta}$. The area which is swept out by \vec{r} is given by $dA = r^2 d\theta/2$ resulting in $dA/dt = (1/2)r^2\dot{\theta} = J/(2m)$. Since J is constant, $r^2\dot{\theta}$ will be constant as well. This means that for large r , the value of $\dot{\theta}$, the rate of change of the position angle, must be small and vice versa for small r , $\dot{\theta}$ must be large in order to satisfy our expression. It is also worth noting that

$$\frac{1}{r} \frac{d(r^2\dot{\theta})}{dt} = 2\dot{r}\dot{\theta} + r\ddot{\theta} = 0 \quad (2.3)$$

since $r^2\dot{\theta}$ is constant. This means that the transverse component of the acceleration is zero, which is what was expected since the force field is purely radial dependent.

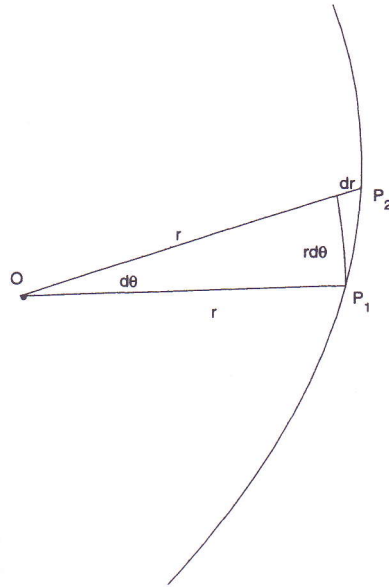


Figure 2.1 – The orbital motion of a body of mass m acted upon by a central force F directed towards the origin O . In a time dt the body moves from P_1 to P_2 , where its radial and angular position changes from r to $r + dr$ and θ to $\theta + d\theta$, respectively. Credit: Hilditch (2001).

In order to determine which kind of motion the body will take under the influence of

the force \vec{F} , the laws of conservation of energy and of angular momentum can be used

$$\frac{1}{2}m\dot{r}^2 - \frac{Gmm_c}{r} = C \quad (2.4)$$

$$\frac{d}{dt}\vec{J} = \frac{d}{dt}(m\vec{r} \times \dot{\vec{r}}) = 0 \quad (2.5)$$

where G is the gravitational constant, m_c is the central mass and m is the mass of the body which is under consideration. By making the law of conservation of energy in Eq. 2.4 purely radial dependent, it can be shown that the form of the orbit is described by the equation

$$r = \frac{l}{1 + e \cos(\theta)} \quad (2.6)$$

where $l = J^2/(Gm_cm^2)$. Eq. 2.6 is the standard polar equation for a conic section. For binary systems such conic sections will be ellipses where e is the eccentricity and l is called the semi-latus rectum of the ellipse¹. The eccentricity can vary in the range of $0 \leq e < 1$ and the semi-latus rectum of the ellipse is $l = a(1 - e^2)$ where a is the semimajor axis of the ellipse. The position of the binaries in their orbit can then be described by Eq. 2.6, which will be important when determining the orbital speed of the stars.

2.1.1 Relative and barycentric orbits

There are two kinds of orbits which are important to understand in order to estimate the radii and masses of the components in a binary system. These orbits are the relative and barycentric orbits of the two stars which will be considered by using Figure 2.2.

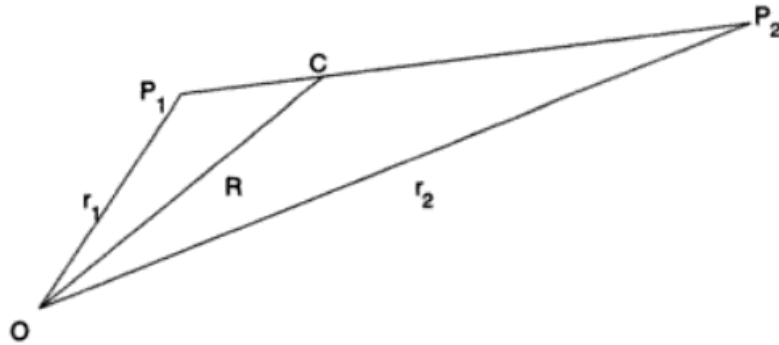


Figure 2.2 – A vector diagram with a reference point, O , the centre of mass, C , and the positions of the masses, m_1 and m_2 at P_1 and P_2 , respectively. Credit: Hilditch (2001).

¹Hilditch (2001), page 32.

The two stars will orbit their common centre of mass C , relative to a reference point, O . At a given time, t , the masses of the stars, m_1 and m_2 are located at P_1 and P_2 , respectively. The distance between the stars is $\vec{P}_2\vec{P}_1 = \vec{r} = \vec{r}_1 - \vec{r}_2$, with the unit vector $\hat{r} = \vec{r}/r$. The equation of motion of the two stars will then be given by

$$m_1\ddot{\vec{r}} = -\frac{Gm_1m_2}{r^2}\hat{r}; \quad m_2\ddot{\vec{r}} = -\frac{Gm_1m_2}{r^2}(-\hat{r}) \quad (2.7)$$

2.1.1.1 Relative orbit

The relative motion is an important tool to estimate the various system parameters and it is therefore worthwhile to consider the motion of one component of a binary system relative to its companion. The relative motion is easily achieved by subtraction of the two equations of motion in Eq. 2.7.

$$\ddot{\vec{r}} = \ddot{\vec{r}}_1 - \ddot{\vec{r}}_2 = -\frac{G(m_1 + m_2)}{r^2}\hat{r} \quad (2.8)$$

By introducing a mass term, $\mu = m_1m_2/(m_1 + m_2)$, which is called the reduced mass, the equation of the relative motions takes the following form

$$\mu\ddot{\vec{r}} = -\frac{G(m_1 + m_2)}{r^2}\mu\hat{r} = -\frac{Gm_1m_2}{r^2}\hat{r} \quad (2.9)$$

This means that the motion of either star in the relative orbit is as though the orbiter has a mass μ and the central mass is the total mass of the system.

2.1.1.2 Barycentric orbits

The barycentric orbits describe the motion of each of the stars with respect to the centre of mass of the binary system. By referring back to Figure 2.2, we can define the vectors $\vec{CP}_1 = \vec{R}_1$ and $\vec{CP}_2 = \vec{R}_2$ which leads to the following:

$$\vec{r}_1 = \vec{R} + \vec{R}_1; \quad \vec{r}_2 = \vec{R} + \vec{R}_2; \quad \vec{r} = \vec{R}_1 - \vec{R}_2 \quad (2.10)$$

The centre of mass is defined as:

$$m_1\vec{r}_1 + m_2\vec{r}_2 = (m_1 + m_2)\vec{R} \quad (2.11)$$

which combined with Eq. 2.10 leads to $m_1\vec{R}_1 + m_2\vec{R}_2 = 0$. The vector \vec{r} connecting the two stars can now be written as two different expressions

$$\vec{r} = +\frac{m_1 + m_2}{m_2}\vec{R}_1 \quad \text{or} \quad \vec{r} = -\frac{m_1 + m_2}{m_1}\vec{R}_2 \quad (2.12)$$

We want to know the expressions for $\ddot{\vec{R}}_1$ and $\ddot{\vec{R}}_2$, which will describe the motion of the barycentric orbits of the stars around their common centre of mass. From Eq. 2.10 we see that the accelerations are $\ddot{\vec{r}}_1 = 0 + \ddot{\vec{R}}_1$ and $\ddot{\vec{r}}_2 = 0 + \ddot{\vec{R}}_2$, because the centre of mass

will move with constant velocity through space unless it is being affected by external sources. The two barycentric equations of motion then become

$$\ddot{\vec{R}}_1 = -\frac{Gm_2^3}{(m_1 + m_2)^2} \frac{\vec{R}_1}{R_1^3}; \quad \ddot{\vec{R}}_2 = -\frac{Gm_1^3}{(m_1 + m_2)^2} \frac{\vec{R}_2}{R_2^3} \quad (2.13)$$

2.1.1.3 Kepler's 3rd law and relationships between barycentric and relative orbits

It is important to understand the connections between the barycentric and relative orbits given in Eq. 2.9 and Eq. 2.13, so their relative sizes and orientations can be used to measure the masses and radii of the stars through observations. All three equations consist of a combination of the gravitational constant and a variable expression involving the masses of the two stars. The centre of mass does not change which means that the periods of the three different orbits will be the same, namely, $P = P_1 = P_2$. If we consider Kepler's third law which is given in Eq. 2.14, the fraction a^3/P^2 is proportional to a mass term, M .

$$M = 4\pi^2 \frac{a^3}{P^2} \quad (2.14)$$

The mass term together with the semimajor axis will be different for each of the three orbits which are given by the following:

$$\text{relative orbit: } a = a; \quad M = G(m_1 + m_2) \quad (2.15)$$

$$\text{barycentric orbit of } m_1: a = a_1; \quad M = Gm_1^3/(m_1 + m_2)^3 \quad (2.16)$$

$$\text{barycentric orbit of } m_2: a = a_2; \quad M = Gm_2^3/(m_1 + m_2)^3 \quad (2.17)$$

All three orbits are in the same plane with the same eccentricity, together with the following relations:

$$a = a_1 + a_2; \quad \frac{a}{m_1 + m_2} = \frac{a_1}{m_2} = \frac{a_2}{m_1} \quad (2.18)$$

2.1.2 Speed as a function of position

The orbital speed as a function of position in elliptic orbits will be a continuously varying function of position and time. By recalling Kepler's 2nd law which states that the radius vector sweeps out equal areas in equal intervals of time, i.e. $r^2\dot{\theta}$ is constant, and that $dA/dt = (1/2)r^2\dot{\theta}$, we will now consider the area swept out during a full orbit. The time interval will be $dt = P$, the orbital period and the area will be given by $dA = 2\pi ab$ where b is the semiminor axis of the ellipse. This leads to $r^2\dot{\theta} = 2\pi ab/P = L$ where L is the angular momentum per unit mass, also known as the specific angular momentum which will be important when evaluating the orbital speed.

The velocity of the orbiting body was found in Eq. 2.1 and thus the linear speed V will be given by

$$V^2 = \dot{r}^2 + r^2\dot{\theta}^2 \quad (2.19)$$

In order to evaluate the linear speed we need to differentiate Eq. 2.6 with respect to time and thereby obtain

$$-e \sin(\theta) \dot{\theta} = -\frac{l}{r^2} \dot{r} \quad (2.20)$$

By using $L = r^2 \dot{\theta}$, we can get the radial and tangential components of the velocity:

$$\dot{r} = \frac{L}{l} e \sin(\theta); \quad r \dot{\theta} = \frac{L}{l} (1 + e \cos(\theta)) \quad (2.21)$$

The square of the linear speed can then be found to be

$$V^2 = \dot{r}^2 + r^2 \dot{\theta}^2 = \frac{L^2}{l^2} \left[\frac{2l}{r} - (1 - e^2) \right] \quad (2.22)$$

By using the fact that $L = Ml$, where M is the mass term from Section 2.1.1.3 and that the semi-latus rectum is $l = a(1 - e^2)$, the square of the linear speed is found to be the following:

$$\textit{Elliptic orbit:} \quad e < 1; \quad l = a(1 - e^2); \quad V^2 = M \left[\frac{2}{r} - \frac{1}{a} \right] \quad (2.23)$$

$$\textit{Circular orbit:} \quad e = 0; \quad l = a; \quad V^2 = \frac{M}{a} \quad (2.24)$$

2.1.3 Kepler's equation

The position of a star in an elliptical orbit is not a simple function of time and the equation which is needed to describe this relation is known as Kepler's equation. It is given by the following expression

$$E - e \sin(E) = \frac{2\pi}{P} (t - T_0) \quad (2.25)$$

where t is a point in time in the orbit and E is the angle called the eccentric anomaly which is given by $E = QOR$ and can be viewed in Figure 2.3. T_0 is the time of periastron passage, i.e. $r = a(1 - e)$ or $\theta = E = 0$, which corresponds to the point Π in Figure 2.3. O is the centre of the ellipse, S is the focus where the centre of mass is located for the orbiting body, P is the position of the orbiting body and A is known as apastron which is the point of maximum $r = a(1 + e)$. θ is called the true anomaly and its relation with the eccentric anomaly is given by

$$\tan(\theta/2) = \left[\frac{1 + e}{1 - e} \right]^{\frac{1}{2}} \tan(E/2) \quad (2.26)$$

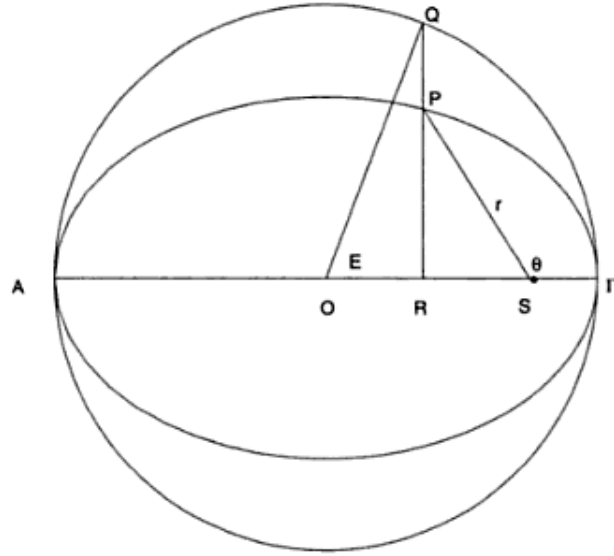


Figure 2.3 – This figure represents the properties of an ellipse. O is the centre of the ellipse and S is the focus which is where the centre of mass is located. Π is the pericentre, the point of closest approach of the orbiting body to S , also known as periastron. A is the apocentre, the point of the orbiting body which is the furthest away from S , also known as apastron. The angle E and θ are called the eccentric anomaly and the true anomaly, respectively. Credit: Hilditch (2001).

2.1.4 Orientation of the orbit

The orientation of a binary system determines how well parameters such as the masses and the semimajor axis can be determined via radial velocity measurements and light curve analysis. It is therefore important to understand the orbit and how the stars move on the tangent plane of the sky. In Figure 2.4 the relative orbit is seen where the primary star is located at the origin O of the xyz coordinate system and the secondary star is located at P_2 . The angle θ is the true anomaly defined by ΠOP_2 and Π is the point of periastron, just like in Figure 2.3. The observer's line of sight is in the direction Oz , from below the figure, and Oz is perpendicular to the tangent plane of the sky which is described by the xNy plane. N is located on a sphere defined by $xNyzO$, where the arc through N is parallel to the orbit. The angle $\Omega = xON$ is called the longitude of the ascending node. It describes the angular position in the orbit where the star is receding from the observer with the greatest velocity. The line NO continues through the sphere on the other side to N' which is called the descending node which will be the point where the star moves with the greatest velocity towards the observer. The inclination of the orbit is given by i . When $i = 90^\circ$ the observer will look directly into the orbital plane. The last angle is called the longitude of periastron and it describes the orientation of the orbit within its own plane and is given by $\omega = NO\Pi$. The six quantities a, i, e, ω, Ω and T_0 are what defines the binary orbit in three-dimensional space which describe its size, shape and orientation.

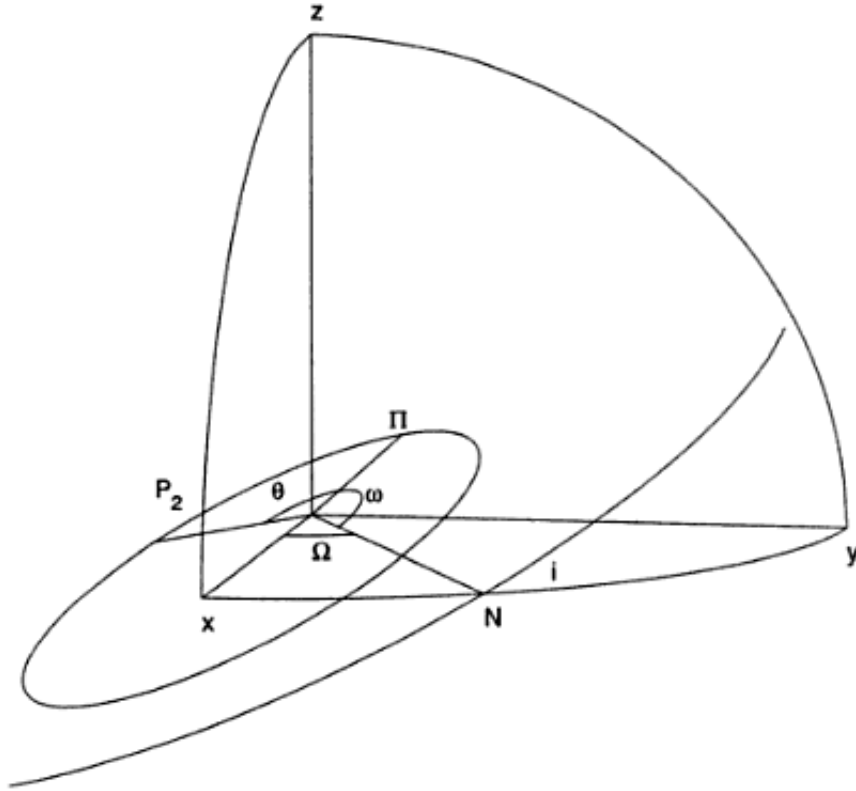


Figure 2.4 – The figure shows the relative orbit where the primary star is located at the origin and the secondary star is located at position P_2 . The observer's line of view is in the Oz direction, from below the figure, and is perpendicular to the tangent plane of the sky defined by xNy .

2.1.4.1 Radial velocity

With the orbital parameters defined we can now proceed to define the radial velocity of the stars which can be measured through spectroscopy. When we project the position vector \vec{r} along the line of sight Oz , we obtain

$$z = r \sin(\theta + \omega) \sin(i) \quad (2.27)$$

By differentiating z with respect to time we are able to determine the radial velocity given by

$$V_{rad} = \dot{z} = \frac{2\pi a \sin(i)}{P(1 - e^2)^{1/2}} [\cos(\theta + \omega) + e \cos(\omega)] \quad (2.28)$$

The radial velocity is usually written in the following form

$$V_{rad} = K [\cos(\theta + \omega) + e \cos(\omega)] + \gamma \quad (2.29)$$

where

$$K = \frac{2\pi a \sin(i)}{P(1 - e^2)^{1/2}} \quad (2.30)$$

K is called the semiamplitude of the velocity curve and γ is the radial velocity of centre of mass of the binary system.

By using the expression for K , one is able to derive the equations for the minimum masses of the binary system in which can be seen in Eq. 2.31.

$$m_{1,2} \sin(i)^3 = \frac{1}{2\pi G} (1 - e^2)^{3/2} (K_1 + K_2)^2 K_{2,1} P \quad (2.31)$$

The subscripts represent the primary and secondary star. If one only has radial velocity measurements of the two stars the orbital inclination i will be unknown and thus the equation only provides the lower limit of the masses of the stars, hence the name. The semiamplitudes of the primary and secondary can also be used to derive the projected semimajor axis $a_1 \sin(i)$ and $a_2 \sin(i)$ from Eq. 2.32.

$$a_{1,2} \sin(i) = \frac{(1 - e)^{1/2}}{2\pi} K_{1,2} P \quad (2.32)$$

By using the relation $a = a_1 + a_2$, the radial velocity measurements can be used to estimate the projected semimajor axis of the relative orbit.

2.2 Analytic theory of light curves

If one wants to know the true masses and the true semimajor axis of the relative orbit, the orbital inclination of the binary system must be known. In order to estimate the orbital inclination, the radii of the two stars in terms of the semimajor axis of the relative orbit and the ratio of the surface brightnesses, light curve measurements are needed. By combining Eq. 2.31 and 2.32 together with the relative radii, $r_{1,2} = R_{1,2}/a$ and the orbital inclination, the masses and radii of the stars can be determined. We will now go through the basics of light curve analysis in order to describe how the parameters such as i and $r_{1,2}$ are obtained.

As the primary and secondary star passes in front of each other in our line of sight, they will block some of the light from their binary partner. This will cause a variation in the observed light curve and depending on the inclination, the shape of these eclipses can take different forms. If $i \sim 90^\circ$ the light curve will have total eclipses which occur when the smaller star is completely occulted by its larger companion. If the inclination is not around 90° both the primary and secondary eclipses will be partial since the stars will only partially block each other. A representation of the same binary system but with different orbital inclinations can be seen in Figure 2.5 and 2.6. The change in orbital inclination causes the secondary eclipse to become only partially, but also causes the eclipse duration to become shorter since the point of contact between the stars changes². If the inclination is $i \sim 90^\circ$ and the orbit is circular, it is very easy to

²Hilditch (2001), page 216.

obtain the relative radii of the two stars, r_1 and r_2 . By looking at Figure 2.5 we get the two following equations

$$\phi_2 - \phi_1 = \phi_4 - \phi_3 = \frac{2R_2}{2\pi a} \quad (2.33)$$

$$\phi_3 - \phi_1 = \phi_4 - \phi_2 = \frac{2R_1}{2\pi a} \quad (2.34)$$

where ϕ is the phase angle where each contact point is described in Figure 2.5. This is a very easy way to determine the relative radii, however when the orbit is not circular the phase angle for the secondary eclipse relative to the primary eclipse will not be located at $\phi = 0.5$. Furthermore, at lower inclinations there will only be partial eclipses and the simple estimation in Eq. 2.33 and 2.34 cannot be used.

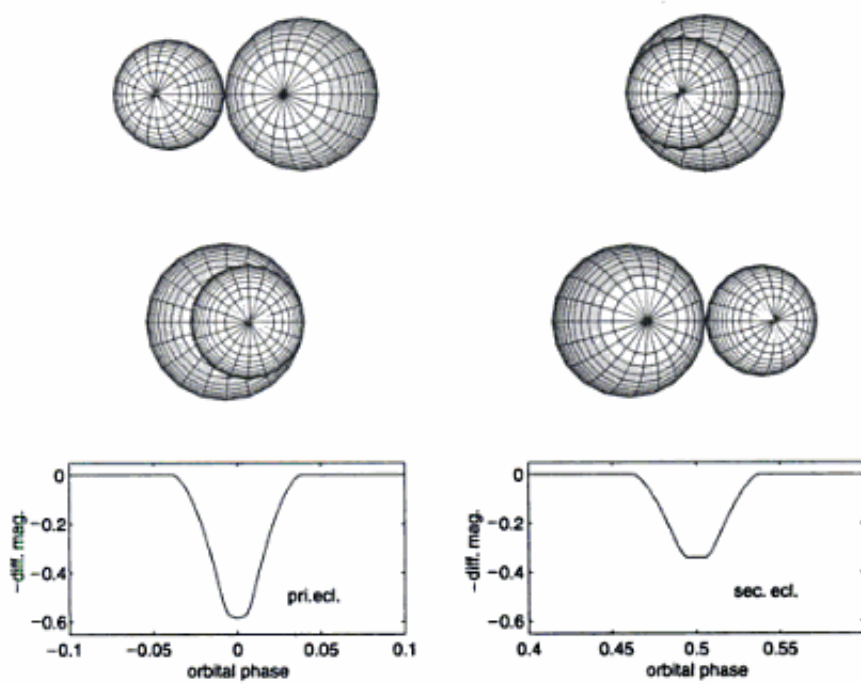


Figure 2.5 – A representation of a binary system with $i = 90^\circ$ where the primary and secondary eclipses are shown. The primary eclipse is seen above the light curves, where we have first contact ϕ_1 (upper left), second contact ϕ_2 (upper right), third contact ϕ_3 (bottom left) and fourth contact ϕ_4 (bottom right). The secondary eclipse is completely occulted by the primary star which causes the bottom of the secondary eclipse to be flat. Credit: Hilditch (2001).

For spherical stars with radii R_1 and R_2 and separation a , the condition for observing eclipses in the light curve of a binary system with orbital inclination i is

$$\sin(90^\circ - i) \leq \frac{R_1 + R_2}{a} \quad (2.35)$$

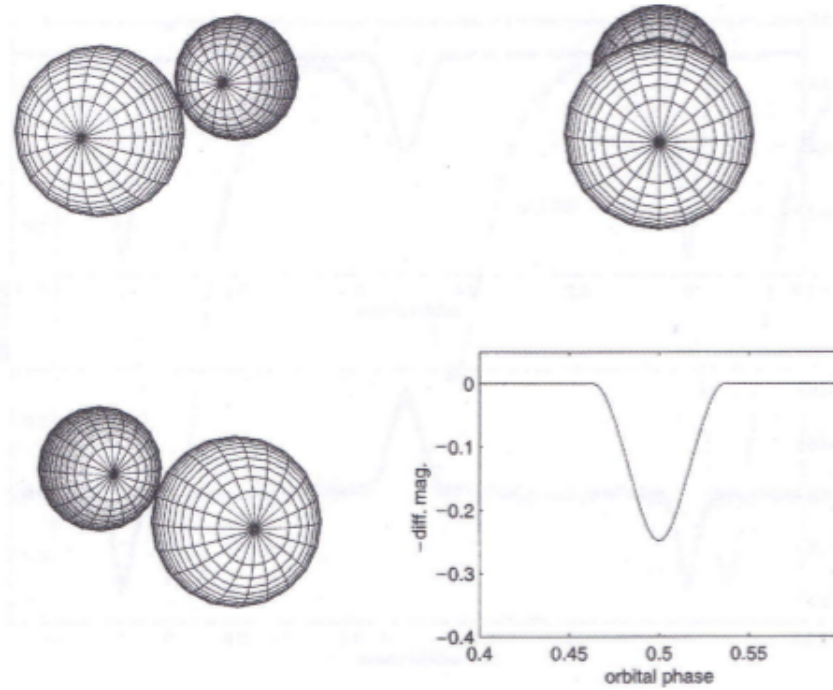


Figure 2.6 – Here is a representation of the same binary system as in Figure 2.5, but with the orbital inclination changed to $i = 85^\circ$. The secondary eclipse is now only partial, but also, the different inclination causes the eclipse to change in duration, since the point of contact of the two stars will be different which results in a shorter duration of the eclipse. Credit: Hilditch (2001).

Observing eclipses is therefore less likely if the stars are small relative to their separation, and thus, it is more likely to observe eclipses for relatively larger stars.

2.2.1 Eclipses in binary orbits

In this section we are going to go through the most important equations which relate the different parameters to the light curve of the binary system. These parameters will involve the orbital inclination, the radii of the two stars in terms of the semimajor axis of the relative orbit, and the ratio of the surface brightnesses.

We start by looking at the projected separation δ between the centre of the two stars. In Figure 2.7 the two stars are represented by O_1 and O_2 and are separated by a distance $a \equiv 1$. They are seen at a phase angle $\phi = \angle NO_2O_1$ and the lengths are $x = O_1N$ and $y = O_2N$.

By noting that $x' = x \cos(i)$ the projected separation becomes

$$\delta^2 = x'^2 + y'^2 = a^2[\cos(i)^2 \cos(\phi)^2 + \sin(\phi)^2] \quad (2.36)$$

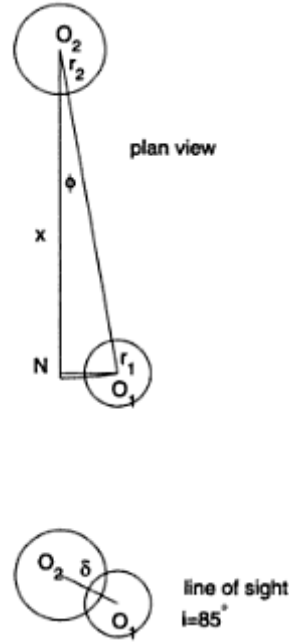


Figure 2.7 – *Plan view*: The two stars are located at O_1 and O_2 and have radii r_1 and r_2 , respectively. They are separated by a distance $a \equiv 1$ and are seen at a phase angle ϕ . *Line of sight*: Here the overlapping of the two stars are seen at an inclination of $i = 85^\circ$. The projected separation is given by δ at a given phase angle ϕ . Credit: Hilditch (2001).

This can be rewritten by defining the separation between the two stars as the unit of length, $a \equiv 1$.

$$\delta^2 = \cos(i)^2 + \sin(i)^2 \sin(\phi)^2 \quad (2.37)$$

By defining a quantity called the geometrical depth, $p_{\text{geo}} = (\delta - r_2)/r_1$, and the ratio of the radii, $k = r_2/r_1$, such that $k \leq 1$, we can get a new expression for the projected separation $\delta = r_1(1 + k p_{\text{geo}})$. This gives us the following relation

$$\cos(i)^2 + \sin(i)^2 \sin(\phi)^2 = r_1^2(1 + k p_{\text{geo}})^2 \quad (2.38)$$

This equation gives a direct link between the orbital inclination, i , the ratio of the radii, $r_{1,2}$, the geometrical depth, p_{geo} , and the orbital phase, ϕ . At the four different points of contact in the eclipse, p_{geo} will be equal to $+1, -1, -1$ and $+1$, respectively. If the orbit is eccentric the general expression for δ will take the following form

$$\delta = \frac{1 - e^2}{1 + e \cos(\theta)} [1 - \sin(\theta + \omega)^2]^{1/2} \quad (2.39)$$

which means that there are two more parameters which need to be evaluated, namely, e and ω . However, if $i \sim 90^\circ$ the following expressions are valid

$$\frac{2\pi(t_{\text{sec}} - t_{\text{pri}})}{P} = X - \sin(X) \quad (2.40)$$

where

$$X = \pi + 2 \arctan \left(\frac{e \cos(\omega)}{(1 - e^2)^{1/2}} \right) \quad (2.41)$$

and

$$e \sin(\omega) = \frac{d_{sec} - d_{pri}}{d_{sec} + d_{pri}} \quad (2.42)$$

Here t_{pri} and t_{sec} represents the time of primary and secondary eclipse. d_{pri} and d_{sec} are the durations of the two eclipses which will be the time between first and fourth contact³. By using Eq. 2.40 and 2.42 one is able to determine e and ω purely from the photometric observations of the light curve, noted that $i \sim 90^\circ$. This gives independent estimates of e and ω , which can be compared with the ones obtained from radial velocity measurements.

2.2.2 Modeling light curves

In order to get the parameters $r_{1,2}$ and i from a light curve, we need to know the relation between p_{geo} and the actual amount of light which is lost at any phase angle within an eclipse. If both of the stars were uniformly illuminated this would be an easy task. However, there are different effects which will cause the stars to vary in brightness across their stellar surface. All effects which will have an impact on the light curve will be addressed in Section 2.5.

The basic idea behind the modeling of a light curve, is that we will have a non-uniformly illuminated stellar disk which will have a surface brightness, I_1 , at any point on the projected stellar disk. The total brightness of the entire apparent stellar disk is then obtained by integrating over this area which will be a surface integral over the stellar surface which is then

$$l_1 = \iint_S I_1 dS \quad (2.43)$$

The next step is then to calculate the amount of light which is lost during any phase of an eclipse which can be written as

$$\Delta l_1 = \iint_S I_1 d\sigma \quad (2.44)$$

where the integral is taken over the eclipsed area of the star and $d\sigma$ is an element of area on the eclipsed stellar disk. The fractional loss of light, δf_1 , for star 1 when it is eclipsed by star 2 will be

$$\delta f_1 = \frac{\Delta l_1}{l_1} \quad (2.45)$$

When it comes to modeling light curves there are a lot of parameters which defines the light curve. These parameters will be discussed in the next section, but for now

³Hilditch (2001), page 238.

we will just list them here: the mean radii of the two stars, $r_{1,2}$, expressed in terms of the semimajor axis of the relative orbit; the orbital inclination, i ; the mass ratio of the two stars $q = m_2/m_1$; the temperatures $T_{1,2}$; the albedos $\alpha_{1,2}$; the gravity darkening exponents $\beta_{1,2}$; and the limb darkening coefficients $u_{1,2}$. The variations in flux relative to an adopted level for a light curve model are then given by

$$\Delta f = \Delta f(r_{1,2}, i, q, T_{1,2}, \alpha_{1,2}, \beta_{1,2}, u_{1,2}) \quad (2.46)$$

which will consist of minimum 12 parameters. The most dominant parameters in these light curve models will be the ones which define the shapes and sizes of the stars, $(r_{1,2}, q)$, the orbital inclination i , and the ratio of the stellar surface brightnesses.

2.3 Roche model

In section 2.1 the two stars were regarded as point masses which are of course not a true representation of the stars. A binary star will experience tidal distortion from its companion and rotational flattening due to rotation about its own rotational axis which will cause the shape of the star to be non-spherical. The tidal torques will cause the rotational axes of the stars to become aligned perpendicular to the orbital plane of the binary system. Furthermore the tidal torques will also enforce the rotational periods of the stars to become equal to the orbital period, and over time also cause an elliptic orbit to become circular. The rotation of the stars about their own axis will cause the polar radius to become smaller than the equatorial radius. For elliptic orbits, the distortions of the stars will create perturbations to the Newtonian gravitational theory. These perturbations will be the rotational potential created by the star spinning around its rotational axis, the tidal potential exerted on each of the stars by its companion and the general relativity correction to Newton's equations. These corrections will cause what is called apsidal motion, which is the precession of the orbit in its own plane⁴. In other words, ω will not be constant but will change over time which can be observed in several binary systems.

Binary systems come in various configurations and will evolve quite differently depending on their relative separation and mass. During a star's evolution, its radius will change quite substantially and in some binary systems the two binary stars will actually touch each other's surfaces and even exchange mass. It is therefore very important to use a formulation which can describe the shape of the stars due to the perturbations which they experience. That formulation is the Roche model, which is based on the consideration of the gravitational potential in a system of two point masses that move in circular orbits about their barycentre. The systems which are considered in the Roche model, are the ones where the tidal torques will have had enough time to cause the binary orbit to become circular and tidally locked in synchronous rotation. The time scales for synchronization and circularization are quite different for stars with convective envelopes

⁴Hilditch (2001), page 132.

and radiative envelopes. The stars of V80 are in the mass range where they will have convective envelopes illustrated by Figure 2.8. The time scale for stars with convective envelopes from Zahn (1977) are given as

$$t_{sync} \approx q^{-2} \left(\frac{a}{R}\right)^6 \approx 10^4 \left[\frac{1+q}{2q}\right]^2 P^4 \text{ years} \quad (2.47)$$

$$t_{circ} \approx \frac{2}{q(1+q)} \left(\frac{a}{R}\right)^8 \approx \frac{10^6}{q} \left[\frac{1+q}{2}\right]^{5/3} P^{16/3} \text{ years} \quad (2.48)$$

where q is the mass ratio of the two stars, a is the semimajor axis, R is the radius of the star and P is the orbital period in days. These equations are strongly dependent on the orbital period, a and R which means that binary systems with short periods and low relative separation will have short time scales for synchronization and circularization of their orbits.

2.4 Blackbody radiation

The radiation emitted from a star is approximately described by black body radiation which is a function of temperature T and frequency ν . Planck's law of black body radiation is given by

$$B(\nu, T) = \frac{2h\nu^2}{c^2} \frac{1}{e^{h\nu/k_b T} - 1} \text{Wm}^{-2}\text{Hz}^{-1}\text{sterad}^{-1} \quad (2.49)$$

where c is the speed of light, h is the Planck constant and k_b is the Boltzmann constant. The light curve of a binary system is very dependent on the projected surface of the stars. If the stars are highly non-spherical the light curve will not be constant between eclipses since the projected surface of the stars will vary during the binary orbit. For detached binary systems, the relative radii, $r = R/a$, are below 0.1 which means that they can be considered nearly spherical which means that they will have little or no variations in their light curve between eclipses. This is of course not true if the system is magnetically active like the case of V80.

2.5 Light curve perturbations

We are now going to go through the minor effects which also will affect the shape of the light curve. Even though these effects do not dominate the overall shape of the light curve, they are still important when one wants to derive precise and correct parameters from the light curve such as i and $r_{1,2}$.

2.5.1 Limb darkening

Limb darkening is a consequence of optical depth, and how this varies across the stellar disk. Optical depth gives information about the amount of light that can travel through

a gas without being absorbed or scattered by the interacting matter. When the photons in the star's interior travel towards the stellar surface, the extent to which they are getting absorbed is determined by the optical depth, which is $\Delta\tau = \kappa\rho\Delta s$. Here Δs is the distance the photon has to travel through the medium, ρ is the density of the medium and κ is the opacity, also known as the mass absorption coefficient. When $\Delta\tau \gg 1$, the medium is said to be optically thick and the photons will quickly collide with the medium and thereby get absorbed. When $\Delta\tau \ll 1$ the medium is optically thin and photons will travel freely without getting absorbed. When we look at a star, we can only see to a certain depth before the star becomes opaque. The optical depth of unity is where $\Delta\tau = 1$, which is where the stellar surface is defined to be. This is also where the effective temperature of the star, T_{eff} is observed⁵. The intensity loss for an object which light passes through a given medium of optical depth $\Delta\tau$, at a frequency ν is given by

$$I_\nu = I_{\nu,0} \cdot e^{-\Delta\tau} \quad (2.50)$$

where $I_{\nu,0}$ is the initial intensity.

When we observe a star, the observed photon flux will differ across the stellar disk, as the photons will have to travel through different layers of gas before escaping the star. The observed flux will decrease as we go from the center towards the limb of the star.

2.5.2 Gravity darkening

Gravity darkening is a consequence of the non-spherical shape of a star and is therefore linked to the Roche model described in Section 2.3. The emergent flux from the stellar surface is proportional to g^β , where β is the gravity darkening exponent and g is the local gravity. The emergent flux will increase with increasing surface gravity which means that the equator of a star will be darker than at its poles⁶.

2.5.3 Reflection and heating

When the binary stars move around in their orbit they will radiate on each others surfaces. The irradiated surface will then either reflect or absorb the radiation. If the radiation is absorbed it will increase the surface temperature resulting in an increase of the flux coming from its surface. The difference between reflection and heating is determined by the surface temperature of the irradiated star. For a temperature of $T \sim 4000$ K, the radiation is completely absorbed by the atoms and ions in the irradiated atmosphere which causes the surface temperature to rise. In this scenario the albedo, α , will be 1. For temperatures of $T \sim 30000$ K, the density of free electrons

⁵Stahler and Palla (2008), page 47.

⁶Hilditch (2001), page 243.

in the atmosphere will be much higher which will result in 50% of the radiation being Thomson scattered and thereby causing the radiation to be reflected⁷. The last 50% of the incoming radiation will be absorbed in the atmosphere which means that the albedo in this scenario will be $\alpha = 0.5$.

2.6 Stellar evolution in Detached Binary systems

As mentioned in the introduction, detached eclipsing binary systems are of fundamental importance to stellar physics and the study of stellar evolution models since they are the only stars for which we can precisely and accurately measure quantities such as mass, radius and surface gravity. Detached eclipsing binary systems can be used to test stellar model isochrones and estimate stellar parameters such as age with tight constraints. In order to better understand what affects isochrone models, we are going to go through and explain some of these effects. The main determinant of a star's evolution is its mass which determines the stellar core temperature and thereby the burning rate of hydrogen fusion. Other than the mass, there are effects such as the mass fraction of hydrogen X and helium Y , the abundance of heavy elements which is linked to $[\text{Fe}/\text{H}]$, diffusion of heavy elements and the abundances of C, N and O.

2.6.1 Stellar abundances and $[\text{Fe}/\text{H}]$

The abundance of X and Y together with $[\text{Fe}/\text{H}]$ will determine the stars properties and how the star evolves. If the helium abundance is fixed, increasing $[\text{Fe}/\text{H}]$ will increase the opacity which will lower the luminosity and effective temperature of the star. Isochrones for different $[\text{Fe}/\text{H}]$ with constant $Y = 0.30$ for NGC 6791 are shown in Figure 6 in Brogaard et al. (2012) and demonstrate that increasing $[\text{Fe}/\text{H}]$ will result in the stars being cooler and having smaller radii. Increasing Y while decreasing X at fixed $[\text{Fe}/\text{H}]$ will result in an increase in the mean molecular weight which will cause the pressure in the stellar core to decrease. This will cause the stellar core to contract and increase in temperature which will increase the rate of hydrogen burning and thereby decrease the time on the main-sequence for the star. Increasing $[\text{Fe}/\text{H}]$ and holding Y constant or vice versa can ultimately lead to the same result in the Color-Magnitude-Diagram (CMD). It can therefore be hard to set tight constraints for Y when comparing stellar models to CMDs of clusters if one does not have any binary systems to constrain the models with.

2.6.2 The CNO cycle

C, N and O can act as a catalyst in the hydrogen burning phase which will speed up the depletion of hydrogen in the stellar core and thereby cause the star to go through its main-sequence phase much faster. The energy generation rate from the CNO cycle is much more temperature dependent than the energy generation rate from the PP-chains. As a result of this, the PP-chains dominate at low temperatures whereas the CNO cycle

⁷Hilditch (2001), page 244.

is dominant at relatively high temperatures⁸. Because of this, the CNO cycle is much more effective in high mass stars which have higher core temperatures and will not be as significant for the isochrone of low mass stars.

2.6.3 Energy transport and mixing length parameter

There are two kinds of energy transport which can occur in a star, namely, radiative and convective energy transport. The stellar mass is a dominant factor in determining where the different energy transports dominate in the stellar interior. The energy transport which will be dominant in a specific region of a star, will be the energy transport which has the greatest temperature gradient ∇ . One can divide the stars up into three categories which gives a general picture of how convection and radiation dominate in different zones for main-sequence stars. This can be seen in Figure 2.8 where convection zones are represented by the curly grey areas.

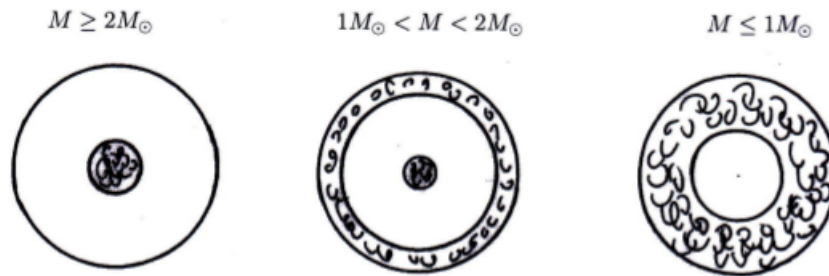


Figure 2.8 – A general picture of how convection and radiation dominate in different zones for main-sequence stars. Convective zones are represented by curly grey areas. Credit: Dalsgaard (2008).

In stellar models, convection is usually described by the Mixing-Length Theory, which makes use of the mixing length scale in order to express the convective flux, velocity and temperature gradients of the convective elements and stellar medium. A simple explanation goes as follows:

A blob of stellar plasma that is unstable will transport its energy by convection. After a typical mixing length distance l_m it dissolves into its surroundings and deposits its energy there. l_m is determined by the mixing-length-parameter α_{MLT} by $l_m = \alpha_{\text{MLT}} H_P$, where H_P is the pressure scale height.

Using a lower value of α_{MLT} in stellar modeling decreases the physical distance that a blob of plasma will travel before it dissolves into its surroundings. There is no physical model which can determine α_{MLT} , so it must be determined by comparing stellar models to a calibrator, the Sun. The mixing-length-parameter is not necessarily the same in

⁸Further information can be found in Dalsgaard (2008), Section 8.5.

all stars and at all evolutionary stages. Because of this, Trampedach and Stein (2011) have made theoretical predictions for the variation of the mixing-length-parameter as a function of T_{eff} and $\log(g)$ based on 3D convection simulations. Even so, the mixing-length-parameter contributes a certain uncertainty to stellar models⁹. Decreasing the value of α_{MLT} will generally decrease the effective temperature and increase the radius of a star. In order to get magnetically active binaries to match the same stellar parameters, α_{MLT} is sometimes changed from that of the solar calibration for one or both of the components. This was done for V636 Centauri in Clausen et al. (2009) where the initial mixing-length-parameter was calibrated to a solar value of $\alpha_{\text{MLT}} = 1.68$. However, the best match of α_{MLT} for the primary and secondary components, corresponding to an age of 1.35 Gyr, were $\alpha_{\text{MLT}} = 1.4$ and $\alpha_{\text{MLT}} = 1.0$, respectively.

It is worth to mention that Pasetto et al. (2014) have presented a self-consistent analytical formulation of stellar convection that determines the properties of stellar convection as a function of physical behaviour of the convective elements themselves and the surrounding medium. If this new analytical formulation is indeed correct, it would eliminate the need for a free parameter in stellar modeling which should greatly improve these models. The predictions of this new theory is in agreement with the Mixing-Length Theory made for the Sun and it would be very interesting to see how this model compares to the Mixing-Length Theory for other stars.

The diffusion of heavy elements also plays a role in stellar modeling. As a star ages on the main-sequence, the diffusion of heavy elements will deplete in the outer part of the star, i.e. $[\text{Fe}/\text{H}]$ at the stellar surface will be lower than the initial $[\text{Fe}/\text{H}]$. Convective motion can however reduce this effect by turbulent mixing. As the star leaves the main-sequence its convection zones deepens and brings the heavy elements back up to the stellar surface. $[\text{Fe}/\text{H}]$ can even increase so much that it becomes greater than the initial values as seen in Figure 2.9 from Brogaard et al. (2012). This is however not because of a higher abundance of Fe but because of a change in Y in the stellar envelope. In Figure 2.9 an isochrone which includes heavy element diffusion and turbulent mixing has been compared to stars from NGC 6791. The initial metallicity is $[\text{Fe}/\text{H}] = +0.35$, $Y = 0.30$ and the color excess is $E(B-V) = 0.15$. The current atmosphere $[\text{Fe}/\text{H}]$ values for each star is given in the left panel, while the difference from the initial $[\text{Fe}/\text{H}]$ is shown in the right panel.

⁹Pasetto et al. (2014), page 1

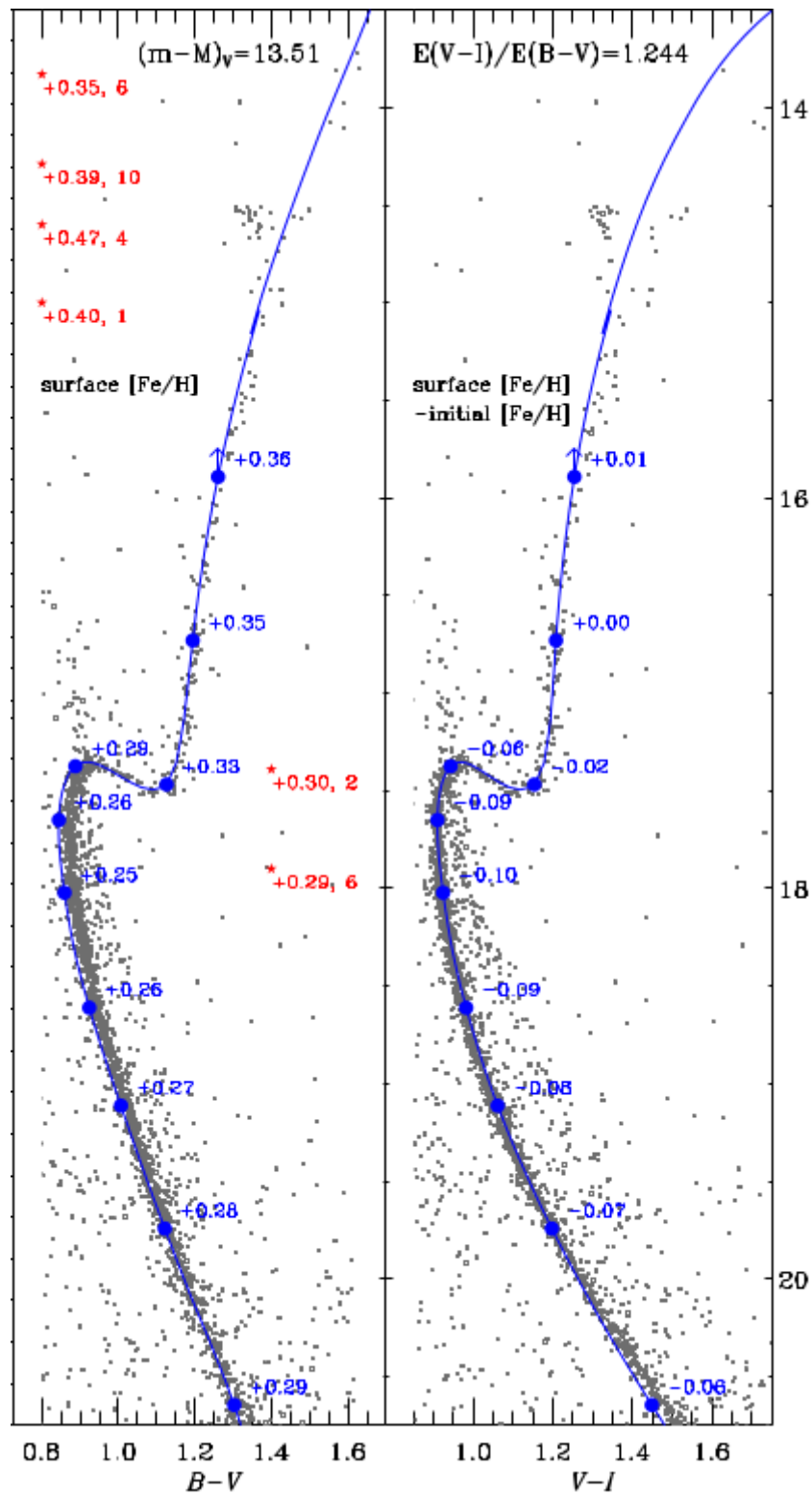


Figure 2.9 – Here the change in heavy element diffusion can be seen for the cluster members of NGC 6791 where $[Fe/H]$ is increased to higher values than the initial $[Fe/H]$ due to turbulent mixing. Credit: Brogaard et al. (2012).

3. *Data*

In this chapter we are going to go through the data we use for the investigation of V80 which will include the light curves from the Kepler Space Telescope, but also the R and V light curves and spectroscopic analysis from Brogaard et al. (2011). We will briefly describe the Kepler Mission and how the light curve data extraction of V80 was done. After that, we will go through the photometry and spectroscopy done for V80 in Brogaard et al. (2011).

3.1 The Kepler Space Telescope

The Kepler Space Telescope is designed for the Kepler Mission which was launched in 2009 with the goal of finding Earth-sized planets in the habitable zone around main-sequence stars using the transit method. The Kepler Mission is designed to survey our region of the Milky Way galaxy in order to explore the structure and diversity of planetary systems by staring at the same area of the sky, looking at more than 100 000 stars. Since the transit signal from an Earth-sized planet eclipsing its host star is very weak, producing a change in brightness of only 100 ppm (parts per million), the Kepler Space Telescope needs to be very sensitive. The combined differential photometric precision over a 6.5 hour integration is less than 20 ppm (one sigma) for a 12th magnitude solar-like star, where a stellar variability of 10 ppm is also assumed. Even though the dynamic range of the Kepler Space Telescope is in the range of 9th to 16th magnitude stars for the hunt of Earth-sized planets, the high photometric precision also makes it excellent for observing light curves of binary systems.

Because the Kepler telescope has to monitor 100 000 stars, it requires a very large field of view of 105 square degrees which can be seen in Figure 3.1. The primary mirror is 1.4 meter in diameter with 21 modules each with two 2200×1024 pixel CCDs, resulting in detectors of 95 mega pixels. The instrument has a spectral bandpass in the range 430 - 890 nm FWHM¹.

The Kepler Mission was scheduled to last 3.5 years, which was extended another 4 years on April 4th 2012². However on August 15th 2013 the Kepler Space Telescope

¹Full Width Half Maximum.

²<http://www.nasa.gov/centers/ames/news/releases/2012/12-33AR.html>

team announced that two of the four gyroscope-like reaction wheels which is used to keep the spacecraft steady and pointing in the right direction, had ceased to work³. The first gyroscope was lost in July 2012 and the second in May 2013. The Kepler Spacecraft needs three of its four gyroscopes in order to function but since the actual telescope is still operating completely fine, the Kepler Space Telescope team announced that they would be looking for what new science the Kepler Space Telescope could be used for.

On the 16th of May 2014 NASA approved a new mission for the Kepler telescope, called the K2 mission. The K2 mission recieved funding for two years of exoplanet search, together with new scientific observation opportunities to observe notable star clusters, young and old stars, active galaxies and supernovae. The K2 mission uses the radiation pressure from the sun as a third gyroscope in order to keep the Kepler spacecraft steady. The K2 mission will observe targets along its orbital plane (approximately the ecliptic) in order to minimize the impact from the radiation pressure of the Sun. This will be done for approximately 83 days before it is necessary to rotate the spacecraft to prevent sunlight from entering the telescope⁴.

With the Kepler Mission having observed more than 100 000 stars, there is still alot of data to be processed, together with follow-up observations which need to done. So far the Kepler Mission has discovered 978 exoplanets and 2165 binary systems, together with 4234 exoplanet candidates which still need to be investigated further.

³<http://kepler.nasa.gov/news/nasakeplernews/index.cfm?FuseAction=ShowNewsNewsID=292>.

⁴<http://kepler.nasa.gov/news/nasakeplernews/index.cfm?FuseAction=ShowNewsNewsID=339>.



Figure 3.1 – Kepler field of view. Credit: <http://kepler.nasa.gov/images/MilkyWay-Kepler-cRoberts-1-full.png>.

3.2 Kepler light curve data

3.2.1 Kepler data and extraction of data

The data extraction from Kepler can be done from the following link: http://archive.stsci.edu/kepler/data_search/search.php, where V80 has the Kepler ID, also called KIC number, 2438061. The light curve data from Kepler are packed as FITS binary table files with a primary header, a light curve extension and an aperture extension. The Kepler instrument consist of 42 CCDs arranged in 21 modules. The half-maximum bandpass is 435 to 845 nm, with $> 1\%$ relative spectral response as short as 420 nm and as long as 905 nm. Each CCD has the size of 50×25 mm with 2200×1024 pixels, with a readout time of 0.5189485261 seconds and an exposure time of 6.019802903 seconds. On every integration all the pixels are read out, and temporally summed in the Science Data Accumulator (SDA). On average 32 pixels are read out of the SDA per target. There are two kinds of flux time series, the long cadence and the short cadence. The short cadence data are summed into a total exposure time of 30 minutes (270 integrations), while the short cadence are summed into one minute sums (9 integrations)⁵. The light curve files for V80 consist of 11 long cadence files and one short cadence file.

3.2.1.1 Light Curve Binary Extension

The light curve binary Extension consists of several data columns, where our primary focus will be on the following: TIME and PDCSAP_FLUX.

TIME

The data column named "Time" contain the time at the mid-point of the cadence in BKJD (Kepler Barycentric Julian Day). BKJD is Julian day minus 2454833.0 (UCT = January 1st, 2009 12:00:00) and is corrected to be the arrival times at the barycenter of the Solar System. In order to transform BKJD into BJD (Barycentric Julian Date), the Kepler pipeline uses the right ascension and declination of the object, which can be found in the header. V80 is located at a right ascension of 290.277020° and a declination of 37.790970° . The conversion can be done by using the following formula for each member of the time series [i]:

$$\text{BJD}[i] = \text{TIME}[i] + \text{BJDREFI} + \text{BJDREFF} \quad (3.1)$$

where BJDREFI and BJDREFF are giving as keywords in the header.

PDCSAP_FLUX

The light curve file contains two columns with flux called SAP_FLUX and PDCSAP_FLUX where each has a corresponding column of flux errors. SAP_FLUX is the flux in electrons per second contained in the optimal aperture pixels collected by the spacecraft. The difference between SAP_FLUX and PDCSAP_FLUX is that the PDCSAP_FLUX

⁵Kepler Archive Manual, page 7. http://archive.stsci.edu/kepler/manuals/archive_manual.pdf

has undergone further analysis. The Presearch Data Conditioning (PDC) module of the Kepler data analysis pipeline removes signatures in the SAP_FLUX light curve that are correlated with systematic error sources from the telescope and spacecraft. This includes pointing drift, focus changes and thermal transients⁶. PDC tries to remove these errors while still preserving planetary signals and other interesting astrophysical phenomena. The PDCSAP_FLUX light curve column will therefore be used to investigate V80 instead of the SAP_FLUX column since this should yield better results.

3.2.1.2 Aperture Extension

For each target Kepler only acquires the pixels contained within a predefined mask which is used to produce the light curve files. The aperture extension consists of a single image that describes which pixels were collected by the spacecraft, which pixels are contained in the optimal aperture and which pixels were used to calculate the centroids. The pixels which were used in the optimal aperture are used to create the SAP_FLUX light curve.

3.2.2 Target Pixel Data

For each light curve file there exists a target pixel data file. Each file consists of a header, a target table extension and an aperture extension. The target table extension contains flux time series for both the raw and calibrated pixels where the pixel values are encoded as images. The aperture extension contains a single image describing the target pixel mask and optimal aperture. For further information on the light curve files and target pixel data, see the Kepler Archive Manual⁷.

3.3 Brogaard et al. 2011

V80 was first investigated by Brogaard et al. (2011) together with the two other binary systems V18 and V20 located in NGC 6791. We will in this section go through the photometry and spectroscopy obtained for V80 in Brogaard et al. (2011) which we are going to use in conjunction with the Kepler light curves.

3.3.1 Photometry

The photometric data for V80 consists of V (Johnson) and R (Cousins) CCD observations acquired from the 2.56 m Nordic Optical Telescope (NOT) and its ALFOSC instrument over 9 nights in the period between May and August 2009. This resulted in 580 exposures (V) with an exposure time of 240 s and 538 exposures (R) with an exposure time of 180 s.

In Brogaard et al. (2011) the V and R band light curves were not good enough to

⁶Kepler Archive Manual, page 21.

⁷http://archive.stsci.edu/kepler/manuals/archive_manual.pdf

put the strong constraints on the photometric parameters of V80 which binary systems otherwise are known for. The reason for this being the magnetic activity and the limited amount of light curve measurements. In order to obtain measurements of the surface gravity, $\log(g)$, which was to be used for T_{eff} and $[\text{Fe}/\text{H}]$ measurements, Brogaard et al. (2011) performed preliminary light curve analysis for V80. The V and R band light curves had offsets in magnitude between each eclipse due to the magnetic activity which they corrected for such that all observations between eclipses were aligned in magnitude. They then found light curve solutions employing a V band light ratio constrain from their Color-Magnitude-Diagram (CMD) of the cluster NGC 6791. The results from Brogaard et al. (2011) can be seen in table 3.1, where the uncertainties are in the range of 6 – 20 %.

Parameter	Value
Constraints from CMD:	
$L_s/L_p(V)$	0.15 ± 0.05
Measured parameters:	
i ($^\circ$)	84 ± 1
r_p	0.0900 ± 0.0054
r_s	0.061 ± 0.012

Table 3.1 – Photometric solution of V80 found in Brogaard et al. (2011).

3.3.2 Spectroscopy

The spectroscopic observations were carried out in service mode with UVES at the ESO Very Large Telescope (VLT) during allocation period 81. The standard 580 nm setup was used for UVES (Ultraviolet and Visual Echelle Spectrograph), together with an on-chip binning of 2x2 pixels. The wavelength ranges which is covered by the two CCD detectors in UVES are 477.5-575.0 nm and 587.5-683.0 nm. The observations at VLT resulted in 10 usable epochs for V80 which can be seen in the spectroscopic double-lined orbital solution for V80 in Figure 3.2. From these measurements the semiamplitude of the primary and secondary components of V80 was found to be $K_p = 66.05 \pm 0.16$ and $K_s = 87.38 \pm 0.26$ km s $^{-1}$, respectively.

V80 Primary	
T_{eff}	5600 ± 95 K
$\log(g)$	4.21
$v \sin(i)$	14.00 ± 2.00 km s $^{-1}$
v_{micro}	1.10 ± 0.10 km s $^{-1}$
$[\text{Fe}/\text{H}]$	$+0.34 \pm 0.10$

Table 3.2 – Parameters determined from spectral analysis, where $\log(g)$ was fixed.

3.3.3 Absolute dimensions

By using the parameters from the preliminary light curve analysis and the spectroscopic analysis Brogaard et al. (2011) found the astrophysical data for V80 which can be seen in Table 3.3.

	Primary	Secondary
M/M_{\odot}	1.0588 ± 0.0091	0.8003 ± 0.0062
R/R_{\odot}	1.341 ± 0.081	0.90 ± 0.18
$\log(g)$ [cgs]	4.208 ± 0.052	4.43 ± 0.18
T_{eff} [K]	5600 ± 95	(...)
v_{rot} [km s ⁻¹]	14.1 ± 2.00	(...)
v_{sync} [km s ⁻¹]	13.88 ± 0.83	9.33 ± 1.9

Table 3.3 – Absolute dimensions of V80 found from Brogaard et al. (2011). v_{rot} is the observed equatorial rotational velocity and v_{sync} is the theoretical equatorial velocity for synchronous rotation.

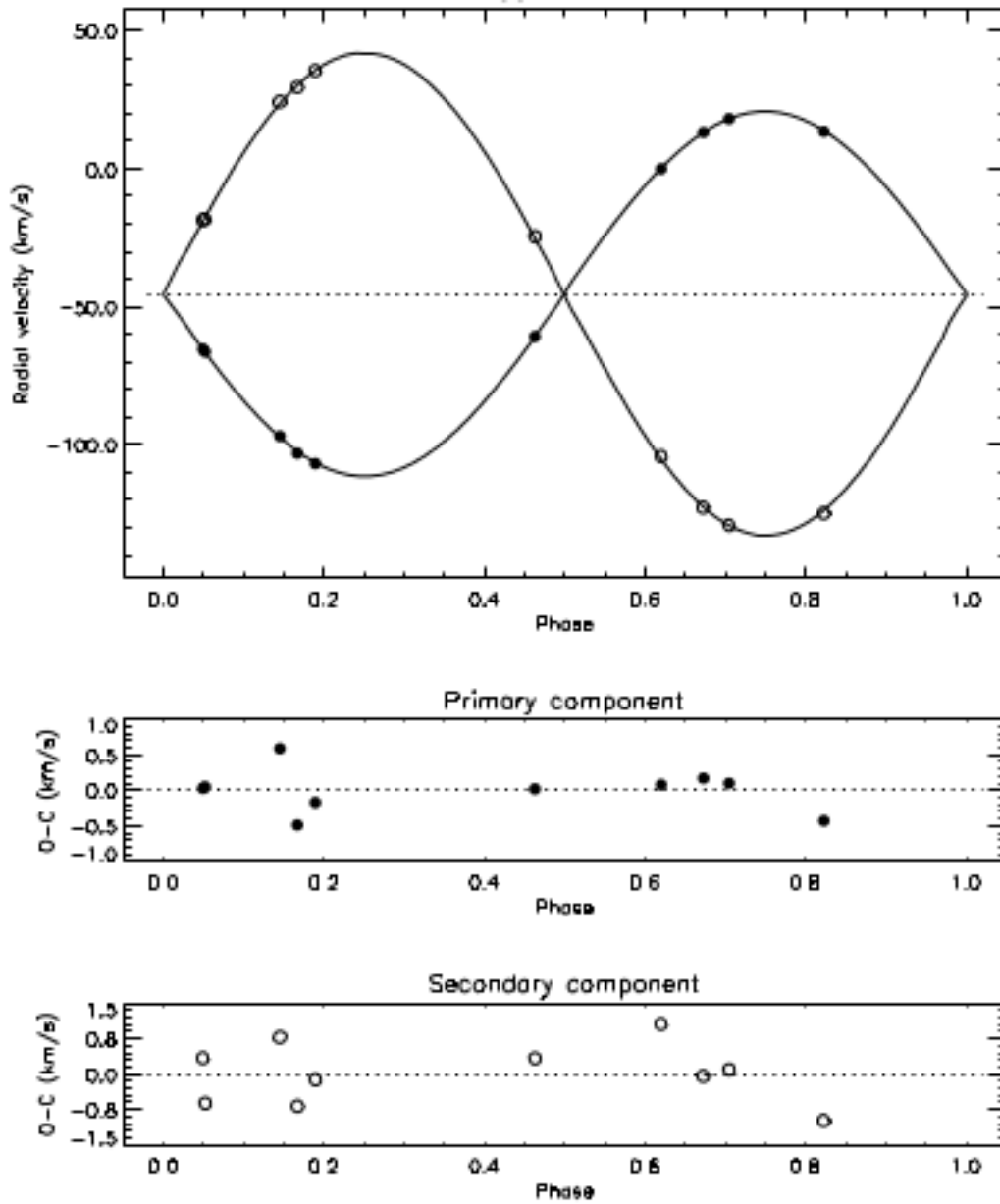


Figure 3.2 – The spectroscopic double-lined orbital solution for V80 from Brogaard et al. 2011. The horizontal dotted line in the upper panel represents the system velocity of V80. Credit: Brogaard et al. (2011).

4. *Data analysis*

In this chapter we will describe the data analysis which has been done to the Kepler long and short cadence light curves and the R and V band light curves from Brogaard et al. (2011). During the data analysis we will address the effects which is observed in the light curve and how these are removed or interpreted.

4.1 Starspot period

The light curve data of V80 from Kepler shows high magnetic activity indicated by the fact that it is not constant outside eclipses which can be seen in Figure 4.1. In order to analyse the system the light curve variations caused by the magnetic activity needs to be removed. Before the removal of the light curve variations, it is interesting to see if the variations are periodic and if so, what the period is. If one looks closely, the eclipses are out of synchronization with the variations of the magnetic activity. In order to investigate the period of the light curve variations we use a program called `pdm2.pro`¹. The program computes a χ^2 statistic for period searching in time-series data which is based on the technique called Phase Dispersion Minimization (PDM) described in Stellingwerf (1978).

The Kepler Spacecraft rotates 90 degrees every quarter of the year in order to keep the solar arrays oriented towards the Sun and to make sure that the radiator is pointed towards deep space². Because of this, the Kepler objects are observed by four different CCDs during a year. This means that the light curves from the different quarters will not lie at the same flux level due to the effects of CCD read-out-noise, dark current and pixel-to-pixel variations³. The rotation of the Kepler Spacecraft means that the light curves from each quarter need to be normalized. After we normalize the light curves, the time series are converted to phases of the orbital period of the system using the period found in Brogaard et al. (2011). In Brogaard et al. (2011) the orbital period was estimated to be 4.88594 ± 0.00016 days with a time of primary eclipse found to be at 54652.3045 (HJD-2 400 000) which converted to BJD is 54652.3052 (BJD - 2 400 000). The conversion is done in order to compare the time of primary eclipse with the Kepler

¹<http://www.astro.washington.edu/docs/idl/cgi-bin/getpro/library30.html?PDM2>

²Kepler Archive Manual, page 7.

³Howell (2006), page 78.

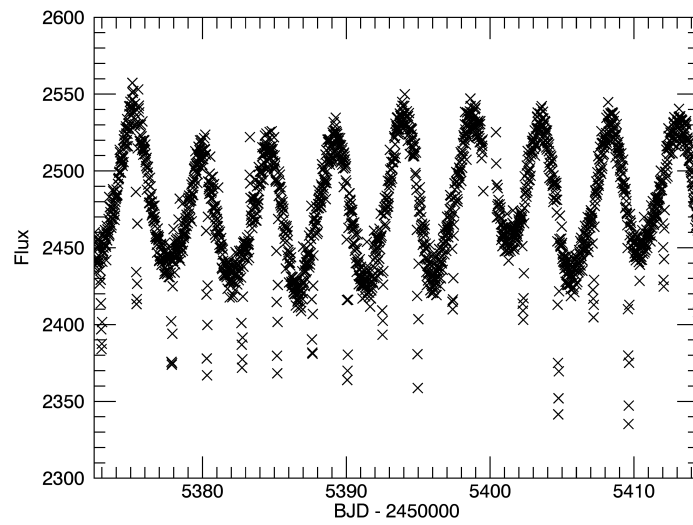


Figure 4.1 – A portion of the Kepler long cadence light curve is shown. The light curve is not constant outside of the eclipses due to what looks like a periodic light variation caused by magnetic activity which is not synchronized in time with the eclipses.

time series. In Figure 4.2 all the long cadence light curves can be seen, before and after the eclipses has been removed.

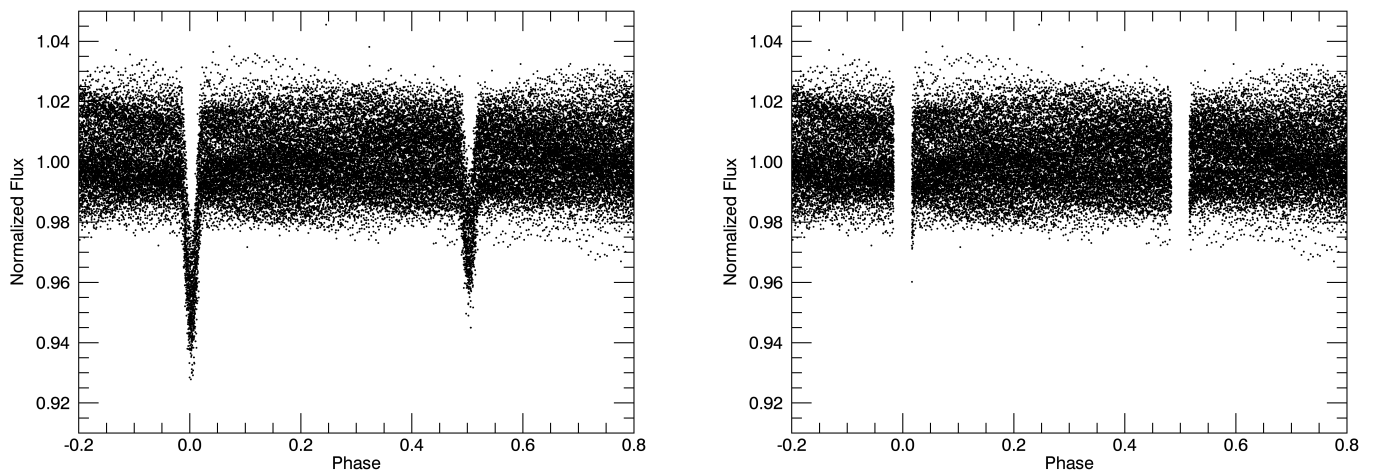


Figure 4.2 – The Phased light curves of the long cadence data can be seen to the left. To the right, the eclipses of the light curves have been removed.

After the removal of the eclipses, `pdm2.pro` can be used to find the period of the light curve variations caused by the magnetic activity. In Figure 4.3 the χ^2 fit is shown where a minimum can be seen. There also seems to be a local minimum, which could indicate that there could be yet another periodic signal in the light curve data. The period of the light curve variations caused by magnetic activity is estimated to be 4.738 ± 0.008 days which we through the thesis will refer to as the main starspot period. The uncertainty of the main starspot period is found by fitting a gaussian function to the minimum in Figure 4.3.

Now that the period of the primary signal in the Kepler light curve has been determined,

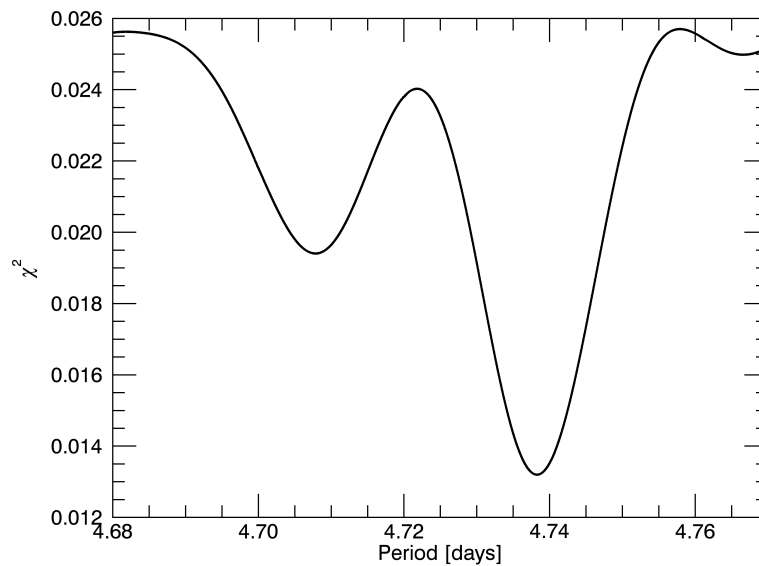


Figure 4.3 – Here the χ^2 fit shows a period of 4.7385 days for the magnetic activity, together with a local minimum at a period of 4.7078 days which indicate that the light curves contain more than one periodic signal.

we proceed by taking the light curves, still with the eclipses removed, and phasing them with the main starspot period and the secondary signal of 4.708 days. This can be seen in Figure 4.4 where the phase diagram for the main starspot period has been fitted with a sine function. The phase diagram for the secondary signal to the right in Figure 4.4 shows more spread of the data points compared with the phase diagram of the primary signal, especially in the interval of $[0.55; 0.75]$. For this reason, we only focus on the primary signal which seems to have a constant period.

To further investigate the phase diagram of the primary magnetic signal, we divide it up into four phase diagrams, one for each CCD. Each CCD is referred to as 0, 1, 2 or 3, where CCD0 corresponds to the quarters 0, 4, 8 and so forth. Figure 4.5 shows how

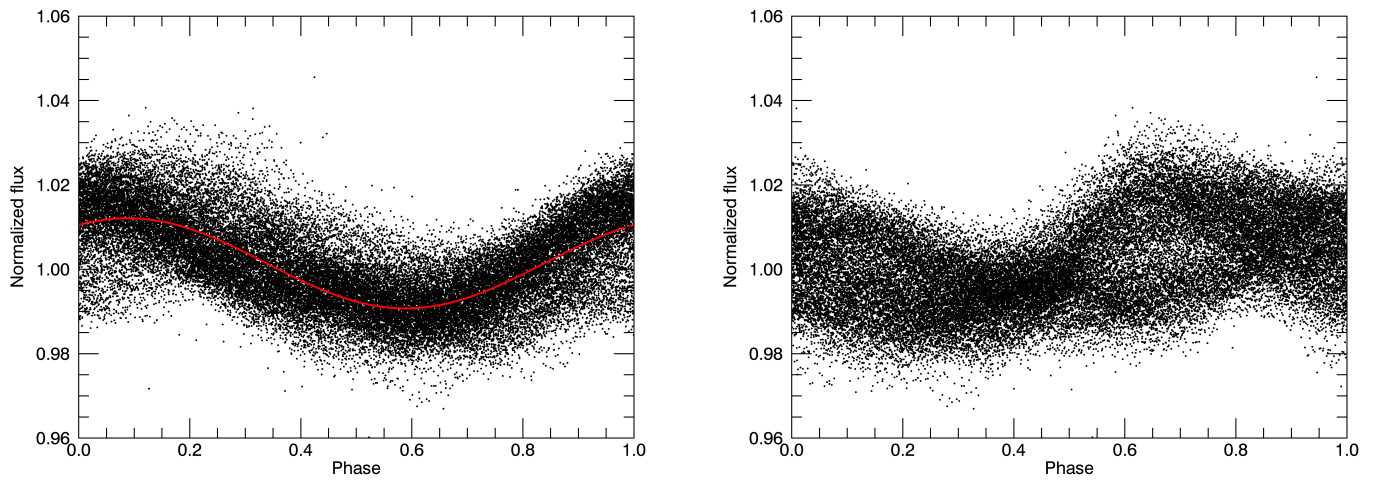


Figure 4.4 – *Left*: The long cadence light curves with the eclipses removed have been phased with the main starspot period, where a sine function has been fitted to the data. *Right*: This is the same scenario as on the left, but where the secondary signal of 4.708 days has been used to phase the light curves.

the magnetic signal is somewhat changing for each quarter. None of the CCDs represent data points which are good for a sine fit which means that the light curve variations caused by the magnetic activity is changing substantially over a year since this is the time difference for each quarter which has been observed with the same CCD.

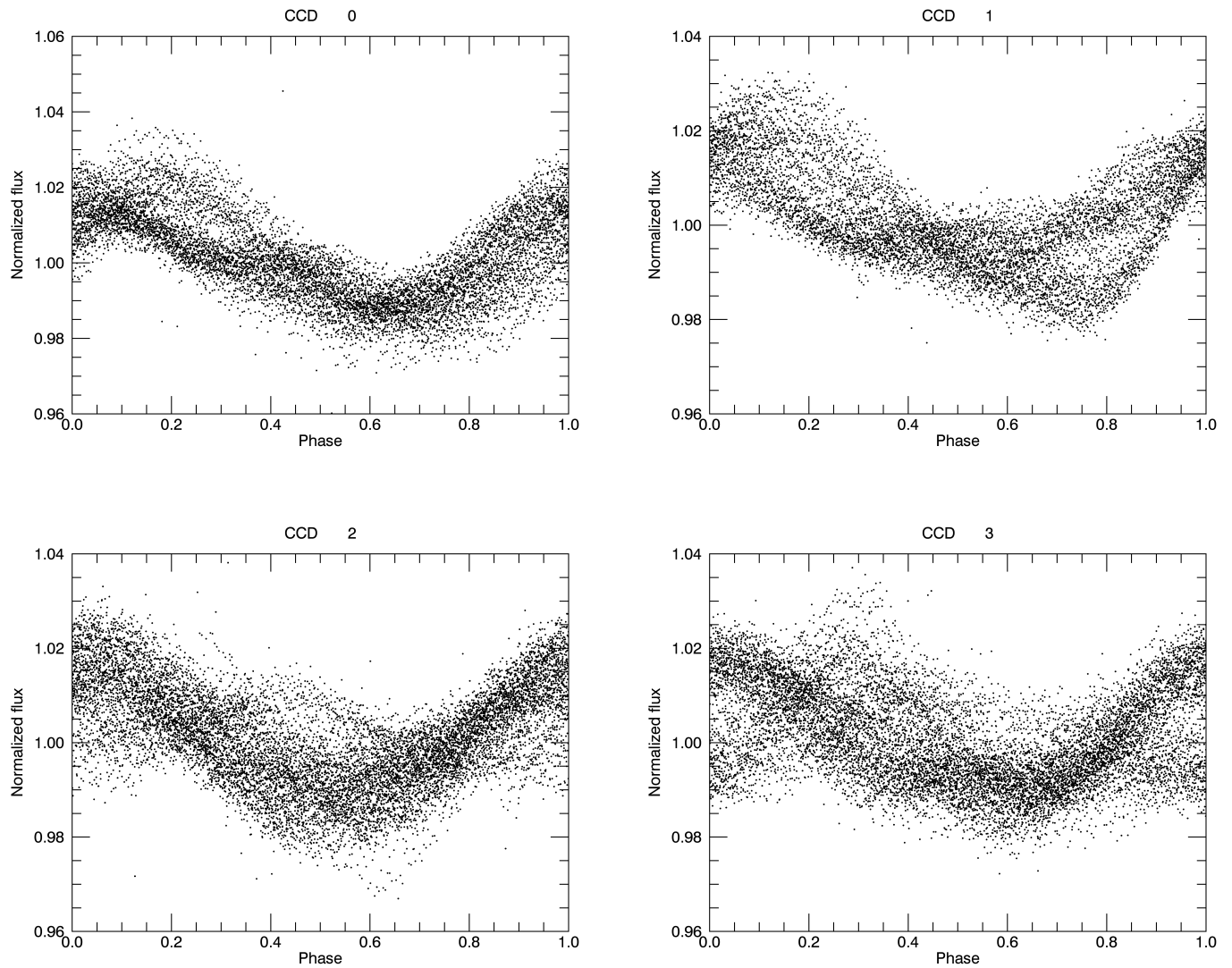


Figure 4.5 – Each quarter has been divided into the CCD which was used for observing V80. Each CCD is referred to as 0, 1, 2 or 3, where CCD 0 corresponds to the quarters 0, 4, 8 and so forth. All four plots show substantial changes for each quarter.

4.2 Orbital period of V80

4.2.1 Estimation of the orbital period of V80 from PDM

Even though the light curve variations caused by the magnetic activity might not be completely constant, we can still use the sine fit from Figure 4.4 to remove the overall shape caused by the magnetic activity from the light curve. By doing so, we can isolate the primary eclipses in the light curve and use the PDM method to get an estimate of the period of V80. The result is a period of 4.88586 days which is in agreement with the result found in Brogaard et al. (2011) where a orbital period of 4.88594 ± 0.00016 days was found. The PDM method does not provide an error estimation for the period of a given signal, so in order to get some idea about how well the period is determined and if there might be possible changes of the period, we need to use the Kwee Van Woerden method.

4.2.2 Kwee Van Woerden method

The code we construct for the Kwee Van Woerden method is written according to the original paper of Kwee and Van Woerden (1956) without any modifications which we use to estimate the time of minimum for a given light curve and its corresponding uncertainty. The method is highly used amongst eclipsing binaries since it does not require any assumptions about the shape of the light curve. The only downside about the Kwee Van Woerden method is that Mikulášek et al. (2013) showed that the method tends to underestimate the uncertainties of the corresponding mid-eclipse times.

The method assumes that the light curve is symmetric, where the time of mid-eclipse is found by folding the light curve about the estimated time of minimum. The correct time of minimum is found by altering the reflection axis until the difference between the square of the sum of each observation pair, $s(t) = \sum \Delta m^2$, is at its minimum. Here Δm is the difference between an observation pair and t is the estimated time of mid-eclipse. When a good estimate of the minimum of s is found, the values of $s(t \pm \Delta t)$ will be higher and these three points can be used to solve a second degree polynomial. The minimum of this polynomial will be the time of mid-eclipse.

4.2.2.1 Kepler long and short cadence data

For the long cadence data, each eclipse is covered by about 9 data points and the correct time of minimum is easily found by using the Kwee Van Woerden method. For the short cadence data it is not that easy. The short cadence data light curves consist of 30 times more data points than that of the long cadence light curves, but of significantly lower signal-to-noise ratio. Because of this, the reflection axis will produce local minima which will result in wrong estimates of the time of minimum for the short cadence data if the estimated time of minimum is not chosen wisely. A comparison of the short and long cadence light curves can be seen in Figure 4.6, where it is easy to see that the long

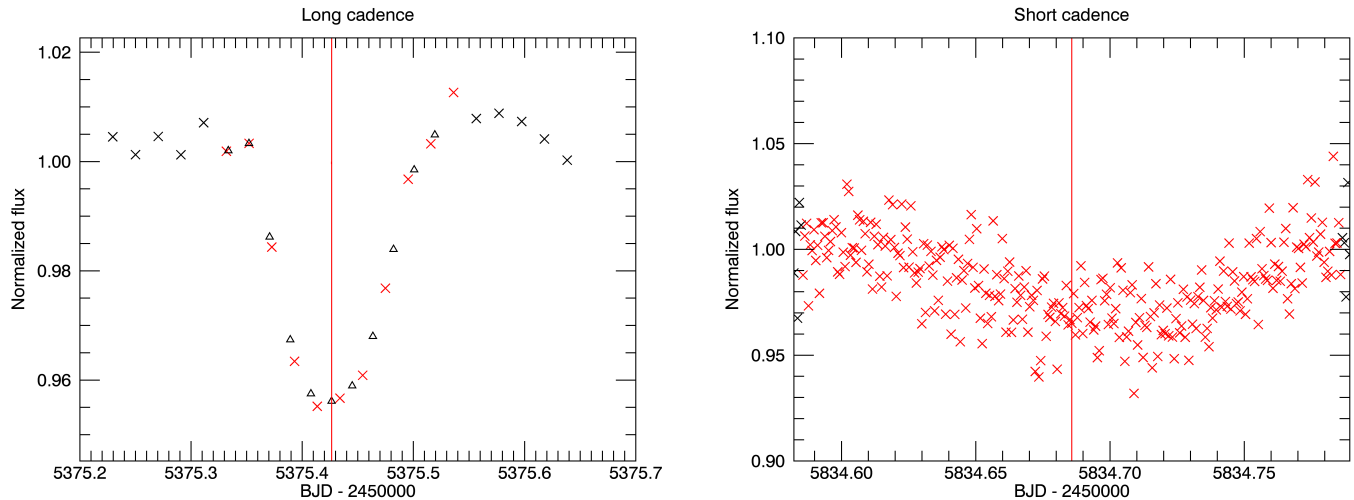


Figure 4.6 – The light curves for long and short cadence data. The crosses represents data points, where the red ones is used in the Kwee Van Woerden method. Triangles represents the interpolated data points used for the reflection of the light curve about the estimated time of minimum which is represented by the vertical red line. For the short cadence light curve, the estimated time of minimum is crucial for getting the correct value of the mid eclipse time, since s could be calculated for a local minimum.

cadence light curve will not be able to produce local minima because of the amount of data points are too low. For each of the light curves, the crosses represents data points, where the red crosses are the ones which are used in the Kwee Van Woerden method. The triangles represents the interpolated data points used for the reflection of light curve about the estimated time of minimum which is represented by the vertical red line. The triangles have been omitted for the short cadence light curve to avoid confusion. In order to bypass the issue with a possibility of finding a local minimum instead of the global minimum for s , we define an area around the estimated time of mid-eclipse where we reflect the light curve and calculate s values for each of these. It is still the same method but instead of letting the code search for a minimum of s , we construct a series of s values in order to find the global minimum. The search for the global minimum for the short cadence light curve can be seen in Figure 4.7 for the same light curve seen to the right in Figure 4.6.

The estimated time of mid-eclipse which was used in Figure 4.6 was 5834.6858 (BJD - 2450000) which when running the Kwee Van Woerden code gave a time of mid-eclipse of 5834.6958 (BJD - 2450000). As we can see in Figure 4.7 this cannot be right, and by making a sequence of s values we find the correct time of mid-eclipse to be 5834.7005 (BJD-2450000). The difference between these mid-eclipse times are 0.005 days which is very significant since the estimated unceratainties of each of these times are ± 0.0001

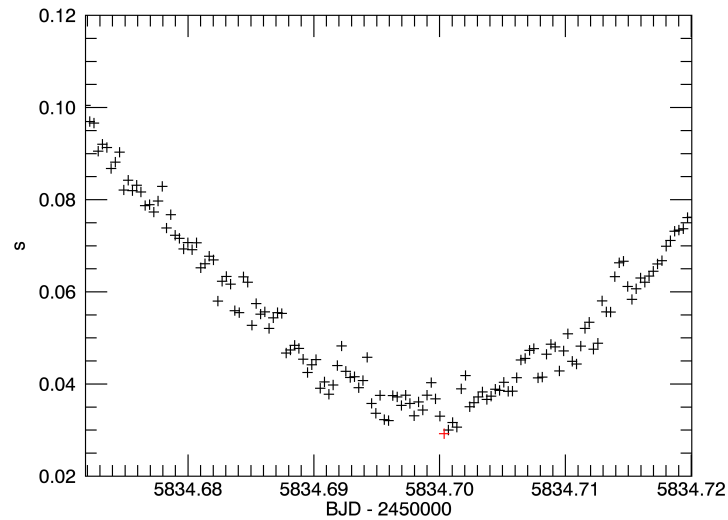


Figure 4.7 – By defining an area around the estimated time of mid-eclipse, we construct a sequence of values for s in order to find the time of global minimum which is marked with a red symbol. If this procedure is not done, the Kwee Van Woerden code would find the time of mid-eclipse to be 5834.6958, instead of the correct value of 5834.7005 (BJD -2450000).

days. For scenarios where we have estimated times of mid-eclipse from both short and long cadence light curves, we use the times obtained with the short cadence light curves, since their uncertainties are much lower than the once obtained for the long cadence data and a weighted mean of the two times would not make a significant difference.

4.2.2.2 V and R band data

From Brogaard et al. (2011) we have the V and R band data from two primary eclipses and two secondary eclipses in HJD which we converted to BJD. By using the Kwee Van Woerden method on these light curves we find that some of the mid-eclipse times do not correspond well with each other. In order to investigate this issue, Karsten Brogaard provided single pixel long cadence light curves from quarter 1 and 2 from the Kepler superstamp sample. The time series in quarter 1 and 2 corresponds with the time from when the R and V light curves were observed. By comparing the time of mid-eclipse from the Kwee Van Woerden method for the R , V and Kepler long cadence light curves we got information which we processed in the following way:

Primary eclipse (2454984.554 BJD)

Here the V and R mid-eclipse times showed variations of more than 2σ between each other. The long cadence supported the V band, where the mid-eclipse times agreed within 1σ . Because of this, we took a weighted mean over the V band and

long cadence mid-eclipses in order to compute an accurate estimate of the primary eclipse.

Primary eclipse (2454989.438 BJD)

In this scenario both the V and R mid-eclipse times corresponded well with each other, however the light curve which was used here did not cover the whole eclipse. In order to make sure that the imperfect light curve did indeed give the correct time of mid-eclipse, we compared it to the time obtained from the long cadence light curve. The difference between these times was more than 3σ ! In the light of this and because the long cadence light curve completely covered the eclipse we decided to use the time of mid-eclipse obtained from the long cadence light curve. The light curve of the V and R band can be seen in Figure 4.8.

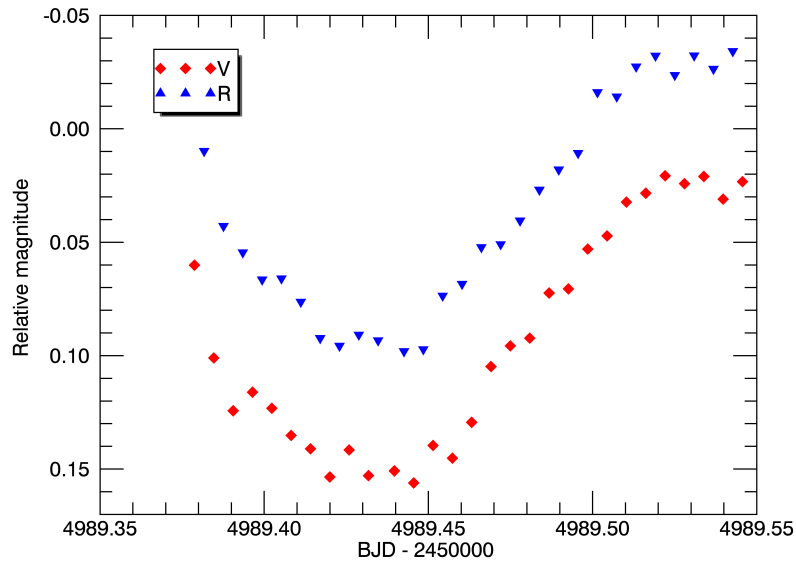


Figure 4.8 – Here the light curves of the primary eclipse (2454989.438 BJD) for the V and R band can be seen. The times of mid-eclipse correspond well with each other, but not with the one obtained from the long cadence light curve. Due to the fact that the light curves for either the V or R band do not cover the whole eclipse, we use the time obtained from the Kepler long cadence light curve.

Secondary eclipse (2455006.543 BJD)

Here the V and R band did not agree within 1σ . The Kepler long cadence light curve showed very good agreement with the V band and thus we used these two times to get an accurate estimate of the secondary eclipse.

Secondary eclipse (2455045.632 BJD)

For this eclipse, the V and R band agreed well with each other and it was in fact the long cadence light curve which showed some inconsistency, however it was still within 1σ of the two others. Because of this, we used all three times of mid-eclipse to compute a weighted mean for this secondary eclipse.

4.2.3 Period and ephemerides

By using the Kwee Van Woerden method we have estimated times of mid-eclipse and their corresponding uncertainties for 189 primary and secondary eclipses using the V , R , short- and long cadence light curves. We can now use these ephemerides for the primary and secondary eclipses to estimate the orbital period of V80 with very high accuracy. The following linear ephemerides for the primary and secondary eclipses of V80 are:

$$T_{\min}(\text{primary}) = 2454984.5539_{\pm 0.0002} + 4.885889_{\pm 0.000001} \cdot E \quad (4.1)$$

$$T_{\min}(\text{secondary}) = 2455006.5440_{\pm 0.0003} + 4.885871_{\pm 0.000002} \cdot E \quad (4.2)$$

where E is the number of cycles away from the first eclipse. As we can see, the orbital period of V80 obtained from both the primary and secondary eclipses agree well until we get to the last two digits. The uncertainty of the orbital period obtained from the primary and secondary eclipses are of the order 0.1 s and 0.2 s, respectively. The reason for the inconsistency between the last two digits of the orbital period is simply that we can not claim to know the period with such high accuracy. When the uncertainty gets below 1s, effects such as special and general relativity begins to play a role in our measurements. Furthermore considering the possibility of an underestimate of the uncertainties of the mid-eclipse times stated by Mikulášek et al. (2013), we adopt an uncertainty for the orbital period of 1 s which means that we find the orbital period of V80 to be 4.88589 ± 0.00001 days.

4.2.4 O-C diagram

In order to investigate if there exists periodic changes in the orbital period of V80 we construct O-C diagrams from the primary and secondary eclipses. The O-C diagrams are constructed by taking the observed times of mid-eclipse and subtracting the calculated times of mid-eclipse by using the linear ephemerides in Eq. 4.1 and 4.2. From the two O-C diagrams in Figure 4.9 there does not seem to be any systematic changes in the orbital period over the time interval of 1402 days which we have investigated. The uncertainty of each point have been removed for clarification, however the data agree very well with a normal distribution which one would expect for random errors. Notice the difference in the spread of the primary and secondary eclipses. This is simply because the depth of the primary eclipse is greater than the depth of the secondary which results in a much lower spread for the primary. By looking at the O-C diagrams of V80 we can conclude that there are not signs of a third body in the system which could affect the light curves of V80.

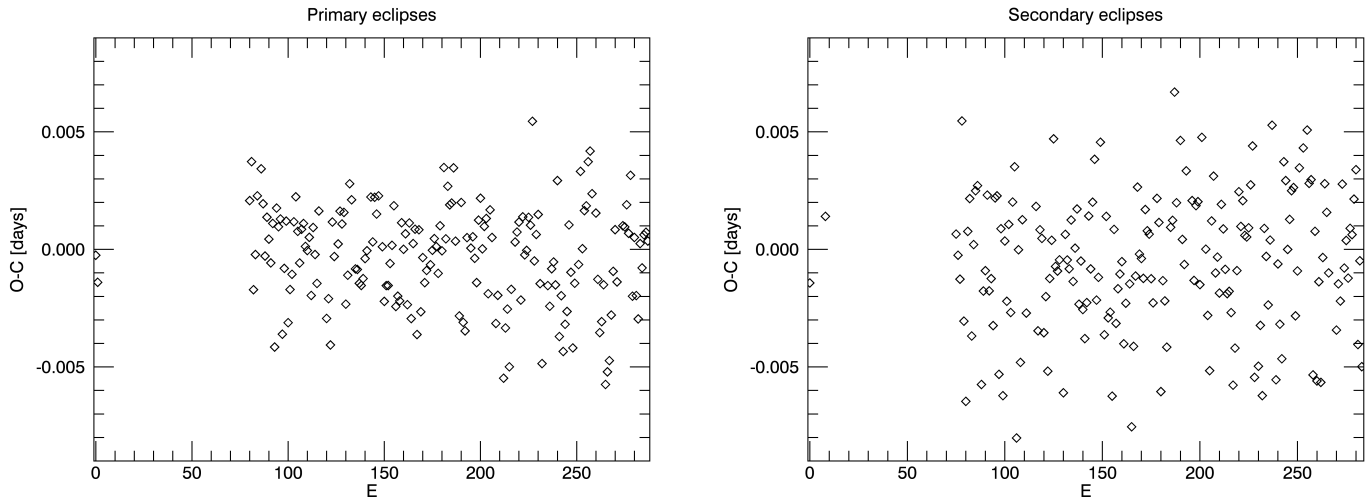


Figure 4.9 – The O-C diagrams for both the primary and secondary eclipses do not show any signs of periodic changes in the orbit of V80. Notice the difference in spread for the primary and secondary eclipses which is caused by a better precision in estimation of the time of mid-eclipse for the primary eclipse due to the difference in eclipsing depth.

4.3 Removal of the magnetic activity

If we want to investigate the photometric elements of V80, we first need to remove the parts of the Kepler light curve which we do not understand well enough to model in detail. This will be the light curve variations caused by the magnetic activity which appear to be somewhat periodic in the system. In order to remove the shape of the light curve which is caused by the magnetic activity, we first need to determine how it should be removed. By fitting a curve to the continuum of the light curve we can remove the shape by either dividing or subtracting the fit from the light curve. The magnetic activity is represented in the form of starspots which will be located either on the primary or secondary component, where we in Section 4.6 will present evidence and argue that the starspots must be located on the primary component.

By assuming that the starspots are located on the surface of the primary component of V80, we can argue for how we would expect the depth of the primary eclipse to vary. Since the main starspot period does not have the same period as the orbit of V80, the primary eclipse will occur at different phases of the main starspot period. This means that the depth of the eclipses will be different depending on the location of the starspots which are causing the light curve variations.

Scenario 1:

If the secondary star covers the surface of the primary star where the starspots

are located, then the depth of the primary eclipse will be different depending on where in the phase of the main starspot it is located. The correct procedure for removing the magnetic activity will then be to divide the light curve with the fit of the light curve continuum.

Scenario 2:

If the secondary star does not cover any area of the surface of the primary where the starspots are located, then the depth of the primary eclipse will be unaffected by where it lies in the phase of main starspot period. The correct procedure for removing the magnetic activity will in this case be to subtract the continuum of the light curve.

Before any of these two scenarios can be investigated we first need to make a fit to the light curve continuum. In order to do so, we first remove the primary and secondary eclipses of the long cadence light curves. Such a fit can be seen in Figure 4.10 where the vertical line represents the time of primary mid-eclipse and the red line is a least-square polynomial fit with weighted uncertainties. In the case of this light curve, a polynomial of 6th degree was found to be the best fit. Such a fit was done for 186 long cadence light curves covering one orbit.

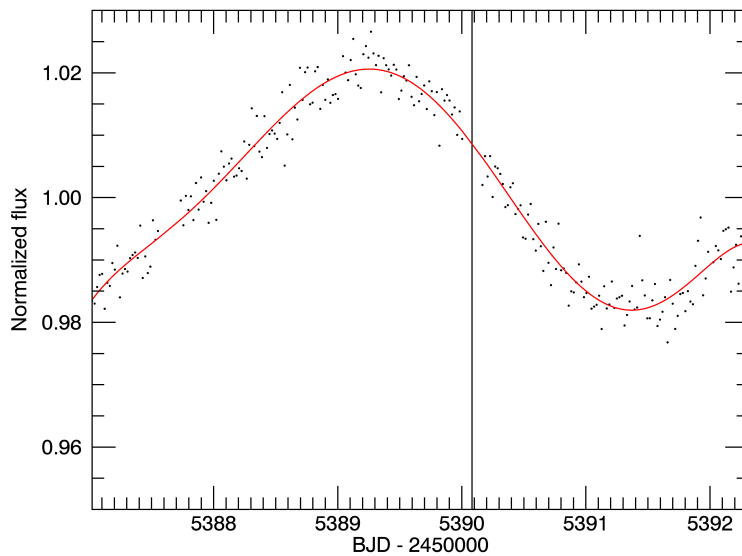


Figure 4.10 – The primary and secondary eclipses have been removed for the Kepler long cadence light curves in order to make a fit to the continuum of the light curves. The light curve in this figure has been fitted with a least-square polynomial fit of 6th degree which is seen as the red line. The vertical line represents the time of primary mid-eclipse.

For each of these fits we measure the vertical distance between the bottom of the polynomial fit to the location of the primary eclipse. This distance will be an estimator for

where in the phase of main starspot period the primary eclipse will be located. Because the shape of the continuum for each light curve changes, especially over different quarters, we divide the distance with the total vertical extent of the polynomial fit for each light curve. By doing so, we are able to relate the position for each primary eclipse in terms of relative distance from the minimum of the continuum fit.

As stated earlier, we do not fully understand the magnetic activity's impact on the light curve, and thus, our focus regarding the removal of the light curve will be around the primary and secondary eclipses. Analysing the light curve by removing the magnetic activity from the whole light curve would put constraints on the shape of the light curve. We do not have any evidence which suggests how the light curve should look outside of eclipses and therefore we will not use this part of the light curve when investigating the photometric elements of V80.

In the light of this, when removing the light variations caused by the magnetic activity from the light curve we will only fit around, but not during the primary and secondary eclipses. Again we use the light curves where the primary and secondary eclipses have been removed in order to fit to the continuum for the light curves. Just as before we use a least-square polynomial fit around the eclipses which can be seen in Figure 4.11. The left plot shows the points around the eclipse which has been used for producing the fit which is represented by the red line. The triangles in the plot to the right in Figure 4.11 represent the data points defining the eclipse which will be used in the light curve analysis.

The polynomial fit is then interpolated onto each of the triangles and are then subtracted and divided from the light curve. The result of this can be seen in Figure 4.12 where the red triangles and blue squares are the divided and subtracted light curve, respectively. It is hard to see, in the case of this primary eclipse, if there in fact is a difference between either dividing or subtracting the continuum fit from the Kepler long cadence light curve.

By measuring the depth of each primary eclipse for these two different ways of removing the magnetic activity we should be able to conclude whether it is scenario 1 or scenario 2 which is present in the light curve for V80. As we can see in Figure 4.13 there is very little difference in the measured depth of the primary eclipses as a function of position in the starspot pattern. There seems to be a tendency around phase 0 where the depths of the eclipses are lower than elsewhere. The spread in this area is however also greater which means that we cannot really correct for this tendency. It seems that there are different effects which alter the light curve of V80 and not only the magnetic activity. A big expected contributor to the altering of the light curve is the variation in the amount of light from additional objects in the aperture for V80. The field of view of the Kepler Space Telescope is very large and therefore the aperture for each target star can easily contain additional objects. This is not a big deal for bright stars, however the

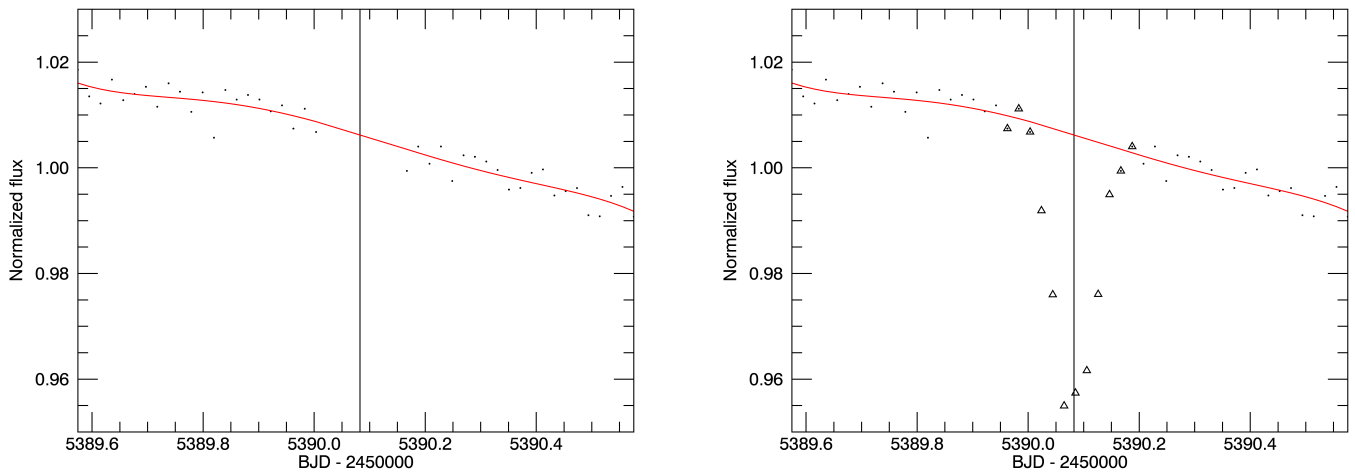


Figure 4.11 – The left plot shows the area around the eclipses where a least-square polynomial fit has been done. The triangles in the right plot represents the data points of the eclipse which will be used in the light curve analysis. The polynomial fit is then interpolated onto each of the triangles which then are subtracted and divided from the light curve.

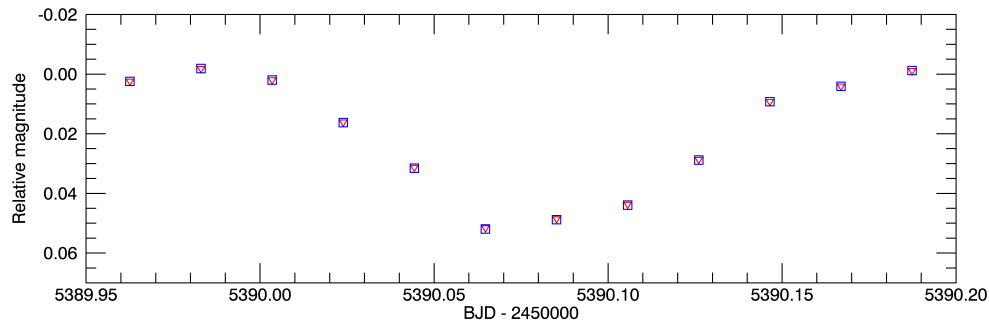


Figure 4.12 – The red triangles and blue squares are the divided and subtracted light curve, respectively. There does not seem to be any significant different between dividing or subtracting the continuum fit from the Kepler long cadence light curve.

apparent magnitude of V80 in the V band is $m_v \sim 17.886$, making it a faint object. Even more importantly, there are many stars close together since V80 is in a cluster which increases the possibility for additional objects in the aperature of V80. The smallest drift of the Kepler Spacecraft, which is not corrected for, can alter the light curve of V80. A combination of all these effect might be why we see a tendency around phase 0 in Figure 4.13. Our conclusion from Figure 4.13 is that it does not seem to matter how we remove the light variations caused by the magnetic activity at the level of accuracy

we can accomplish. The light curve variations are large and it seems likely that the secondary component would partly cover some of the starspots on the primary component and we therefore choose to use the divided Kepler light curve in our light curve analysis.

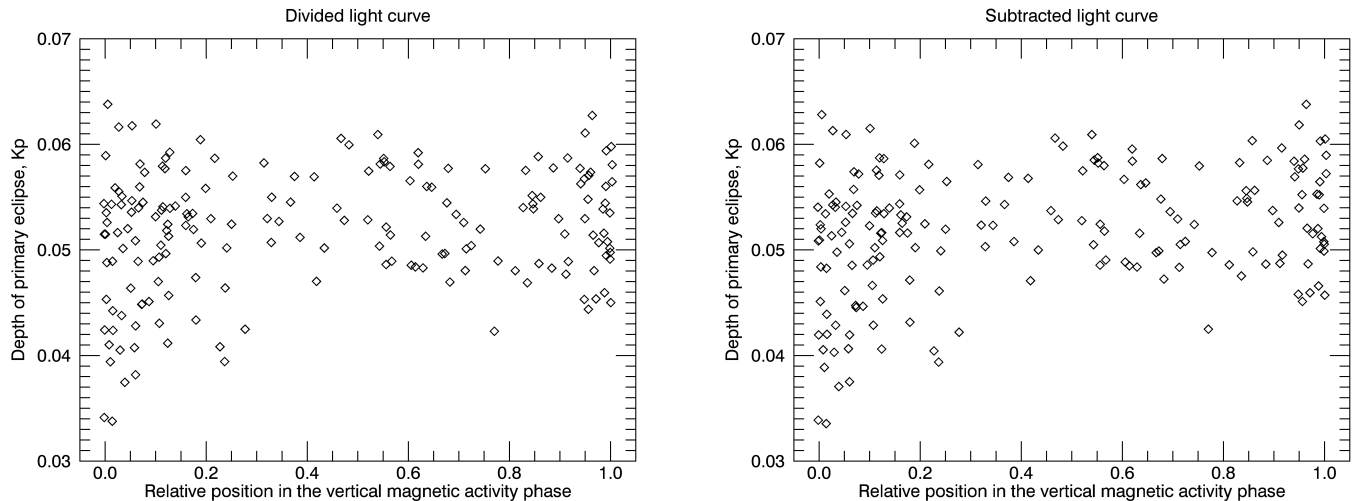


Figure 4.13 – Dividing or subtracting the magnetic activity continuum does not seem to make a difference regarding the depth of the primary eclipses. There however seems to be a tendency around phase 0 where the depths of the eclipses are lower than elsewhere.

4.4 Determining limb darkening coefficients for the components of V80

Before using the Kepler long and short cadence light curves in a light curve analysis we first need to determine the limb darkening coefficients $u_{1,2}$ for both the primary and secondary components of V80. In order to do so, we use the JKTLD⁴ code for computing theoretically calculated limb darkening coefficients. The coefficients of the JKTLD output is based on published tables of limb darkening coefficients calculated from stellar model atmospheres.

The inputs of JKTLD are the effective temperature of the star T_{eff} , the surface gravity $\log(g)$, the metallicity expressed by $[\text{Fe}/\text{H}]$ and the microturbulence velocity v_{micro} . The effective temperature of the secondary was not listed in Brogaard et al. (2011) and we therefore have to use a color-temperature-metallicity relation which we obtain from

⁴<http://www.astro.keele.ac.uk/jkt/codes/jktld.html>

Casagrande et al. (2010) which can be seen in Eq. 4.3

$$\theta_{\text{eff}} = a_0 + a_1 X_c + a_2 X_c^2 + a_3 [\text{Fe}/\text{H}] + a_4 [\text{Fe}/\text{H}] + a_5 [\text{Fe}/\text{H}]^2 \quad (4.3)$$

where $\theta_{\text{eff}} = 5040/T_{\text{eff}}$, X_c is the color and $a_i (i = 0, \dots, 5)$ are the coefficients which can be found in Table 4 in Casagrande et al. (2010) where the proposed standard deviation of the calibration $\sigma(T_{\text{eff}})$ is also given. By solving Eq. 4.3 with respect to X_c and using $[\text{Fe}/\text{H}]$ and the effective temperature of the primary component we find the color X_c which the primary component needs to have in order to give the observed effective temperature from the color-temperature-metallicity relation. We can calculate the color difference between the two components of $(B - V) = 0.897$ and $(B - V) = 1.200$ for the primary and secondary components, respectively. Then by using the measured $[\text{Fe}/\text{H}]$ for the secondary, we can calculate the effective temperature of the secondary component which is found to be 4864 ± 254 K.

The microturbulence velocity listed for the primary component in Brogaard et al. (2011) is $1.10 \pm 0.10 \text{ km s}^{-1}$, but most limb darkening coefficients in JKTL D are only available for a microturbulence velocity of 2.0 km s^{-1} . Because of this, we have to settle with a microturbulence velocity of 2.0 km s^{-1} for each component. For the Kepler band, there only exists limb darkening coefficients for three laws, namely, the linear law, the Sing three-parameter law and the quadratic law. The linear limb darkening law have shown to be a poor fit to both the observed limb darkening of the Sun and that predicted by theoretical model atmospheres, and we will therefore not use this law⁵. The Sing three-parameter law is not available for the V and R bands, and thus, for consistency we use the quadratic law for all three bands. The limb darkening effect I_u is described by the quadratic law in Eq. 4.4.

$$I_u = I_0 [1 - u_1(1 - \mu) - u_2(1 - \mu)^2] \quad (4.4)$$

Here $\mu = 1 - \cos(\gamma)$, where γ is the angle between a line normal to the stellar surface and the line of sight of the observer and I_0 is the surface brightness per unit area at the centre of the stellar disk. The input and output parameters of JKTL D is given in table 4.1 where we refer to the Kepler band as Kp .

⁵Brogaard et al. (2011), page 4.

Parameters	Primary	Secondary
Input:		
T_{eff} [K]	5600	4864
$\log(g)$ [cgs]	4.208	4.43
[Fe/H]	0.3	0.3
v_{micro} [km s ⁻¹]	2.0	2.0
Output:		
u_1 (R)	0.3824	0.5420
u_2 (R)	0.3039	0.1934
u_1 (V)	0.4976	0.6910
u_2 (V)	0.2572	0.1075
u_1 (Kp)	0.4483	0.5965
u_2 (Kp)	0.2304	0.1249

Table 4.1 – The input for JKTLD together with the limb darkening coefficients for the quadratic law for the Kepler, R and V band.

4.5 Preliminary light curve analysis

By using the R , V and Kp (Kepler band) light curves we want to perform preliminary light curve analysis in order to determine the quality of the data. R and V light curves were not good enough to put strong constraints on the photometric parameters of V80, however they might still be useful for comparison with the results for the Kepler long and short cadence light curves.

4.5.1 JKTEBOP code

The light curve model we use to analyse V80 is the Nelson-Davis model which represents the deformed stars as biaxial ellipsoids and applies a simple bolometric reflection model⁶. We use the JKTEBOP code by John Southworth which relies on the Nelson-Davis model and which is a revised and extension of the original EBOP code from Etzel (1981). Times of minimum, spectroscopic light ratios, third light values and orbital eccentricity can be included as observed quantities to constrain the solution. JKTEBOP offers Monte Carlo simulations to assign robust errors to the fitting parameters⁷.

4.5.2 Preliminary light curve analysis using V , R and Kp light curves

In our preliminary light curve analysis the period of V80 is well known and we therefore included it as a fixed parameter. From the spectroscopic orbit in Brogaard et al. (2011) the orbit of V80 was found to be circular and we therefore adopt a fixed eccentricity of $e = 0$. Just like Brogaard et al. (2011) we applied gravity darkening coefficients corresponding to convective atmospheres and kept the mass ratio $q = m_s/m_p$ fixed. The limb darkening coefficients were fixed since including them as free parameters resulted in unphysical values of these. Altering both the gravity and limb darkening coefficients had negligible effect on the derived photometric elements and because of this it was safe to keep them fixed during the light curve analysis.

By running the JKTEBOP code for a range of fixed values of $k = r_s/r_p$ we got results for each of the four different light curves which can be seen in Figure 4.14. The results from the R light curve model does not show any minimum in the root-mean-square (rms) of the fit for any value of k . The V light curve model shows a clear minimum at $k \sim 0.625$ which also seems to be the case for the Kepler long cadence light curve model. There is however not a clear minimum but rather a flat minimum in the interval $k = [0.60, 0.66]$ which means that the light curve model finds equal good fits for this range of k values. The Kepler short cadence light curve model shows a jump in the rms around $k \sim 0.61$ suggesting that some parameters in the model changes somewhat dramatically.

⁶Nelson and Davis (1972)

⁷<http://www.astro.keele.ac.uk/jkt/codes/jktebop.html>

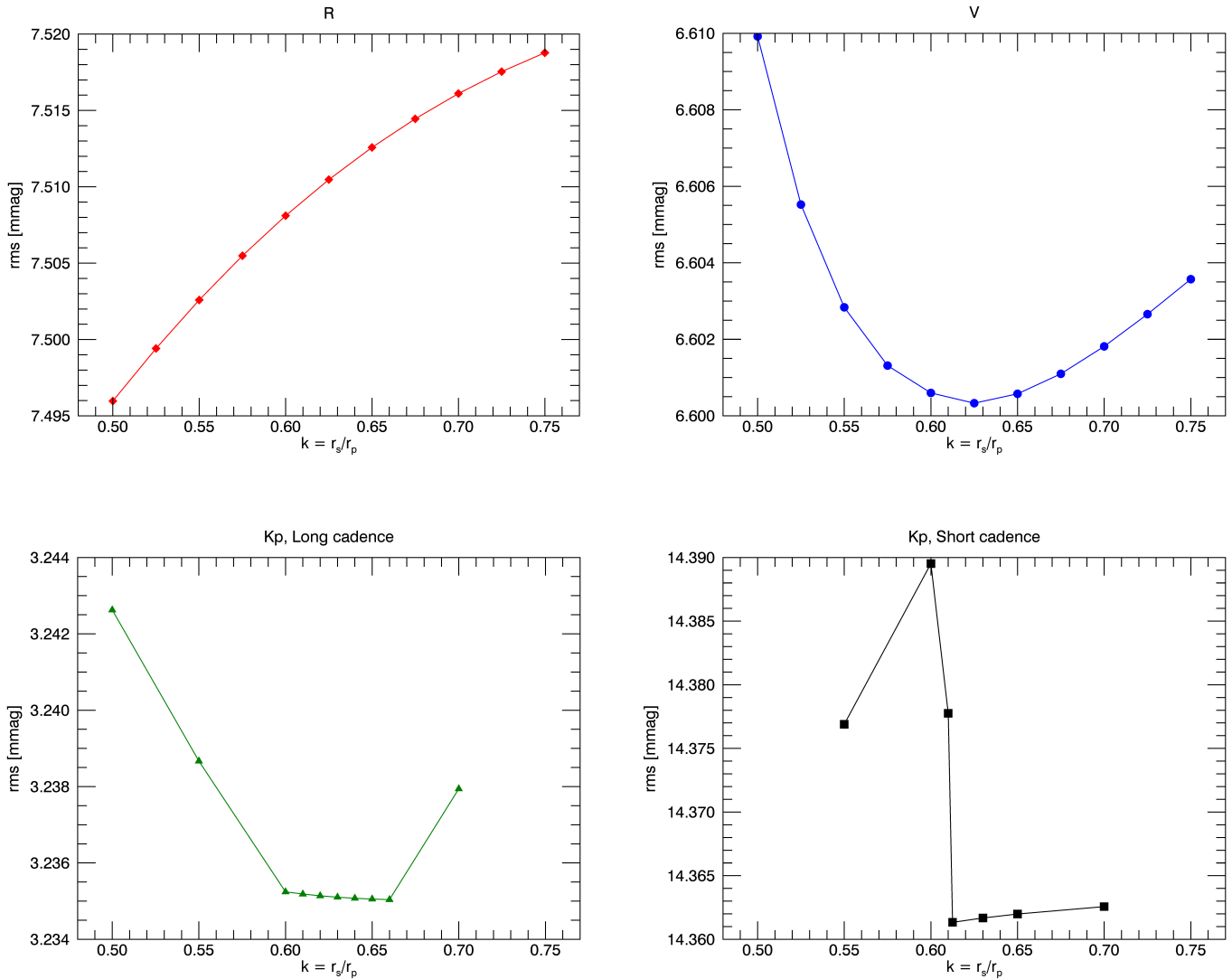


Figure 4.14 – The results for the preliminary light curve analysis of the four different light curves. The V band shows the most clear evidence for a preferred value of k , where the Kp long cadence light curve also shows indications of k being in the same range as the V band suggests. The R band light curve model does not show a minimum of rms for a specific value for k . The Kp short cadence light curve shows evidence of some kind of parameter change that affects the rms of the model at $k \sim 0.61$.

In order to investigate further we compared the estimated values of the orbital inclination which from Brogaard et al. (2011) was estimated to be $i = 84 \pm 1^\circ$. Even though the R light curve model did not show any preference for a specific value of k , it does however agree with V in regards to the orbital inclination as can be seen in Figure 4.15. The Kepler long cadence light curve model has an offset from the V and R light curve models of about 1° at $k = 0.63$ which is where we expect the true value of k lies if one is to trust the V light curve model in Figure 4.14. The Kepler short cadence light curve model is not included in Figure 4.15 due to its very bad fit, which is a consequence of the amount of third light in these light curves which is about 80% of the total light. The Kepler short cadence data covers 7 orbital periods while the Kepler long cadence data covers 189 orbital periods. The Kepler short cadence light curves were observed in quarter 11. If the amount of third light in this CCD from quarter 11 is around 80%, then it also might be for the rest of the quarters where the same CCD has been used to observe V80. The aperture mask is not exactly the same for each quarter due to the algorithm in the Kepler Telescope. Because of this, the quarters which are from the same CCD which observed quarter 11 might not have the same amount of third light in their light curve.

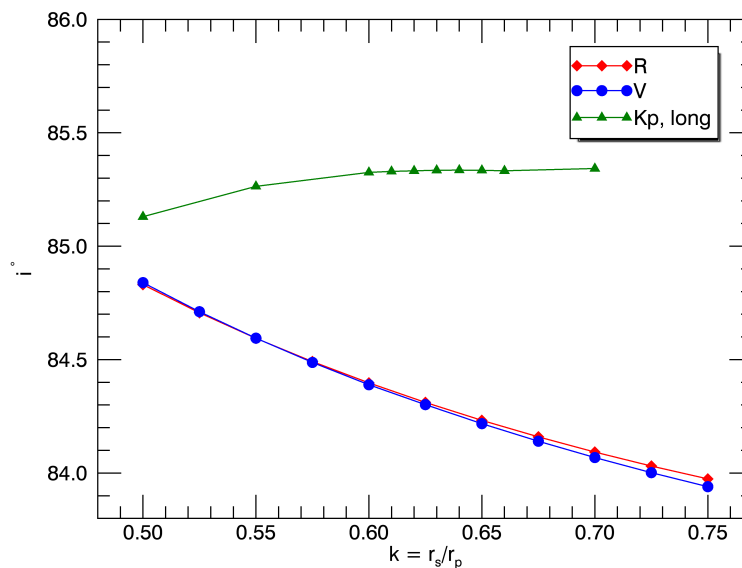


Figure 4.15 – Here the orbital inclination can be seen for the different values of k , where V and R correspond very well with each other. The Kp long cadence light curve shows a orbital inclination of about 85.3° which is about 1° higher than V and R at the expected value of $k = 0.63$ indicated by V in Figure 4.14.

4.5.3 Preliminary light curve analysis using Kepler long cadence light curves

Due to the amount of third light indicated by the Kepler short cadence light curve models, we want to further investigate the Kepler long cadence light curves by dividing the quarters into the four different CCDs which were used for observing V80. The amount of third light of 80% from the Kepler short cadence light curves indicates that the third light of the Kepler long cadence light curves of $\sim 68\%$ is driven up by the high amount of third light coming from the CCD which observed quarter 11. We therefore divide the quarters up into their respectable CCD which can be seen in Table 4.2.

	Quarter
CCD 0	8, 12, 16
CCD 1	9, 13
CCD 2	6, 10, 14
CCD 3	7, 11, 15

Table 4.2 – The quarters are dividing into each of the CCDs which was used for the observation of V80.

By performing a new preliminary light curves analysis of each light curve configuration for each CCD we get four new results. These results can be seen in Figure 4.16 where we can note that CCD 3 produces the worst rms fit which we also would expect if the third light is high in the aperture of CCD 3. CCD 3 does however also show a sign of a preferred fit around $k = 0.54$, together with CCD 0 with $k = 0.525$. These results are not consistent with the analysis of V which was not affected by a third light source. CCD 0 does show a relatively high jump in rms from $k = 0.525$ to $k = 0.50$ which might indicate that the light curve fit becomes much worse here and that it may therefore not be a real indication for a rms minimum of k . It seems very likely that the minimum around $k = 0.54$ for CCD 3 is caused by the high amount of third light. The light curves observed with CCD 1 and 2 show very little variation in the rms over the range of k values which indicates (just like the whole Kepler long cadence light curve model) that the light curve model does not prefer a specific value of k .

The orbital inclination and third light is represented in Figure 4.17 where we can see an expected strong correlation between these two components. As the amount of third light increases in the light curve, the depths of the primary and secondary eclipses will decrease, just like they would if the orbital inclination would decrease. Just as we expected, the amount of third light for CDD 3 is very high which means that the overall third light gets driven up in the Kepler long cadence light curve. The light curves observed with CCD 0 and 2 also show a high amount of third light in them, however their orbital inclination are within 1 and 1.5 σ of what was found in Brogaard et al. (2011). The result of CCD 1 is the one which matches the orbital inclination from Brogaard et al. (2011) the best. It does however only consists of two quarters, namely, quarter 9

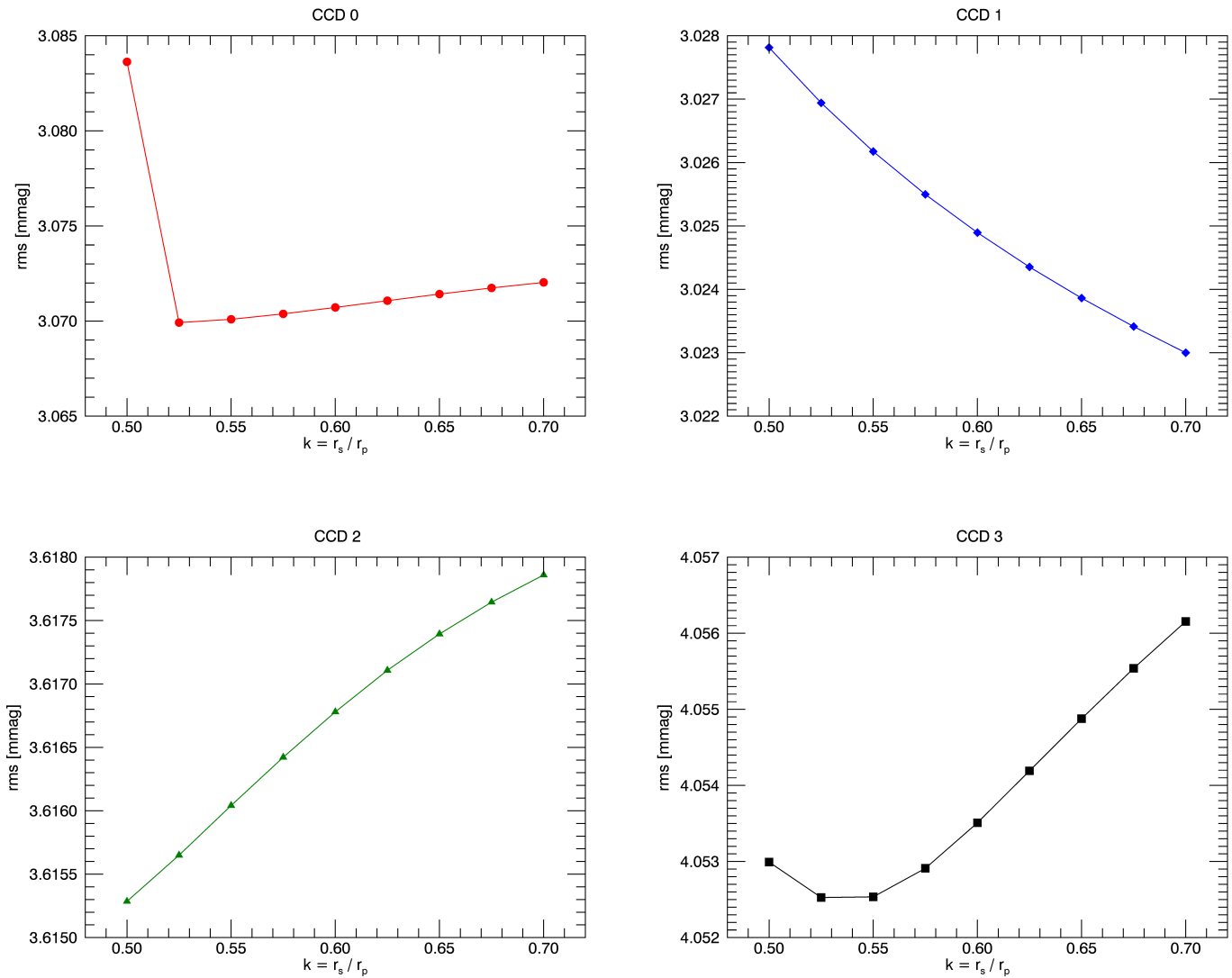


Figure 4.16 – The results for the preliminary light curve analysis of the four different CCDs for different values of fixed k .

and 13. If we only used the light curves from CCD 1 the uncertainty estimates for the photometric elements would presumably be less constrained due to the low number of data points used in the analysis. The consequence of this is that we decided to omit the light curves observed with CCD 3 and keep the ones observed with CCD 0, 1 and 2. In the following we will refer to the whole Kepler long cadence light curve as Kp^l , whereas we will refer to the light curve where CCD 3 has been omitted as Kp^* .

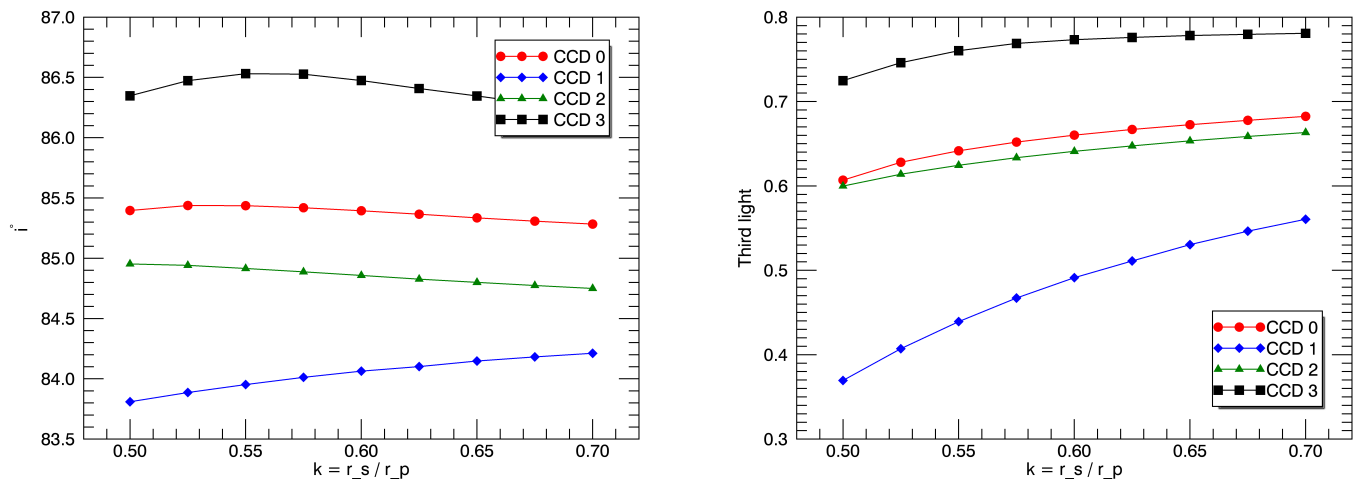


Figure 4.17 – The results for the preliminary light curve analysis of the four different CCDs for different values of fixed k .

With the CCD 3 light curves omitted we perform the same procedure for Kp^* as we did for Kp^l in order to see if the light curve model has been improved. By comparing Figure 4.14 and 4.18 we see that Kp^* indeed shows a better fit, with an improvement of ~ 0.23 mmag in the rms. Despite of this, there still does not seem to be any values of k which is preferred by the Kp^* since the rms values does not show any sign of a minimum. Further comparison with between Kp^l and Kp^* in Figure 4.19, but also the results for each CCD in Figure 4.17, show that the estimate of the orbital inclination decreases as the overall amount of third light in the light curves decrease.

The main goal of this preliminary light curve analysis was to see if we could find a preferred value of k which we could constrain the light curve fit with. Even by omitting the quarters observed with CCD 3 in Kp^* there still does not seem to be any preferable value for k in the light curve model. The light curve analysis from V shows a clearly preferred value of $k \sim 0.63$ which also is consistent with the flat interval in Kp^* . We do not feel comfortable enough to choose a value of k based solely of the results of V which only consists of two primary and secondary eclipses. Instead we use a different approach

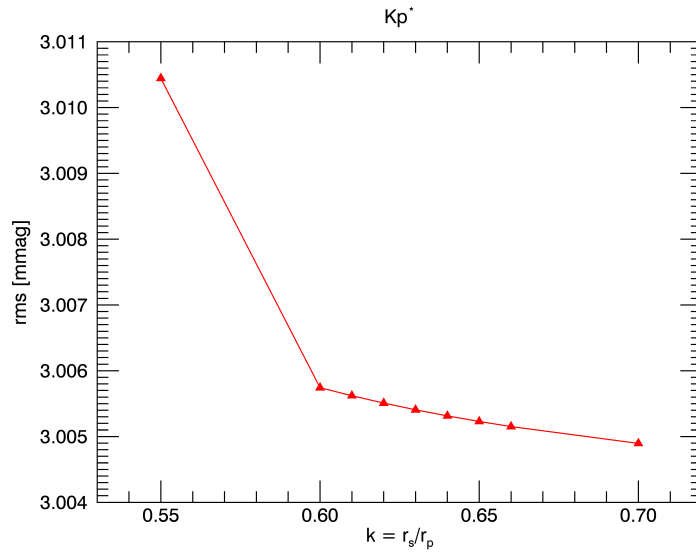


Figure 4.18 – Preliminary light curves solutions for the Kp^* light curve. The result is the same as in Figure 4.14 for the Kp^l light curve which also showed a flat bottom for the rms values of a different range of k .

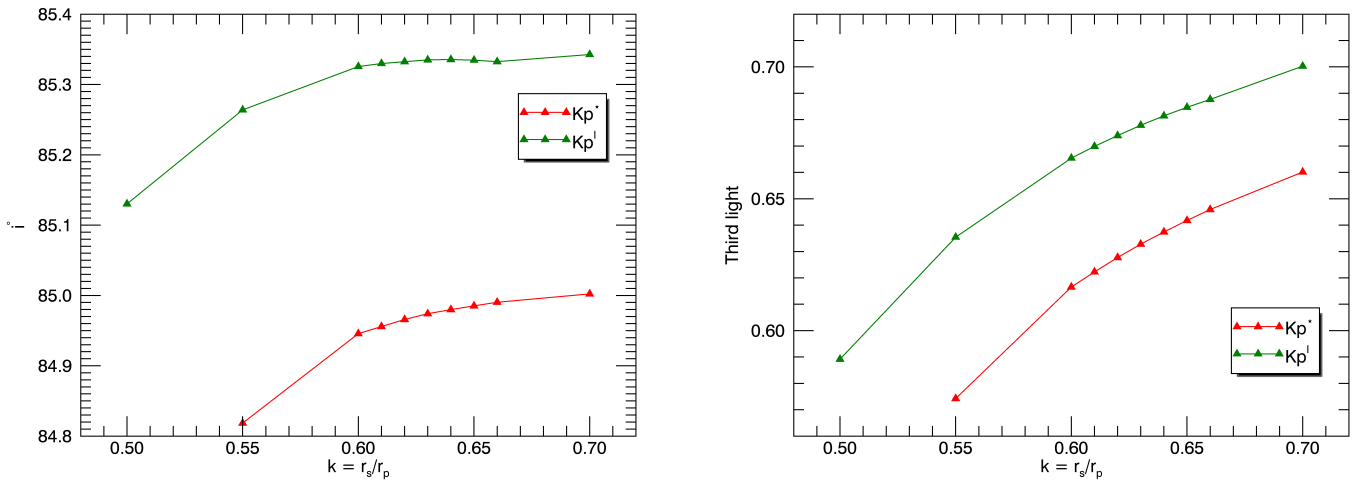


Figure 4.19 – The results for the preliminary light curve analysis of the four different CCDs.

which we will discuss in Section 4.7.

4.6 Analysing the magnetic activity of V80

V80 shows signs of magnetic activity in the form of brightness variations in V , R and Kp . We will in this section analyse the Kepler long cadence light curve and present evidence for different signatures which are associated with magnetic activity.

4.6.1 Stellar magnetic fields and starspots

A stellar magnetic field is generated by the motion of conductive plasma inside of the star. According to dynamo models, the motion is created by convection where the conductive plasma acts like a dynamo which generates a dipolar field. Fast rotation and differential rotation together with deep convective zones in the upper layers of a star will increase its magnetic activity. Localized magnetic fields can exert a force on a region of plasma which will cause it to rise relative to the surrounding plasma until it reaches the stellar surface. This will create a starspot which will be cooler than the stellar surface which will cause a decrease of flux in this region. If the distribution of starspots on a star is not uniform, the star will display brightness variations as it rotates about its own axis. Two magnetic active binary components have shown light curve variations with an amplitude as high as 0.6 mag in the V band. Large variations in color in these two systems have suggested the presence of cool spotted areas, which cover up to 20% of the entire stellar surface or about 40% of the stellar disk⁸. The temperature difference between starspots and stellar surfaces decreases from about 2000 K in G0 stars to 200 K in M4 stars⁹.

4.6.2 Preparing the Kepler long cadence light curve

To verify that these brightness variations are in fact due to starspots we will analyse the Kepler long cadence light curve. In the investigation of starspots we had the assistance of Heidi Korhonen from the Niels Bohr Institute who could help us verify the presence of starspots. Before Heidi Korhonen could analyse the light curve, we first had to divide the light curve into light curves for the primary and secondary components, respectively. The light curve variation caused by the main starspot period must be coming from one of the two components. By dividing the light curve up into two different light curves for the primary and secondary components we are able to see how much each of the stars have to vary in brightness, in order to produce what we observe in the light curve of V80. In order to divide the light curve up into two light curves, several steps are needed. The first step is to remove the amount of third light in the light curve. From Section 4.5 we found different estimates of the amount of third light for different quarters as seen in Figure 4.17. For each of the four CCDs, we run a light curve solution for a fixed value of k found from the best estimate in the V light curve of $k \sim 0.63$. We then use the estimated third light and light ratio $L = L_s/L_p$ found in these solutions to create the two light curves for the primary and secondary star where a section of them can be seen in

⁸Berdyugina (2005), page 8.

⁹Berdyugina (2005), page 26.

Figure 4.20. By looking at Figure 4.20 we can see that if the secondary is responsible for brightness variation in the light curve of V80, it has to have magnitude variations of ~ 1 mag, whereas the primary component only has to have magnitude variations of ~ 0.2 mag. A variation of magnitude of ~ 1 mag is very high for starspots and considering that the highest amplitude variations which has been observed is ~ 0.63 , it seems like the starspots are indeed located on the primary component.

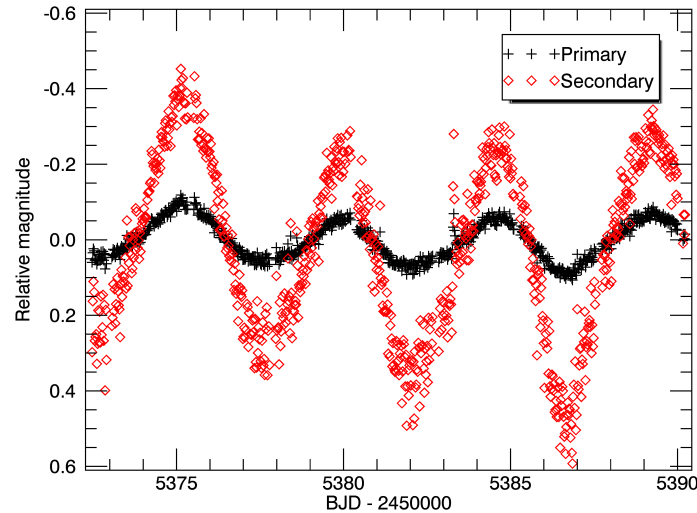


Figure 4.20 – The Kepler long cadence light curve where the primary and secondary eclipses and the third light has been removed. The light ratio $L = L_2/L_1$ from the preliminary light curve analysis has been used to make a light curves for the primary and secondary components of V80. If the magnetic activity in the form of starspots is coming from the secondary component it requires variations of ~ 1 mag in order to produce the brightness variations seen in V80 which seems highly unlikely.

4.6.3 Confirmation of starspots

By analysing the full light curve Heidi Korhonen confirmed our suspicion, that the brightness variations in the light curve is indeed caused by starspots. The patterns seen in the full light curve with changing amplitude is typical for magnetic activity and the amplitude change in the primary light curve of $\sim 0.1 - 0.3$ mag is normal for large starspots on magnetically active stars. Heidi Korhonen also pointed out that it is highly likely if not almost certain that the starspots are located on the primary component. Heidi Korhonen pointed out that due to its deep convective zones in its upper layers, the secondary component could easily be magnetically active and have starspots, however they would be hidden in the variations of the primary. The magnitude variations of the

primary can be seen in Figure 4.21 where we can see how the magnitude variations are quite different as time goes by which is common for starspots.

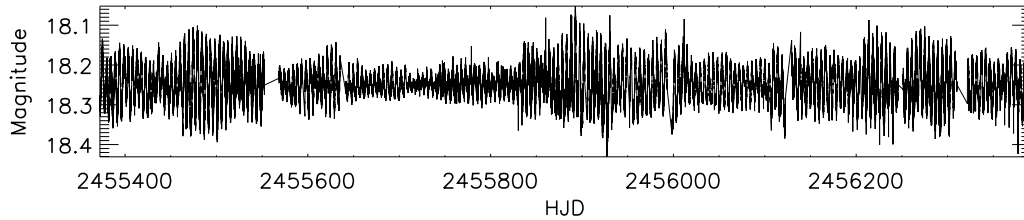


Figure 4.21 – Here the magnitude variations over the whole kepler light curve can be seen. The magnitude scale is arbitrary and does not matter, since it is the variations that are investigated. Credit: Heidi Korhonen.

Heidi Korhonen continued her analysis of the light curve with a period search with a Lomb Normalised periodogram. The periodogram showed that there is basically only one region in the periodgram that has a signal. This signal is around 4.7 days with a couple of distinct peaks around the main period of 4.74 days. This is a common indication that the star is rotating differentially. If the starspots are spread out on the stellar surface at different latitudes, the differential rotation of the star will change the starspot period and thereby cause what is seen in the periodogram. The periodogram can be seen in Figure 4.22 which is the same result we got in Section 4.1 where we found the main starspot period of 4.738 ± 0.008 days.

A more detailed investigation of the light curve was also carried out. Here the rotational phase was calculated using the main starspot period of 4.738 ± 0.008 days. 25 plots were constructed, each consisting of ~ 40 days of data, corresponding to ~ 8.5 stellar rotations. These plots can be seen in Figure 4.23 where the title of the plots are given in JD minus 2455000. All 25 plots show clear starspot evolution, often within the ~ 8.5 stellar rotation period. The light curve shape indicates that there are several starspots on the surface. Heidi Korhonen has thereby helped us confirm that the light curve variations are indeed caused by magnetic activity in the form of starspots which is most likely located on the primary component. Even so, the secondary could also be magnetically active with starspots, however this would be lost in the variations of the primary.

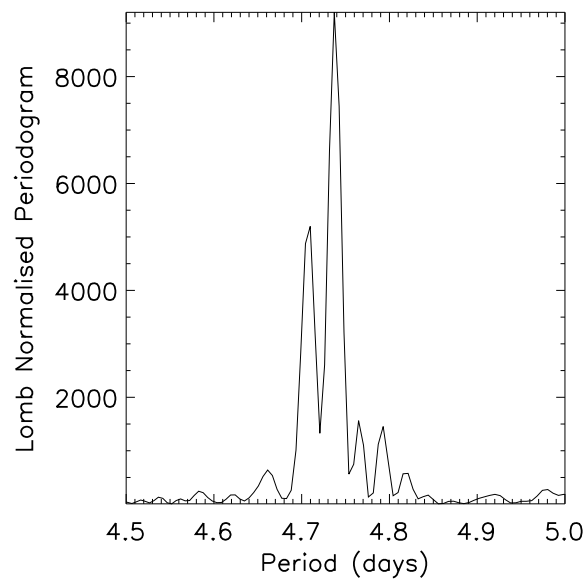


Figure 4.22 – The period search for the primary light curve where only one region has a signal. This is around the main period of 4.74 which we also found in Figure 4.3. The different periods are a common indication that the star is differentially rotating. Credit: Heidi Korhonen.

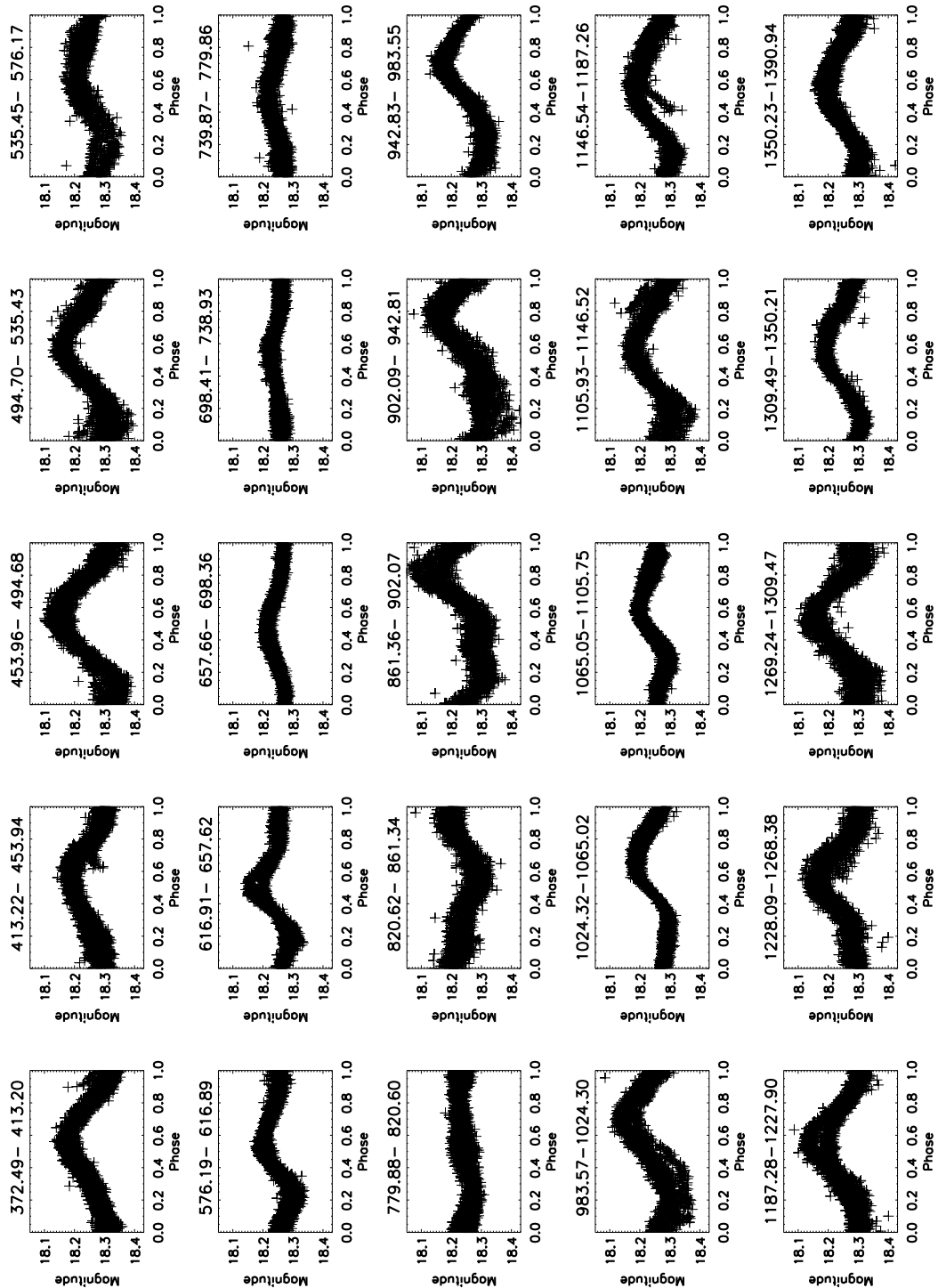


Figure 4.23 – The magnitude scale is arbitrary since it is only the variations we are looking for. The title of each plot are given in JD - 2455000. Each plot show starspot evolution even within the ~ 8.5 stellar rotation period. The light curve shape indicate that there are several starspots on the surface which are causing the observed light curve variations. Credit: Heidi Korhonen.

4.6.4 Observation of a superflare

Superflares are caused by the sudden release of magnetic energy stores near starspots where they release high amounts of energy on a timescale of hours. Maehara et al. (2012) have reported observations of 365 superflares for about 83 000 stars observed over 120 days from data obtained from the Kepler Space Telescope. The 365 superflares with energy of $> 10^{33}$ erg were found on 148 solar-type stars. It is suggested that superflares occur more frequently on rapidly rotating stars. Their amplitude are generally of the order of 0.1 – 1% of the stellar luminosity, however Maehara et al. (2012) also finds some superflares which have amplitudes of 8.4% of the stellar luminosity. We have

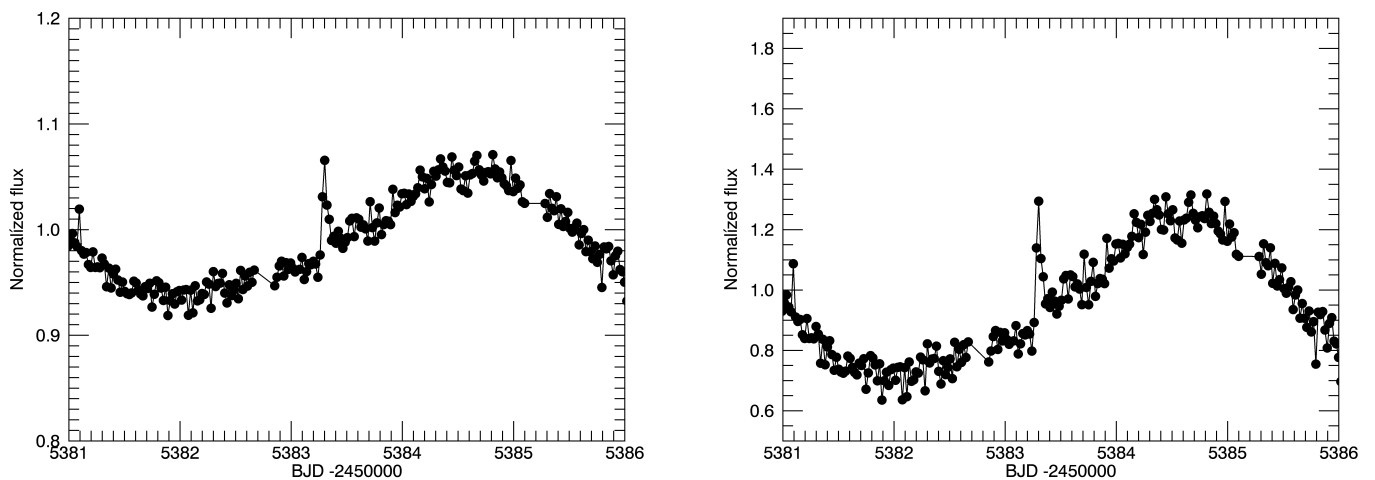


Figure 4.24 – The Kepler long cadence light curve where the primary and secondary eclipses and the third light has been removed. The light ratio $L = L_2/L_1$ from the preliminary light curve analysis has been used to make a light curves for the primary (left) and secondary (right) components of V80. The luminosity of the superflare is $\sim 10\%$ and $\sim 40\%$ of that of the primary and secondary, respectively.

identified a sign of a superflare in the Kepler light curve of V80. We use the two light curves which was used in Figure 4.20 to investigate the origin of the starspots. These two light curves showing the superflare can be seen in Figure 4.24. The luminosity of the superflare is $\sim 10\%$ and $\sim 40\%$ of that of the primary and secondary, respectively. Given our observations just as for the starspot origin it seems like the superflare is coming from the primary component, as a luminosity of ~ 40 of the secondary seems highly unlikely. We compare the shape of the observed superflare in the light curve of the primary component to light curves of typical superflares from Maehara et al. (2012) which can be seen Figure 4.25. As can be seen, the signature of the light curve of V80 agrees well with that from Maehara et al. (2012) which confirms that the superflare indeed seems to be originating from the primary component and has a duration of ~ 2.4

hours.

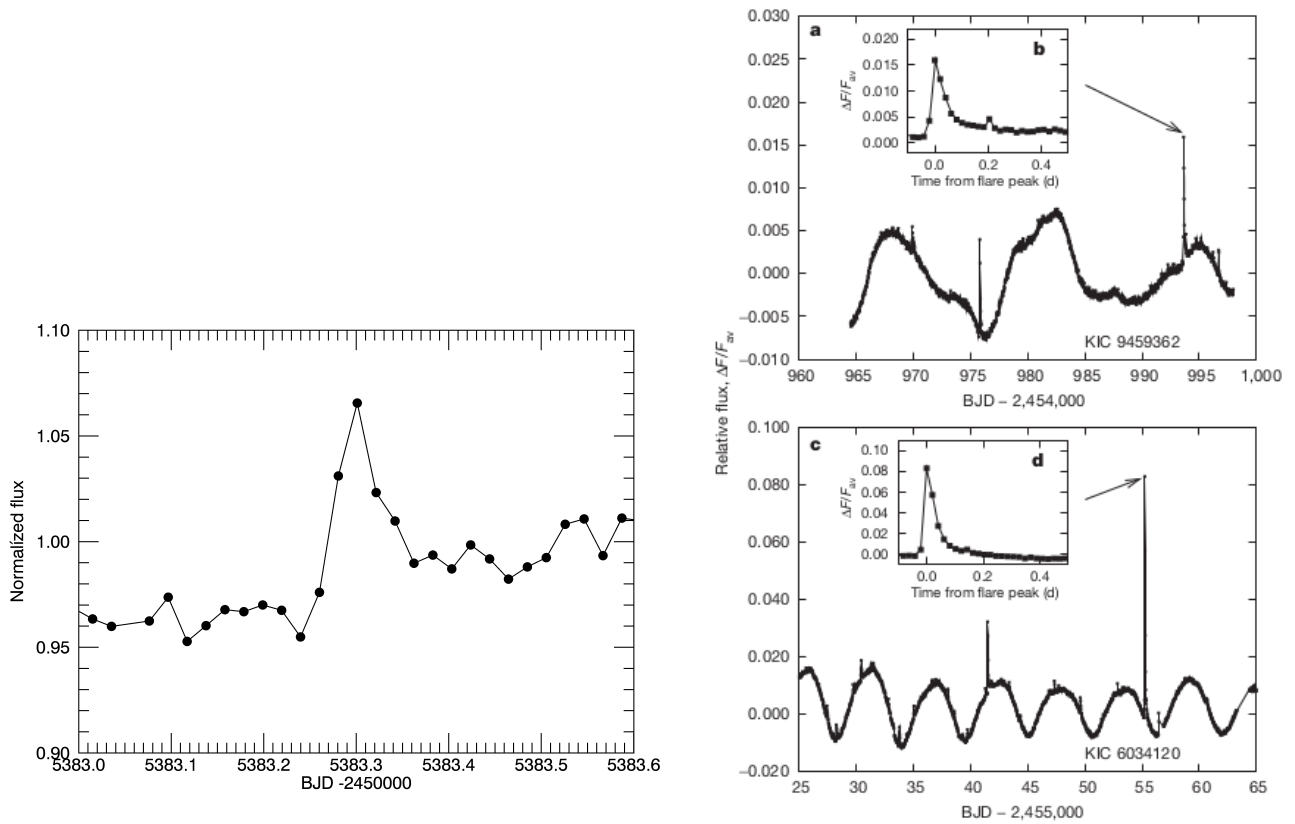


Figure 4.25 – *Left*: The light curve of the primary component where we have zoomed in on the superflare. *Right*: Typical light curves of superflares from Maehara et al. (2012).

4.6.5 Line emission

Emission of $H\alpha$ balmer lines is a strong indicator of high magnetic activity. Birkby et al. (2012) have reported $H\alpha$ emission in 3 out of 16 detached M-dwarf eclipsing binaries and argued that it was likely that it was caused by high magnetic activity in these systems. Other lines such as Ca II K (3968.5 Å) and Ca II H (3933.7 Å) can also be an indication of strong magnetic activity. By using periodic measurement of variations of the line emissions of Ca II K and Ca II H differential rotation together with rotation period can be determined¹⁰. V80 does not show any emission in $H\alpha$ for the primary component and unfortunately we have no observation of Ca II K or H line emission since the spectra from Brogaard et al. (2011) did not cover this wavelength range.

¹⁰Korhonen and Elstner (2011), page 120

4.6.6 X-ray emission and stellar rotation period

X-ray emission from magnetically active stars arises from hot gas in the corona which is the outermost part of the stellar atmosphere. Empirical observations suggest from papers such as Pizzolato et al. (2003) that there exists relations between X-ray luminosity and stellar rotation period. Van den Berg et al. (2013) have performed an X-ray study of NGC 6791 with the aim of uncovering the population of close interactive binaries with X-ray luminosities down to $L_X \sim 1 \cdot 10^{30} \text{ erg s}^{-1}$ (0.3 - 7 KeV). In their research they also observed V80 which showed emission of X-rays. The unabsorbed X-ray luminosity of V80 was found to be $L_{X,u} = 2.2 \cdot 10^{30} \text{ erg s}^{-1}$ or compared to the V band, $\log(F_X/F_V)_u = -2.5 \pm 0.2$. Since there exists a relation between X-ray luminosity and stellar rotation period we can compare the main starspot period of 4.738 ± 0.008 days and the X-ray luminosity of V80 with the empirical laws found in Pizzolato et al. (2003) for the mass ranges of the components of V80. These empirical laws can be seen in Figure 4.26. The masses of the primary and secondary components was found in Brogaard et al. (2011) to be $1.0588 \pm 0.0091 R_\odot$ and $0.8003 \pm 0.0062 R_\odot$, respectively. The horizontal line represents

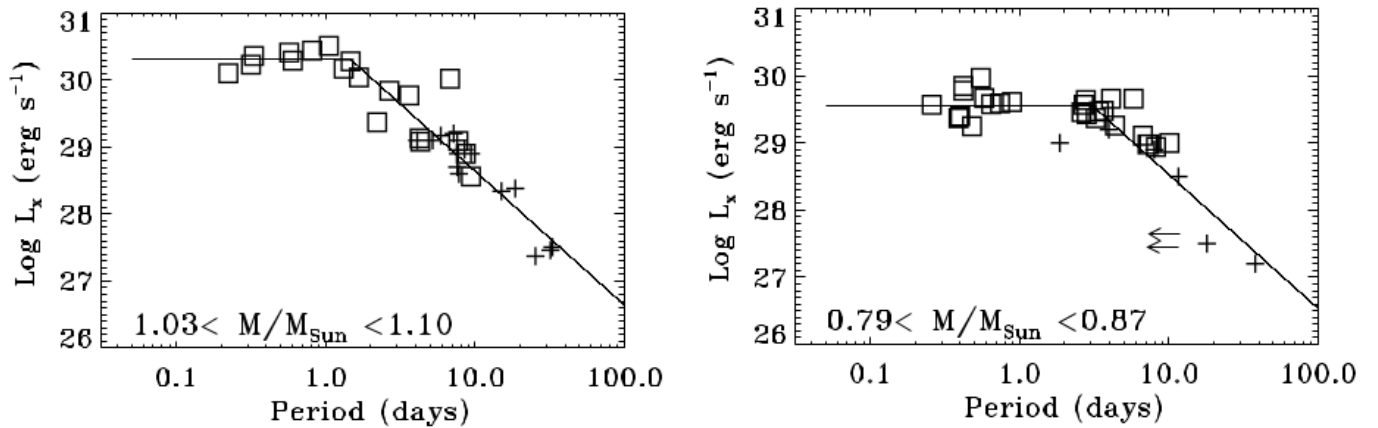


Figure 4.26 – *Left*: The relation between X-ray luminosity and stellar rotation period for the primary component of V80. *Right*: X-ray luminosity and stellar rotation period relation for the secondary component of V80. Squares represent cluster members, crosses represents field stars and left hand arrows indicate field dwarfs with periods derived from $v \sin(i)$ data. Credit: Pizzolato et al. (2003)

the level where the X-ray luminosity becomes saturated. The age of V80 is 8.3 ± 0.3 Gyr and we would therefore expect the rotation period of the primary and secondary to be synchronized with a period around the main starspot period of 4.738 ± 0.008 days. By looking at Figure 4.26 we can see that X-ray luminosity of V80 is much higher than was expected for the empirical law of the secondary component. It is however also higher for the empirical law of the primary component. Even if both components were magnetically active and followed the X-ray luminosity and period relation they would still be around a factor of 10 too low compared to the observed X-ray luminosity of

$L_{X,u} = 2.2 \cdot 10^{30} \text{ erg s}^{-1}$ in Van den Berg et al. (2013) which could indicate that both components of V80 are highly magnetically active.

4.7 Light curve analysis of Kp^*

The results of our preliminary light curve analysis showed that Kp^* was not good enough to constrain a value of k due to the amount of third light in the light curve. In order to be able to get further knowledge about V80 through the investigation of the Kp^* light curve we use the light ratio constrain in JKTEBOP and the mass-radius relation from the isochrone of the best age estimate of NGC 6791 found in Brogaard et al. (2012).

4.7.1 Light ratio in Kp^*

In Southworth et al. (2007) a new feature was incorporated in JKTEBOP where an externally determined light ratio could be applied in the light curve analysis. Since the light ratio in detached eclipsing binaries is highly correlated with k an observed spectroscopic light ratio can be used to constrain k . In Table 3.1 the light ratio was given to be $L = L_s/L_p = 0.15 \pm 0.05$ in V which can be used in our Kp^* light curve analysis, by rescaling the light ratio to the Kp band. In order to do so, we assumed that each of the stars were perfect black bodies and used Planck's law of black body radiation to calculate the flux of each star. We then used the V response function found at the NOT home page¹¹ and the Kp response function from the Kepler home page¹².

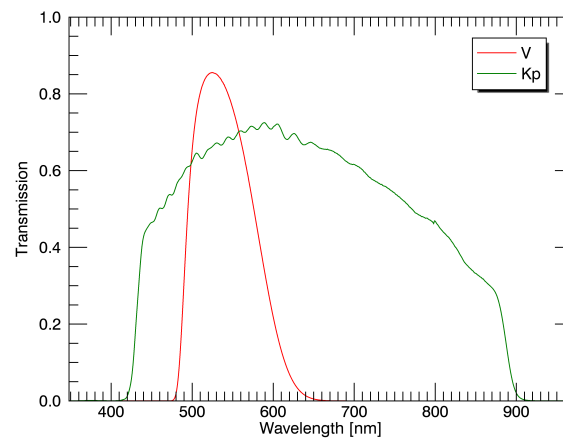


Figure 4.27 – A visualization of the Kepler and V band response functions used in the determination of the light ratio in the Kepler band.

¹¹<http://www.not.iac.es/instruments/filters/filters.php>

¹²http://keplerscience.arc.nasa.gov/kepler_response_hires1.txt.

The two response functions can be seen in Figure 4.27, showing how wide a wavelength range the kepler bandpass actually spans. When performing this transformation from V to Kp we do not take into account the effects of limb and gravity darkening since these effects are minor and will generally not change over such a short wavelength shift. Furthermore the uncertainty from the light ratio of the V band will be dominant which means that these minor effects can be ignored. We find the light ratio of the Kepler band to be $L = L_s/L_p = 0.267 \pm 0.102$.

4.7.2 Implementing the isochrone of NGC 6791

In order to get more insights on the light curve solution from the Kp^* light curve we want to employ the best matching isochrone of NGC 6791 found in Brogaard et al. (2012). Before we use the isochrone we will give a short description of what was done in Brogaard et al. (2012) in order to obtain this isochrone.

4.7.2.1 Brogaard et al. (2012)

Brogaard et al. (2011) investigated the binary systems V18, V20 and V80, where accurate masses and radii were determined for the components of V18 and V20. By using Mass-Radius diagrams (MR), Mass- T_{eff} diagrams (MT) and cluster member Color-Magnitude-Diagrams (CMD) Brogaard et al. (2011) performed stellar model comparison in order to constrain the age and helium content of the open cluster NGC 6791. Brogaard et al. (2012) is an extension of this investigation where conclusions of NGC 6791 are made by making detailed studies of stellar models and abundance pattern of these models. One of the best matching isochrones from Brogaard et al. (2012) which we will use in our light curve analysis was a an isochrone with an age of 8.3 Gyr, $[\text{Fe}/\text{H}] = 0.35$, $Y = 0.30$ and $E(B-V) = 0.14$ where a solar abundance pattern was used.

4.7.3 Using the isochrone from NGC 6791 as a constraint

By using the constraints from the light ratio and isochrone of NGC 6791 we perform light curve analysis using the JKTEBOP code. We performed two JKTEBOP runs of the Kp^* light curve. By assuming that one of the components will match the mass-radius relation from the isochrone we lock $r_{p,s}$ and include this as a fixed parameter in the JKTEBOP solutions. In order to find the values of $r_{p,s}$ we use the results of the masses of the components from Brogaard et al. (2011). Even though Brogaard et al. (2011) were not able to constrain the uncertainty of the orbital inclination to more than $\pm 1^\circ$, the masses of the components are still very precise with uncertainties for the primary and secondary of 0.85% and 0.77%, respectively. We can therefore be very certain of where on the isochrone in the Mass-Radius diagram the two components should lie on the mass axis.

In Section 4.6 we found evidence which suggest that the magnetic activity is primarily originating from the primary component. However, assuming that the X-ray luminosity

and stellar rotation period relation is indeed correct, the high X-ray luminosity of V80 could indicate that the secondary could also be highly magnetically active. Nevertheless, the primary component still seems to be much more active. The mass-radius relation we have from Brogaard et al. (2012) assumes that the components of the binary are none active which we know is definitely not true for the primary component. This means that by performing a light curve solution with a fixed r_p we constrain the primary component to not be magnetically active. Papers such as Birkby et al. (2012), Clausen et al. (2008), Clausen et al. (2009), Clausen et al. (2010) and Vos et al. (2012) have reported discrepancies between observations and stellar models for magnetically active binary components with a range of masses below $1.1M_{\odot}$. They show that stellar models predict $\sim 10\%$ smaller radii and $\sim 5\%$ higher temperatures than what is observed. We would therefore not expect our light curve solution with r_p fixed to give a realistic estimate of the photometric elements from V80 since the primary component is highly magnetically active. By fixing r_s in the light curve solution we expect a much more realistic estimate of the photometric elements of V80 since this would allow the radius of the primary component to show an increased radius which we would expect since this is one of the expected discrepancies of highly magnetically active stars. There is however also a possibility that the secondary could be magnetically active. We will therefore also include a photometric light curves solution where we have increased r_s with 10% which is the highest discrepancy we would expect for the secondary radius if it is also magnetically active.

For the two JKTEBOP solutions with r_p and r_s fixed, we applied 10 000 Monte Carlo simulations, whereas we applied 1 000 Monte Carlo simulations for $r_s + 10\%$. JKTEBOP assumes gaussian uncertainties and because of this, the large uncertainty in the light ratio L_s/L_p might not be sufficiently covered in the photometric analysis. In order to be certain that it does not affect the photometric results we run the light curve solutions for different ranges of L_s/L_p within the range of the uncertainties for the Kp light ratio. We find no significant differences in the photometric results and we therefore trust the photometric solutions when we use the light ratio constraint of $L_s/L_p = 0.267 \pm 0.102$. In order to run the Monte Carlo task in JKTEBOP we adopt rms values for each data point from the preliminary light curve solutions in Figure 4.18 of 3 mmag. The results of the three JKTEBOP solutions can be seen in Table 4.3, where l_3 is the amount of third light defined by $l_3 = L_3/(L_1 + L_2 + L_3)$.

As we can see in Table 4.3 each of the photometric solutions show an equally good light curve fit, despite the difference in the input parameters. This is expected since we showed in Section 4.5 that the light curve solutions did not show a rms minimum for the different ranges of k values. The three models can be seen in Figure 4.28 where there is no visible difference between the three different synthetic light curves.

Parameter	r_p (fixed)	r_s (fixed)	$r_s + 10\%$ (fixed)
Constraints			
L_s/L_p [Kp]	0.267 ± 0.102	0.267 ± 0.102	0.267 ± 0.102
i [$^\circ$]	84.31 ± 0.40	84.82 ± 0.48	84.62 ± 0.47
r_p	0.0863	0.0939 ± 0.0045	0.0910 ± 0.0046
r_s	0.0655 ± 0.0042	0.0511	0.05621
l_3	0.60 ± 0.04	0.58 ± 0.08	0.59 ± 0.07
Monte Carlo, N	10 000	10 000	1 000
Reduced χ^2	1.319 ± 0.024	1.320 ± 0.025	1.320 ± 0.025

Table 4.3 – Photometric solutions from the JKTEBOP code where r_p , r_s and $r_s + 10\%$ were adopted from the mass-radius relation of the ischrone of NGC 6791.

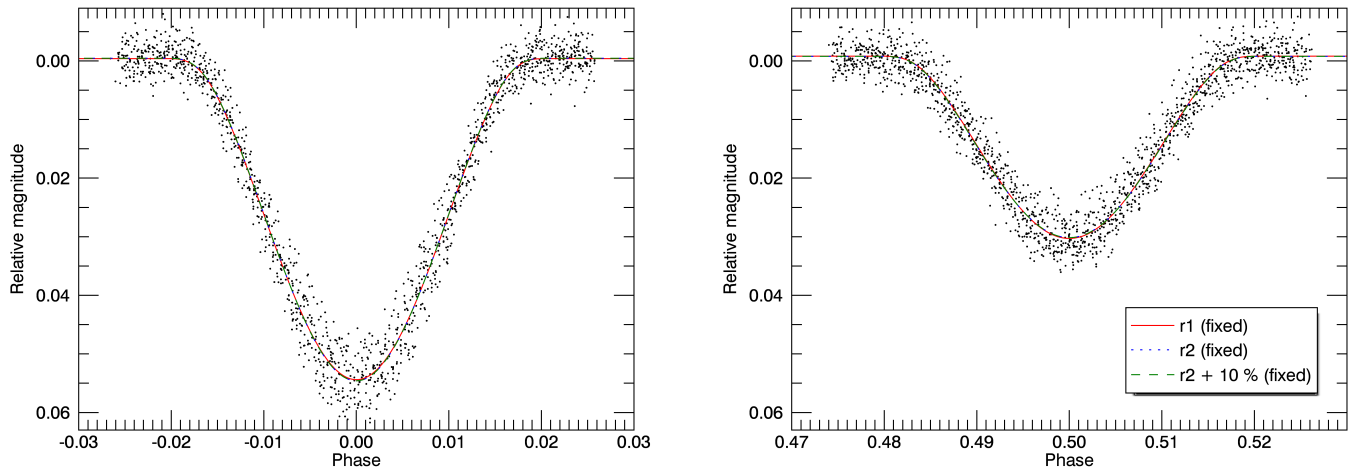


Figure 4.28 – The three different light curve solutions from JKTEBOP where phase 0 and 0.5 represents the primary and secondary eclipse, respectively. There are no visible difference between the three models.

5. Results and discussion

In this part of the thesis we will go through and discuss the different results obtained through the photometric analysis of the Kepler light curve. We will address the issues related to the estimates of stellar parameters of magnetically active binary systems where stellar models have been used to predict stellar parameters by decreasing the mixing-length-parameter of the magnetically active components.

5.1 Absolute dimensions

By using the photometric solutions from the JKTEBOP code and the spectroscopic orbital solution from Brogaard et al. (2011) we can calculate absolute dimensions for the components of V80. By comparing these results in the MR diagram together with the mass-radius relation from the isochrone of NGC 6791 we can deduce which of the photometric solutions are most probable. The absolute dimensions from the different photometric solutions can be seen in Table 5.1.

	r_p (fixed)	r_s (fixed)	$r_s + 10\%$ (fixed)
Absolute dimensions:			
M_p/M_\odot	1.0566 ± 0.0074	1.0539 ± 0.0075	1.0549 ± 0.0075
M_s/M_\odot	0.7987 ± 0.0048	0.7967 ± 0.0048	0.7974 ± 0.0049
R_p/R_\odot	1.2839	1.396 ± 0.067	1.354 ± 0.067
R_s/R_\odot	0.958 ± 0.063	0.7595	0.8358
	r_p (fixed) Secondary	r_s (fixed) Primary	$r_s + 10\%$ (fixed) Primary
$\log(g)$ [cgs]	4.377 ± 0.131	4.171 ± 0.096	4.197 ± 0.099
v_{sync} [km s ⁻¹]	9.93 ± 0.43	14.47 ± 0.69	14.03 ± 0.69
v_{rot} [km s ⁻¹]	(...)	14.1 ± 2.0	14.1 ± 2.0

Table 5.1 – Absolute dimensions obtained from our photometric solutions and the spectroscopic orbital solution from Brogaard et al. (2011). $\log(g)$ is calculated using the mass and radius. v_{rot} is obtained from Brogaard et al. (2011).

A comparison between the known mass-radius relation from the isochrone and the different results from the Kepler light curve analysis can be seen in Figure 5.1. The mass- T_{eff}

relation from the isochrone is also included together with the observed effective temperatures of the primary and secondary components. The MT diagram is included since we would expect to see a temperature discrepancy which is due to the magnetic activity of V80.

The light curve solution for fixed r_p gives an estimate of the radius of the secondary which is 26% higher than what the isochrone predicts. Even though the secondary could be highly magnetically active it would be unlikely that it would show such a high discrepancy in radius, especially when the magnetic activity in V80 seems to be originating from the primary component which we showed evidence for in Section 4.6. We would expect the primary to be the one which shows discrepancies and by fixing r_p in the light curve solution it is assumed that the primary component acts as a star with no magnetic activity, even though we have confirmation of it being highly magnetically active. By comparing the results from the magnetic analysis and the photometric solutions for fixed r_p it seems very unlikely that the photometric solution for r_p fixed gives a reliable view of the real photometric elements of the components of V80.

It is much more interesting to compare the two results from the photometric solution where we fixed r_s and $r_s + 10\%$ which can be seen in the top and bottom right in Figure 5.1. If we look in Table 5.1 the two results are quite similar. However, when we look at Figure 5.1 the small differences between these solutions proves to become highly relevant. The solution where r_s is fixed on the isochrone shows a value 10.5% greater than what the isochrone predicts for the primary and does not match the isochrone to within 1σ . Meanwhile the photometric solution for fixed $r_s + 10\%$ does match the isochrone just within 1σ . The solution for fixed $r_s + 10\%$ does still however show a radius 6.8% higher than the mass-radius relation of the isochrone. This is what we would expect according to the known discrepancies observed between observations of radius and stellar models, if the primary component is indeed magnetically active which our observation do suggest. If we believe that the radius of the secondary component is in the range $r_s < R_s < r_s + 10\%$, then the radius of the primary must lie in the range of $1.396 \pm 0.067 < R_p < 1.354 \pm 0.067$, and thus supporting the theory that the magnetic activity is causing the radius of the primary to be 6.8% - 10.5% larger than what stellar models predict.

Several papers such as, Clausen et al. (2009), Birkby et al. (2012) and Morales et al. (2010) have shown that stellar models predict $\sim 3 - 5\%$ higher temperatures than what is observed for magnetic active stars. Most of these discrepancies occur at masses in the range of $0.2 - 0.8M_\odot$, however some stars with masses of $\sim 1.1M_\odot$ have also shown discrepancies in temperature such as the primary component in the binary system V636 Centauri in Clausen et al. (2009). Here the $0.8M_\odot$ secondary is moderately magnetically active with starspots and Ca II H and K emission, where the $1.05M_\odot$ primary shows signs of magnetic activity as well, but at a much lower level. For the estimated age of the primary, the secondary component is 10% larger than model predictions. Both

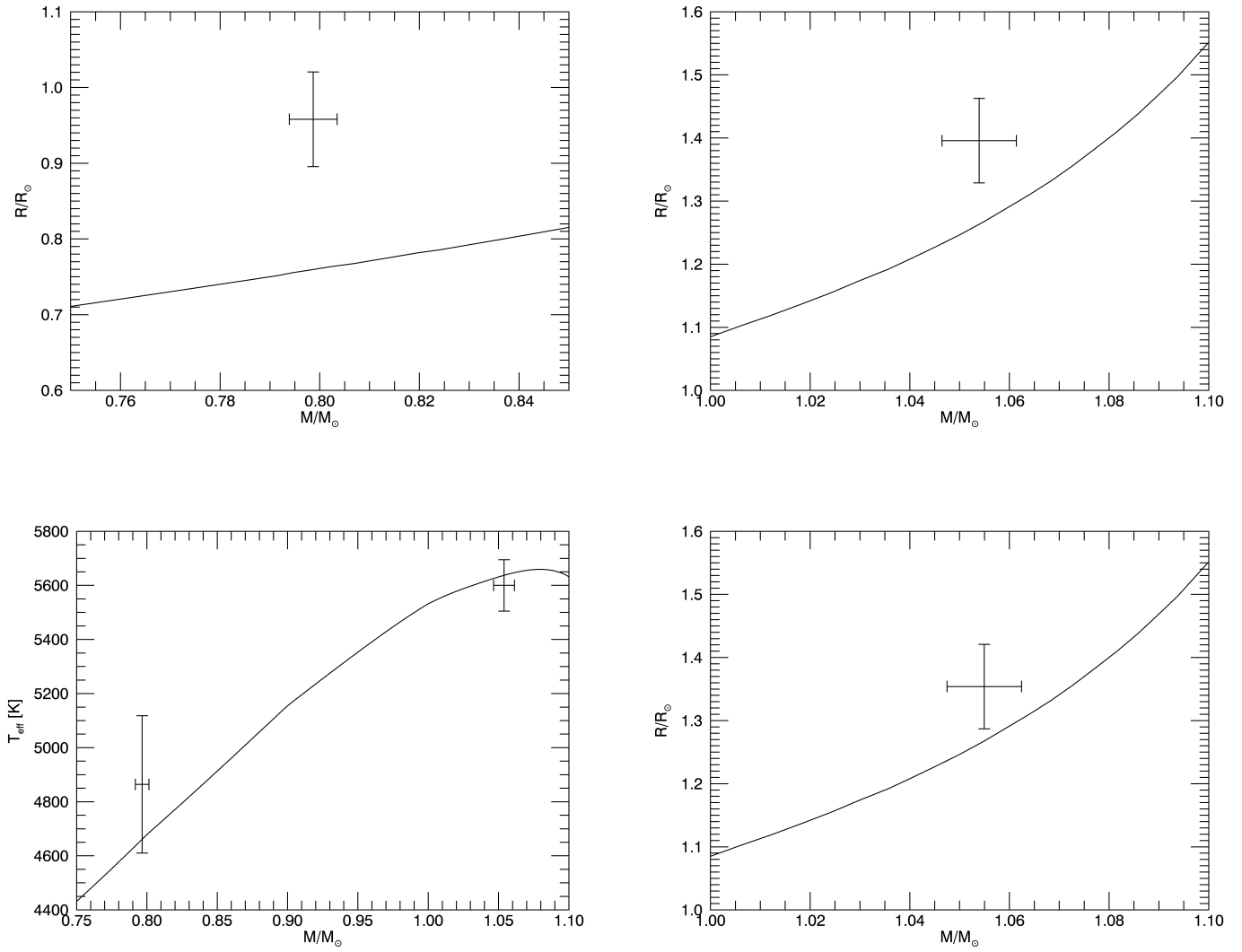


Figure 5.1 – MR diagrams constructed from the photometric JKTEBOP solutions combined with the spectroscopic orbital solution from Brogaard et al. (2011). *Top left:* fixed r_p . *Top right:* Fixed r_s . *Bottom left:* Mass-Temperature diagram of the primary and secondary components, *bottom right:* fixed $r_s + 10\%$. The uncertainties are represented by 1σ .

the primary and secondary show temperatures which are ~ 200 K and ~ 400 K cooler than predicted by stellar models, respectively. To investigate if this is also true for the components of V80, we compare the ischrone of NGC 6791 with the observed effective temperature of the primary from Brogaard et al. (2011) and the effective temperature of the secondary calculated in Section 4.4. This can be seen in the mass-temperature diagram in the bottom left of Figure 5.1 where the isochrone predicts temperatures 39 K higher and 203 K lower than what is observed for the primary and secondary, respectively. This corresponds to a temperature difference of 0.7% for the primary and 4.3% for the secondary. It does not look like the primary component share the same temperature discrepancy which is observed for other magnetically active stars which are in the same mass range. The secondary component of V80 which could also be magnetically active does also not show any sign of discrepancy in temperature. The secondary component is in fact hotter and not cooler, however it still matches the isochrone to within 1σ . The high uncertainty of the secondary component makes it hard to conclude anything from its possible observed discrepancy in temperature.

5.2 Radius estimation of the primary component

With confirmation that the light curve variations are caused by starspots which are highly likely to be located on the primary component of V80 we want to use the main starspot period to calculate its radius. From Brogaard et al. (2011) we have the projected rotational velocity of the primary component, $v_{\sin(i)} = 14.00 \pm 2.00$ km s $^{-1}$. If we assume that the main starspot period represents the starspots on the equator of the primary component we can calculate the radius of the primary component which is nearly independent of the light curve analysis. The dependence comes from the orbital inclination, however i shows a very small dependence of which light curve solution we pick as can be seen in Table 4.3.

V80	
Time scales:	
t_{sync} [Myr]	7.6860 ± 0.0005
t_{circ} [Gyr]	1.2348 ± 0.0009

Table 5.2 – The synchronisation and circularisation time scales for V80 calculated by using Eq. 2.47 and 2.48.

All i values are consistent with each other to within 1σ and also with the value found in Brogaard et al. (2011) of $i = 84 \pm 1^\circ$. We find the radius of the primary component by using the relation in Eq. 5.1.

$$v_{\text{rot}} = v \sin(i) = \frac{2\pi R}{P} \quad (5.1)$$

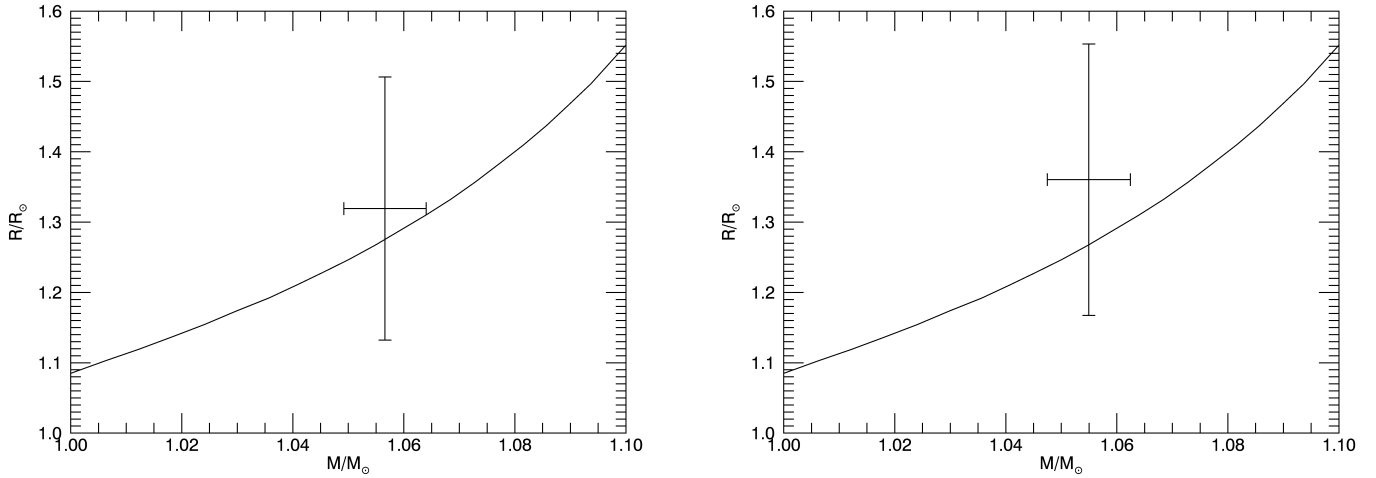


Figure 5.2 – *left*: radius of primary obtained using the main starspot period, *left*: radius of primary component assuming synchronisation rotation, using the orbital period. The rotational velocity used for both radius estimates are from the spectral analysis of the primary component in Brogaard et al. (2011).

When estimating the radius we assume that the starspots which is causing the primary signal in the light curve is located on the equator of the primary. Unfortunately we cannot be certain that this is the case, so the radius inferred from the main starspot period is in fact a minimum radius estimate of the primary component. The synchronisation and circularisation time scales for V80 can be seen in Table 5.2 where synchronisation is estimated to occur after 7.6860 ± 0.0005 Myr. Since NGC 6791 is estimated to be 8.3 ± 0.3 Gyr old, the components of V80 should be synchronised by now and thus if this is in fact true, the orbital period is equal to the rotation period of both the primary and secondary components. The periods and radii calculated using Eq. 5.1 can be seen in Table 5.3. The results of using different values of i for the photometric solutions does not have an effect in the calculated radius for the primary since the dominating uncertainty comes from the observed $v \sin(i)$. The observation of $v \sin(i)$ assumes solid body rotation and is not the observation of the equatorial velocity, however the high uncertainty seems to compensate for this assumption. The two estimates of the radius of the primary using the main starspot and orbital period can be seen in Figure 5.2 where they are compared to the mass-radius relation of the isochrone in the MR diagram. The estimate from the main starspot period and orbital period are seen to the left and right, respectively. The radii are 3.8% and 7.0% higher than what the isochrone of NGC 6791 predicts for the main starspot period and orbital period, respectively. If we compare the results in Figure 5.2 we can see that by applying the orbital period for the radius estimate does in fact increase the radius of the primary to an extent which levels the

	Starspot	Orbital
Parameter:		
Period [days]	4.738 ± 0.008	4.88589 ± 0.00001
R_p/R_\odot	1.32 ± 0.19	1.36 ± 0.19

Table 5.3 – Estimation of the radius of the primary component based on the main starspot period and the orbital period. The rotational velocity used for both radius estimates are from the spectral analysis of the primary component in Brogaard et al. (2011).

radius to that obtained in the photometric solutions were r_s was fixed. Even though the uncertainties in Figure 5.2 are high for the radius obtained for the main starspot period, it does however confirm that the starspots responsible for the light curve variations is indeed coming from the primary component.

By looking at Figure 4.22 which shows the periodic signals in the light curve, we can see that there are no significant signals above the orbital period of 4.88589 ± 0.00001 days. If the primary is indeed synchronized which the time scale suggests, then the starspots cannot be located at the equator, but must be located at higher latitudes. The fact that the starspots do not seem to be located on the equator of the primary component implies that the primary component does rotate slower at its equator than at higher latitudes which means that the primary component seems to be experiencing anti-solar differential rotation.

5.3 Magnetically active detached binaries

When estimating the radii of the components of V80 we are so fortunate that Brogaard et al. (2012) have analysed the age and stellar parameter for NGC 6791 to very high precision. This was done by using CMD of NGC 6791 and two detached binary systems (V18 and V20) which did not show any signs of being magnetically active. Because of this, the isochrone was very tightly constrained in regards to stellar parameters. This means that we know what the radius-mass relation is expected to be if the components of V80 were not magnetically active. We have therefore been able to compare our observations to this mass-radius relation and have thereby been able to measure and investigate the known discrepancies which are associated with magnetic activity in a way which has never been done before. If a magnetically active binary is a field star or if the cluster it resides in has not yet been investigated, the stellar parameters cannot be known and the mass-radius relation is therefore unknown. The fact that one or both of the components are magnetically active makes the investigation of the correct stellar model very hard if not impossible. Examples of where a stellar model has been determined even though the binary is magnetically active are Clausen et al. (2009), Clausen et al. (2008) and Vos et al. (2012). We will briefly go through each of these and in Section 5.3.4 address their methods and conclude on them.

5.3.1 Clausen et al. (2008)

In Clausen et al. (2008) the detached binary system EW Ori was investigated where the secondary shows signs of magnetic activity where it reveals weak lines of Ca II H and K emissions. The best age estimate is found at the age of 2.3 Gyr for the system. In order to get this perfect agreement, a slight downwards adjustment of the mixing-length-parameter was done for the secondary and a slightly lower amount of helium content was adopted.

5.3.2 Clausen et al. (2009)

The procedure of Clausen et al. (2009) was mentioned earlier where both components are magnetically active. In order to get the best stellar model to match the mixing-length-parameter was lowered to 1.4 for the primary and 1.0 for the secondary to obtain the best age estimate of 1.35 Gyr for the system. The observed $[\text{Fe}/\text{H}]$ was estimated to be -0.20 ± 0.08 , however in the best fitting stellar model $[\text{Fe}/\text{H}]$ was fixed without taking its uncertainty into account.

5.3.3 Vos et al. (2012)

Vos et al. (2012) investigated the detached binary system EF Aquarii where the secondary shows signs of high magnetic activity in the form of starspots and strong Ca II H and K emission lines. The primary component does also show signs of being magnetically active but at a much lower level. Like in Clausen et al. (2009) the observed $[\text{Fe}/\text{H}] = 0.00 \pm 0.10$ is fixed to the observed value and the best age estimate is found by lowering the mixing-length-parameter to $\alpha_{\text{MLT}} = 1.30$ for the primary and $\alpha_{\text{MLT}} = 1.05$ for the secondary, giving both components the common age of 1.5 ± 0.6 Gyr.

5.3.4 Article discussion

As we can see from the Clausen et al. (2008), Clausen et al. (2010) and Vos et al. (2012) a common way to correct for the discrepancies between observation and stellar models in binaries, is to decrease the mixing length parameter for the magnetically active components. The justification for doing this, is that the magnetic activity is believed to decrease the effectiveness of the energy transport for convection and thereby cause the star's radius to increase and its surface temperature to cool. There is in principle nothing wrong with decreasing α_{MLT} in order to account for magnetic activity in a star if the other parameters are well known. However, since parameters such as age, helium abundance and $[\text{Fe}/\text{H}]$ are not known to very high precision in the mentioned papers, the uncertainties of age, helium abundance and $[\text{Fe}/\text{H}]$ will be incorporated into α_{MLT} . In other words, it is assumed that the discrepancies between observation and models can be described solely by decreasing α_{MLT} . This does not seem likely and doing so means that the age of the stellar model isochrone is not necessarily a good estimator of the true

age of the binary system.

In Clausen et al. (2008) where the secondary is the only component observed to be magnetically active, the primary is fixed on a isochrone which best matches the primary component with a fixed observed $[\text{Fe}/\text{H}]$, disregarding the uncertainties of $[\text{Fe}/\text{H}]$. α_{MLT} is then decreased for the secondary until it matches the isochrone of the primary component. It seems like that there would be many isochrones which would match the primary component within 1σ and how is the best isochrone then selected? Using 1σ as a threshold when comparing models seems necessarily, at least for radius-temperature and mass-temperature diagrams since there is a relative high uncertainty in temperature, but not for MR diagrams. Statistically the chance for one component matching the isochrone to within 1σ is $\sim 68\%$. When decreasing α_{MLT} for the secondary in order to get the best match for both components the chance for both the primary and secondary to agree to within 1σ is $\sim 46\%$. The situation gets even worse in Clausen et al. (2009) and Vos et al. (2012) where both components are magnetic active and α_{MLT} needs to be decreased to different values for the primary and secondary.

Obtaining the right age estimates of magnetically active detached binaries seems to be very dependent on the chosen values of the mixing-length-parameter α_{MLT} which is used to match the binary components to the same isochrone. In order to match the components correctly, the stellar parameters need to be known to very high precision like in the case of NGC 6791.

5.4 Anti-solar differential rotation

There does not exist any observations of stars where anti-solar differential rotation has firmly been confirmed even though some papers claim to have indications which suggest the observation of this. In this section we want to address some of the papers which have claimed to have detected stars which experience anti-solar differential rotating.

5.4.1 Reports of stars indicating anti-solar differential rotation

There are several papers which claim to have observed anti-solar differential rotation such as Strassmeier et al. (2003), Weber et al. (2005), Kóovári et al. (2007), Weber (2007), Hackman et al. (2001) and Vogt et al. (1999) where Doppler imaging has been applied. Doppler imaging can be used to map starspots on rapidly rotating late-type stars by studying the line profiles of high resolution spectra. Starspots on the surface of a rapidly rotating star will cause distortions in the observed spectral line profiles indicated by "bumps". As the star rotates these bumps will move across the absorption line profiles and by tracing these distortions a surface map of the star can be made. Including photometric measurements of the light curve of the star can constrain the temperature range of model atmospheres and thereby be used to calculate a surface temperature distribution of the star. In order to trace differential rotation, two surface

images are indeed which should be separated by a time interval high enough so the starspots would have had time to move on the stellar surface, but not so much that the short-lived starspots disappear. By cross-correlating constant latitude slices of the two images and then calculating the shift as a function of the latitude can give a description of the differential rotation. This has been done in all of the mentioned papers, except for Hackman et al. (2001).

5.4.2 Strassmeier et al. (2003)

Of the papers where cross-correlation has been used, the best evidence of the observation of anti-solar differential rotation are presented in Strassmeier et al. (2003). Strassmeier et al. (2003) investigated the rapidly rotating single K2 giant HD 31993 where Doppler images from two consecutive stellar rotations was used. The cross-correlation function in Strassmeier et al. (2003) from the two independent consecutive Doppler images can be seen in Figure 5.3 where the dots represents the cross-correlation peaks in each latitude strip. The grey scale represents the correlation coefficient where black is perfect correlation and white is no correlation. The vertical line is the rotational period of 25.3 days.

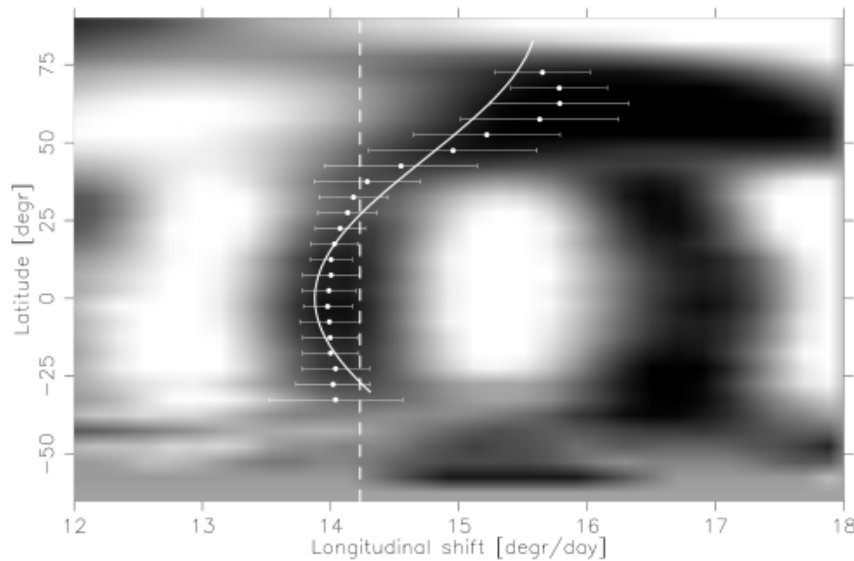


Figure 5.3 – The cross-correlation function from Strassmeier et al. (2003) for two consecutive Doppler images. The grey scale represents the correlation coefficient where black is perfect correlation and white is no correlation. The vertical line represents the rotational period of 25.3 days. Credit: Strassmeier et al. (2003).

These cross-correlation peaks were fitted with a quadratic anti-solar differential rotation law of the form

$$(b) = \Omega_{\text{eq}} + \Omega_1 \sin(b)^2 \quad (5.2)$$

where Ω_{eq} is the angular velocity of the stellar equator, b is the surface latitude and Ω_1 is the difference between the angular velocity of the equator and the pole, $\Omega_1 = \Omega_{eq} - \Omega_{pole}$. Strassmeier et al. (2003) find the constants to be $\Omega_0 = 13.87 \pm 0.22$ and $\Omega_1 = 1.73 \pm 0.67$ based on the latitude range -30° to $+75^\circ$, in steps of 5° .

Even though Strassmeier et al. (2003) presents some of the best evidence for the observation of anti-solar differential rotation, Doppler imaging maps should always be studied critically since the method suffers from difficulties in modeling spectral lines in late-type stars, as well as from uncertainties in stellar and spectral parameters. As mentioned in Hackman et al. (2001), temperature maps obtained with some Doppler methods most often show very large cool starspots covering the poles, whereas other methods rarely show polar starspots. From instances where the same observations have been used, it is evident that the results depend on the methods or the selected stellar and spectral parameters used. A crucial point of Doppler imaging is how the line profiles for a given temperature distribution are calculated. Artifacts can be introduced if there are errors in the calculated line profiles which will affect the surface map of the star. A wrong $v \sin(i)$ will manifest itself as a cool or hot belt in the image. Furthermore a wrong estimate of the inclination will cause a latitudinal displacement together with a slight distortion of the starspots. The effect of differential rotation is very sensitive to the inclination and thus a decrease of the inclination will increase the effect of differential rotation in the line profile¹. In Strassmeier et al. (2003) the inclination of HD 31993 was determined by reducing the misfit of the line profiles as a function of the inclination and by trial-and-error the inclination which gave the most homogeneous temperature maps was adopted to be $i = 65 \pm 15^\circ$. It is not unlikely that the inclination adopted in Strassmeier et al. (2003) might cause artifacts in the Doppler imaging which will affect the cross-correlation function in Figure 5.3. Nevertheless, what is particularly important to note is that the observed starspots on HD 31993 is located at low latitudes in the range $0 - 40^\circ$ and no starspots are detected above a latitude of 60° . Even so, there is still a strong signal in the cross-correlation function above the 60° latitude which might indicate that there is something wrong in the Doppler images.

5.4.3 Hackman et al. (2001)

Another convincing report of anti-solar differential rotation is Hackman et al. (2001) who used a χ^2 landscape technique where Doppler imaging was used to construct a surface temperature map of the FK Comae-type star HD 199178 (V1794 Cygni). Hackman et al. (2001) derived temperature maps by using a modified code where different values of rotational velocity, microturbulence, inclination and surface differential rotation were fitted to a model. The differential rotation was implemented by adjusting the angular

¹Strassmeier et al. (2003), page 173.

rotational velocity at each latitude b using the following rotation law of the form

$$\Omega(b) = \Omega_{eq} (1 - \alpha_{diff} \sin(b)^2) \quad (5.3)$$

where α_{diff} is the surface differential rotation defined by $\alpha_{diff} = (\Omega_{eq} - \Omega_{pole})/\Omega_{eq}$. Bare in mind that the definition of the parameter α_{diff} changes, depending on how it is used in the corresponding article. The best model solution, i.e. the model which showed the smallest deviation between the spectroscopic observations and the calculated line profiles, was found to be $\alpha_{diff} = -0.17$ implying anti-solar differential rotation. The best solution can be seen in Figure 5.4 where a large cool starspot is located at high latitude and is 1200 – 1600 K cooler than the mean surface temperature. Photometric data together with the line profiles which was used in the solution is also shown in Figure 5.4. For the model in Hackman et al. (2001) $\alpha_{diff} < 0$ would cause a more flat bottomed line profile which is also seen in the figure. However, these observed flat bottomed absorption lines are usually interpreted as evidence for a large cool starspot located at the pole, which Hackman et al. (2001) also finds evidence of. Even though several other configurations in the model were used such as solid body rotation and solar differential rotation the best solution found was still $\alpha_{diff} = -0.17$.

Photometric periods P_{phot} for the starspots on Hd 199178 have also been done which supports the theory of differential rotation of the star. By using the parameters determined for the solution of $\alpha_{diff} = -0.17$, Hackman et al. (2001) could calculate the periods of the pole and of the equator where P_{pole} was in fact larger than the smallest measured periods from photometric observations, indicating a discrepancy in this solution. Hackman et al. (2001) conclude that even though HD 199178 from the model fits seems to be experiencing anti-solar differential rotation they do not find conclusive evidence for this and note that there are still other possible explanations for the slightly flat bottomed line profiles.

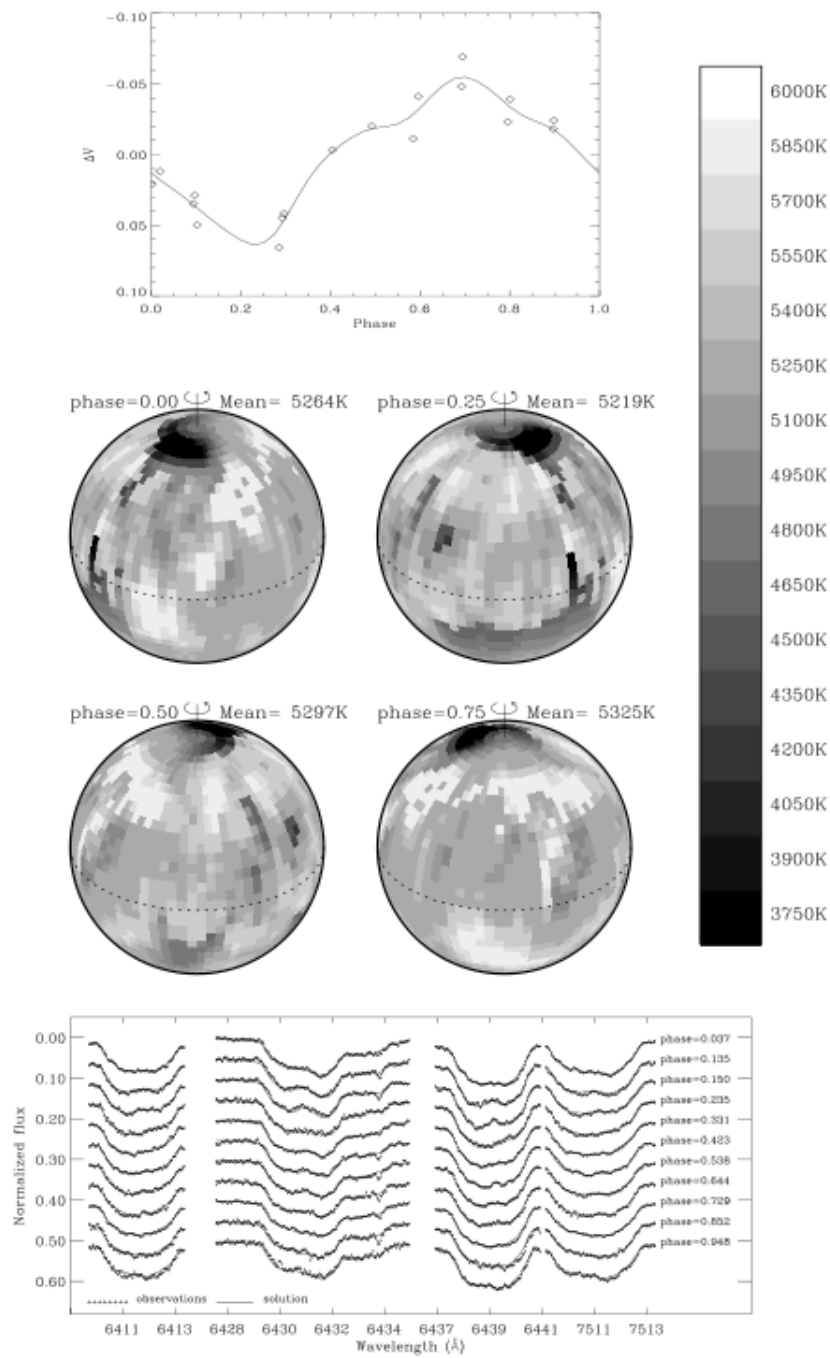


Figure 5.4 – Surface temperature map of HD 199178 from Hackman et al. (2001) where a large cool starspot is located at high latitude. A photometric light curve and the line profiles are also included. Credit: Hackman et al. (2001).

5.4.4 Comparison to the primary component of V80

Both Strassmeier et al. (2003) and Hackman et al. (2001) have used Doppler imaging in order to investigate the surface rotation pattern. It is therefore hard to compare them with the results from the primary component of V80 since we only have indications of anti-solar differential rotation through photometric observations and the assumption that the primary should have synchronized rotation. The only comparison we can make is with the photometric period discrepancy mentioned in Hackman et al. (2001) where the estimated P_{pole} from the model was larger than the smallest periods from photometric observations. All we can see is that there are no periods in the periodogram which have a higher period than the orbital period. Then by assuming that the components of V80 are synchronised, which the time scale for synchronisation suggest, it is hard to come up with an explanation other than the fact that the primary component seems to be experiencing anti-solar differential rotation.

Observations of large starspots are currently the only way stellar surface rotation can be measured and it is therefore crucial to investigate if the movement of the starspots are indeed a good tracer of the stellar surface flow. Korhonen and Elstner (2011) have investigated the surface differential rotation by using snapshots of dynamo models to perform cross-correlation. The obtained surface differential rotations from the snapshots were then compared to the known internal rotation law in the dynamo models. Korhonen and Elstner (2011) conclude that starspots caused by the large scale dynamo field are not necessarily tracing the real surface differential rotation which would be the starspots at high latitude near the stellar pole. Starspots near the equator are in much better agreement with the real surface differential rotation. It therefore seems that starspots caused by small scale localized magnetic fields are good tracers of the stellar differential rotation. One may therefore wonder whether the large starspots observed in magnetically active stars could be caused by small scale magnetic fields and it is therefore still unclear if the true stellar surface rotation can be measured by observations of large starspots.

6. *Summary and conclusions*

In this thesis we have investigated the highly magnetically active detached eclipsing binary system V80 by using new photometric data from the Kepler Space Telescope along with observations from Brogaard et al. (2011). By using the Kwee Van Woerden method we determined the mid-eclipse times for the 189 primary and secondary eclipses from the V , R , Kepler long and short cadence light curves. The orbital period determined from the primary and secondary eclipses from the linear ephemerides was found to be 4.885889 ± 0.000001 and 4.885871 ± 0.000002 days, respectively. The uncertainties are of the order 0.1 s and 0.2 s which means that effects such as special and general relativity begins to play a role in our measurements. Furthermore Mikulášek et al. (2013) showed that the Kwee Van Woerden method tends to underestimate the uncertainties of the corresponding mid-eclipse times. Because of this we adopted an uncertainty of 1 s and found the period of V80 to be 4.88589 ± 0.00001 days. We constructed O-C diagrams from the primary and secondary mid-eclipse times using the adopted ephemerides which can be seen in Figure 4.9. We find no signs of a third body in the binary system which could affect our light curve analysis.

Before we removed the light curve variations caused by the magnetic activity in the Kepler light curves we investigated how this should be done. As can be seen in Figure 4.13 there was no significant difference between dividing or subtracting the continuum. We chose to divide the light curves with the light curve continuum.

The effective temperature of the secondary was not given in Brogaard et al. (2011) and we therefore used a color-temperature-metallicity from Casagrande et al. (2010) in Eq. 4.3. By using the color and $[\text{Fe}/\text{H}]$ of the primary and secondary, together with the effective temperature of the primary measured in Brogaard et al. (2011) we estimated the effective temperature of the secondary component to be 4864 ± 254 K. By using the JKTL D code together with the estimated effective temperature of the secondary we obtained the limb darkening coefficients which was used in the JKTEBOP light curve analysis. The microturbulence velocity listed for the primary component in Brogaard et al. (2011) is $1.10 \pm 0.10 \text{ km s}^{-1}$, however most limb darkening coefficients in JKTL D are only available for a microturbulence velocity of 2.0 km s^{-1} . Because of this, we had to adopt a microturbulence velocity of 2.0 km s^{-1} for both components. The quadratic limb darkening law was available for all three bands and thus, for consistency we chose to use this law. The limb darkening coefficients are listed in Table 4.1.

We performed preliminary light curve analysis of the R , V , Kepler long and short cadence light curves and ran the JKTEBOP code for a range of fixed values of k . Only the V light curve showed a minimum in rms for $k \sim 0.63$ whereas R and the Kepler short cadence light curves showed very poor results. The Kepler long cadence light curve showed a flat minimum in the range $k = [0.60, 0.66]$. Because of this we chose to investigate the Kepler long cadence light curve further by dividing each light curve quarter up into the CCD which was used to measure the light from V80. As before, only no rms minimum for k was found. The CCD which was used to measure quarter 7, 11 and 15 showed a high amount of third light in the light curve of $\sim 80\%$ and we therefore chose to omit these three quarters in our light curve analysis. By removing these quarters, a much better agreement was made between the Kepler long cadence light curve and the V light curve for the orbital inclination. Even though the V light curve showed a minimum for $k \sim 0.63$ we did not use this in our analysis since the Kepler long cadence light curve analysis could not reproduce the same result.

The preliminary light curve analysis showed that the Kepler light curve data is not good enough to determine precise radii of the primary and secondary components since a minimum in rms for k could not be found. The reason for this is a combination of the high magnetic activity in V80 and the amount of third light in the Kepler light curve. In order to get reliable results from the JKTEBOP light curve analysis for the Kepler long cadence light curve we had to use some constraints. First we used the light ratio constraint from Brogaard et al. (2011) of $L = L_2/L_1 = 0.15 \pm 0.05$ from the V band and assumed that the primary and secondary components could be described as perfect black bodies using Planck's law of black body radiation. By using the Kepler and V response functions we estimated the light ratio in the Kepler band to be $L = L_2/L_1 = 0.267 \pm 0.102$ which was used as a constrain in the JKTEBOP light curve solutions. The second constrain which we used was from the mass-radius relation from one of the best isochrones estimated for NGC 6791 in Brogaard et al. (2012). By using the masses of the primary and secondary, together with the spectroscopic results from Brogaard et al. (2011) we could calculate the radii, $r_{p,s}$ which matched the isochrone for the corresponding masses. By changing between fixing r_p and r_s in our JKTEBOP solutions of V80 we got two different results for the components.

Magnetic activity in the components of binary systems are known to result in discrepancies between observations and stellar models. Stellar models are known to predict stellar radii and temperatures which are $\sim 10\%$ lower and $\sim 5\%$ higher than what is observed, respectively. From our analysis of the magnetic activity we made observations which indicates that the magnetic activity is originating from the primary component. We could however not be certain that the secondary is not magnetically active as well since its magnetic activity could be hidden in the magnetic activity of the primary component. Because of this, we included a JKTEBOP solution where the radius of the secondary was fixed with an increased radius of 10% . Each of the three JKTE-

BOP solutions gave equally good fits to the light curve data and no visible difference in the three models could be seen. The MR diagram however revealed that the best results were for fixed r_s and $r_s + 10\%$. We therefore believe that the configuration of the radii of the primary and secondary components are likely to lie in the range of $1.396 \pm 0.067R_\odot < R_p < 1.354 \pm 0.067R_\odot$ and $0.7595R_\odot < R_s < 0.8358R_\odot$. For the primary component this corresponds to discrepancies in radius that is 6.8% – 10.5% larger than what stellar models predict.

The effective temperatures of the components compared to the isochrone in the MT diagram did not show any discrepancies in Figure 5.1. Compared to the MT relation, the primary is 0.7% cooler and the secondary is 4.3% hotter. It does therefore not look like the primary component share the same temperature discrepancy which is observed for other magnetically active stars. The temperature of the secondary is in fact 4.3% hotter than what the stellar model predicts, however due to the high uncertainty in temperature we cannot conclude anything from its possible observed discrepancy in temperature.

By using a period search using the Phase Dispersion Minimization technique we found a dominant starspot period of 4.738 ± 0.008 days. The time scale for synchronisation is 7.6860 ± 0.0005 Myr and the age of V80 is 8.3 ± 0.3 Gyr. Synchronisation should therefore have occurred a long time ago and the rotational period of the primary component should therefore be equal to the orbital period of V80. By using the measured rotational velocity of the primary in Brogaard et al. (2011) combined with the main starspot and orbital periods we derived two estimates for the primary component using Eq. 5.1. This resulted in a radius of the primary component of $1.32 \pm 0.19R_\odot$ and $1.36 \pm 0.19R_\odot$ for the main starspot and orbital period, respectively. Both results agree with the light curve solutions for fixed r_s and $r_s + 10\%$. Even though the uncertainties are high, it does however indicate that the starspot pattern responsible for the light curve variation in V80 is originating from the primary component.

V80 shows further presence of magnetic activity by being an X-ray source with $L_{X,u} = 2.2 \cdot 10^{30}$ erg s⁻¹ and by having a superflare in the Kepler light curve. The empirical relation between X-ray luminosity and stellar rotation period does not agree with the luminosity observed for V80. Even by assuming that both components of V80 follow the empirical relation, the X-ray luminosity of V80 is still a factor of 10 higher than what is expected. This could suggest that both the primary and secondary components are highly magnetically active. Superflares are known to have luminosities of 4 – 10% of the stellar luminosity from which they originate. If the observed superflare in the Kepler light curve is considered to come from the secondary component, the luminosity of the superflare would be 40% of the secondary, whereas it would be 10% of the luminosity if it originated from the primary component. This further suggests that the magnetic activity of V80 is indeed coming from the primary component.

In our analysis a period search was performed on the Kepler light curve which revealed

several periods for the primary component which is a common indication that a star is rotating differentially. There are however no starspot periods at or above the orbital period of V80. Assuming that synchronisation has occurred would suggest that the primary rotates slower at the equator than at higher latitudes. It therefore seems as though the primary component is experiencing anti-solar differential rotation. In order to further confirm this, Doppler imaging could be used. Unfortunately in order to use Doppler imaging, the projected rotational velocities of the star needs to be more than 20 km s^{-1} which is not the case for the primary component which has a projected rotational velocity of $14.00 \pm 2.00 \text{ km s}^{-1}$. Furthermore the spectra obtained from UVES in Brogaard et al. (2011) had a signal-to-noise ratio of only 15, whereas Doppler imaging requires a signal-to-noise ratio of at least 10 times more. It therefore seems as though it will be impossible to obtain observations which could confirm if the primary component is indeed experiencing anti-solar differential rotation. Stellar dynamo models could however be used to see if the observations we have made in this thesis can be mimicked by a star which is experiencing solar differential rotation or if our observations can only be reproduced if the star is experiencing anti-solar differential rotation.

We discussed how several papers such as Clausen et al. (2008), Clausen et al. (2009) and Vos et al. (2012) lower the mixing-length-parameter of magnetically active components in detached binaries in order to mimick the expected reduction in convective efficiency due to starspots. It seems that such an approach is highly likely to cause flawed estimates of the stellar parameters of these systems since parameters such as $[\text{Fe}/\text{H}]$ and Y are fixed without assuming the uncertainties of these parameters. By doing so, it is also assumed that the observed discrepancies between observations and stellar models are solely caused by the mixing-length-parameter. In order to investigate the contribution of the mixing-length-parameter related to the observed discrepancies of magnetically active binary components, MR and MT relations need to be compared to observations. In order to do this the binary systems need to be in a cluster for which the stellar parameters have been constrained to a very high precision as in the case of NGC 6791. Investigating the relation between several magnetically active binaries located in NGC 6791 could therefore provide knowledge of how the mixing-length-parameter relates to the discrepancies in radii and temperature between observations and stellar models.

Bibliography

- Svetlana V Berdyugina. Starspots: a key to the stellar dynamo. *Living Rev. Solar Phys.*, 2:8, 2005.
- Jayne Birkby, Bas Nefs, Simon Hodgkin, Gábor Kovács, Brigitta Sipócz, David Pinfield, Ignas Snellen, Dimitris Mislis, Felipe Murgas, Nicolas Lodieu, et al. Discovery and characterization of detached m dwarf eclipsing binaries in the wfcam transit survey. *Monthly Notices of the Royal Astronomical Society*, 426(2):1507–1532, 2012.
- K Brogaard, H Bruntt, F Grundahl, Jens Viggo Clausen, Søren Frandsen, DA Vandenberg, and LR Bedin. Age and helium content of the open cluster ngc 6791 from multiple eclipsing binary members. i. measurements, methods, and first results. *arXiv preprint arXiv:1009.5537*, 2011.
- K Brogaard, DA Vandenberg, H Bruntt, F Grundahl, S Frandsen, LR Bedin, AP Milone, A Dotter, GA Feiden, PB Stetson, et al. Age and helium content of the open cluster ngc 6791 from multiple eclipsing binary members. ii. age dependencies and new insights. *arXiv preprint arXiv:1205.4071*, 2012.
- L Casagrande, I Ramírez, J Meléndez, M Bessell, and M Asplund. An absolutely calibrated teff scale from the infrared flux method*. *Astronomy and Astrophysics*, 512, 2010.
- Jens Viggo Clausen, G Torres, H Bruntt, Johannes Andersen, Birgitta Nordström, RP Stefanik, David W Latham, and John Southworth. Absolute dimensions of eclipsing binaries. xxvi. setting a new standard: Masses, radii, and abundances for the f-type systems ad bootis, vz hydrae, and wz ophiuchi. *arXiv preprint arXiv:0806.3218*, 2008.
- Jens Viggo Clausen, H Bruntt, A Claret, A Larsen, Johannes Andersen, B Nordstrom, and A Giménez. Absolute dimensions of solar-type eclipsing binaries. ii. v636 centauri: A 1.05 msun primary with an active, cool, oversize 0.85 msun secondary. *arXiv preprint arXiv:0905.3077*, 2009.
- Jens Viggo Clausen, H Bruntt, E. H. Olsen, and A Claret. Absolute dimensions of solar-type eclipsing binaries. iii. ew orionis: Stellar evolutionary models tested by a g0 v system. *arXiv preprint arXiv:0912.3450*, 2010.

- Jørgen C. Dalsgaard. *Lecture Notes on: Stellar Structure and Evolution*, volume 6. Aarhus University, 2008.
- Paul B Etzel. A simple synthesis method for solving the elements of well-detached eclipsing systems. In *Photometric and Spectroscopic Binary Systems*, pages 111–120. Springer, 1981.
- Thomas Hackman, Lauri Jetsu, and I Tuominen. Surface imaging of hd 199178 (v1794 cygni). *arXiv preprint astro-ph/0106118*, 2001.
- Ronald W Hilditch. *An introduction to close binary stars*. Cambridge University Press, 2001.
- Steve B Howell. *Handbook of CCD astronomy*, volume 5. Cambridge University Press, 2006.
- Zs Köovári, J Bartus, M Švanda, K Vida, KG Strassmeier, K Oláh, and E Forgács-Dajka. Surface velocity network with anti-solar differential rotation on the active-giant σ geminorum. *Astronomische Nachrichten*, 328(10):1081–1083, 2007.
- H Korhonen and D Elstner. Investigating variation of latitudinal stellar spot rotation and its relation to the real stellar surface rotation. *arXiv preprint arXiv:1106.1335*, 2011.
- KùK Kwee and H Van Woerden. A method for computing accurately the epoch of minimum of an eclipsing variable. *Bulletin of the Astronomical Institutes of the Netherlands*, 12:327, 1956.
- Hiroyuki Maehara, Takuya Shibayama, Shota Notsu, Yuta Notsu, Takashi Nagao, Satoshi Kusaba, Satoshi Honda, Daisaku Nogami, and Kazunari Shibata. Superflares on solar-type stars. *Nature*, 485(7399):478–481, 2012.
- Zdeněk Mikulášek, Marek Chrastina, Miloslav Zejda, Jan Janík, LiYjing Yhu, and Shen-Bang Qian. Kwee-van woerden method: To use or not to use? *arXiv preprint arXiv:1311.0207*, 2013.
- Juan Carlos Morales, José Gallardo, Ignasi Ribas, Carme Jordi, Isabelle Baraffe, and Gilles Chabrier. The effect of magnetic activity on low-mass stars in eclipsing binaries. *The Astrophysical Journal*, 718(1):502, 2010.
- Burt Nelson and Walter D Davis. Eclipsing-binary solutions by sequential optimization of the parameters. *The Astrophysical Journal*, 174:617, 1972.
- Stefano Pasetto, Cesare Chiosi, Mark Cropper, and Eva K Grebel. Theory of stellar convection: Removing the mixing-length parameter. *arXiv preprint arXiv:1403.6122*, 2014.

- N Pizzolato, A Maggio, G Micela, S Sciortino, and P Ventura. The stellar activity-rotation relationship revisited: Dependence of saturated and non-saturated x-ray emission regimes on stellar mass for late-type dwarfs. *ASTRONOMY AND ASTROPHYSICS-BERLIN*-, 397(1):147–158, 2003.
- John Southworth, Hans Bruntt, and Derek L Buzasi. Eclipsing binaries observed with the wire satellite-ii. \ beta aurigae and non-linear limb darkening in light curves. *Astronomy & Astrophysics*, 467(3):1215–1226, 2007.
- Steven W Stahler and Francesco Palla. *The formation of stars*. John Wiley & Sons, 2008.
- RF Stellingwerf. Period determination using phase dispersion minimization. *The Astrophysical Journal*, 224:953–960, 1978.
- KG Strassmeier, L Kratzwald, and M Weber. Doppler imaging of stellar surface structure. xx. the rapidly-rotating single k2-giant hd 31993= v1192 orionis. *Astronomy and Astrophysics*, 408:1103–1113, 2003.
- Regner Trampedach and Robert F Stein. The mass mixing length in convective stellar envelopes. *The Astrophysical Journal*, 731(2):78, 2011.
- Maureen Van den Berg, Frank Verbunt, Gianpiero Tagliaferri, Tomaso Belloni, Luigi R Bedin, and Imants Platais. A chandra x-ray study of the interacting binaries in the old open cluster ngc 6791. *The Astrophysical Journal*, 770(2):98, 2013.
- Steven S Vogt, Artie P Hatzes, Anthony A Misch, and M Kürster. Doppler imagery of the spotted rs canum venaticorum star hr 1099 (v711 tauri) from 1981 to 1992. *The Astrophysical Journal Supplement Series*, 121(2):547, 1999.
- Joris Vos, Jens Viggo Clausen, Uffe Gråe Jørgensen, RH Østensen, Antonio Claret, Michel Hillen, and Katrina Exter. Absolute dimensions of solar-type eclipsing binaries. ef aquarii: a g0 test for stellar evolution models. *arXiv preprint arXiv:1202.4851*, 2012.
- M Weber. Differential rotation of giant stars. *Astronomische Nachrichten*, 328(10):1075–1077, 2007.
- M Weber, KG Strassmeier, and A Washuettl. Indications for anti-solar differential rotation of giant stars. *Astronomische Nachrichten*, 326(3-4):287–291, 2005.
- J-P Zahn. Tidal friction in close binary stars. *Astronomy and Astrophysics*, 57:383–394, 1977.